Simulating the Effects of Neural Pathology on Cochlear Implant Responses

Jesse M. Resnick

A dissertation

submitted in partial fulfillment of the

requirements for the degree of

Doctor of Philosophy

University of Washington

2019

Reading Committee:

Jay T. Rubinstein, Chair

David J. Perkel

Fred M. Rieke

Program Authorized to Offer Degree:

Graduate Program in Neuroscience

University of Washington

Abstract

Simulating the Effects of Intrinsic Neuron Pathology on Cochlear Implant Responses

Jesse M. Resnick

Chair of the Supervisory Committee:
Jay T. Rubinstein
Otolaryngology- Head and Neck Surgery

Cochlear implants (CIs) provide a strategy for treating severe to profound sensorineural hearing loss (SNHL) that cannot be adequately managed by amplifying acoustic signals. There is considerable variability of CI effectiveness among bilaterally implanted patients with similar pre-operative audiograms, and the factors underlying this variability are not completely understood (Blamey et al., 2012; Lazard et al., 2012; Orabi et al., 2006). Some individuals achieve near perfect performance on tasks requiring speech recognition in quiet while others receive far less benefit (Lazard et al., 2012). Binaural hearing-dependent tasks, such as localizing sound sources based on interaural timing and level cues or discerning speech in noise, are particularly variable even in the research setting with optimized delivery of fine temporal structure information (Kan and Litovsky, 2014; Litovsky et al., 2012). Understanding the biological mechanisms of this variability may enable the design of individually-tailored stimulation strategies and improve prognostics. Temporal bone studies in humans and animal models describe both significant, diameter-dependent degeneration of spiral ganglion neurons (SGNs) and demyelination of remaining peripheral axons (Incesulu and Nadol, 1998; Leake and Hradek, 1988; Seyyedi et al., 2014; Shepherd et al., 2004). The present work explores the question of whether pathological demyelination and fiber diameter-dependent degeneration of spiral ganglion neuron processes following loss of afferent input from hair cells can explain particular features of experimental inter-animal and patient-to-patient variability in outcomes to electrical stimulation. These pathological manifestations were incorporated into population-scale biophysical computer simulations of implant stimulation and shown capable of reproducing key dimensions of observed variability at multiple scales, including model animal single-unit response timing, human inter-aural timing difference detection, and electrically-evoked, intracochlearly-recorded potentials. These findings suggest that both asymmetric loss and microarchitectural changes of SGNs may shape the temporal dynamics of population responses and may place fundamental restrictions on the performance of implants in some individuals.

Contents

Chapter 1- Introduction and Overview

1.1 The state of the field: Cochlear implant history, principles, and challenges

Cochlear implants (CIs) are the most prevalent and successful neural prostheses in current use. To date, hundreds of thousands of severe to profoundly deaf individuals, both adults and children, have received at least one implant and most users experience dramatic improvements in their speech recognition and environmental sound awareness via their electrical hearing. The most successful users can perform open-set speech reception near perfectly in quiet environments and perform relatively well, though not as well as normal-hearing individuals, when listening to speech in noise (Brant et al., 2018). These benefits constitute a dramatic average improvement in quality of life as quantified by standardized measures (Bond et al., 2009; Budenz et al., 2011; Crowson et al., 2018; Geers et al., 2011; Orabi et al., 2006). Consequently, the indications and coverage for CI surgery and post-operative rehabilitation have both expanded. Bilateral implantation, both sequential and simultaneous, is becoming common and evidence suggests the second implants provide additional improvement in outcomes, particularly speech recognition in noise (Basura et al., 2009; Bond et al., 2009).

These outcomes are particularly remarkable given the history of cochlea implant development. The first CIs implanted by the pioneering group of Dr. William House and colleagues in the early 1960s were performed without significant prior testing in animal models and with significant concerns within the medical community about the impact of electrical stimulation in otherwise healthy humans (Niparko et al., 2009; Wilson and Dorman, 2008). Despite these unknowns and the relative simplicity of these early single-channel implants, the outcomes were extremely promising with individuals developing environmental awareness of sound with modest side effects. Over the following decades, implant technology rapidly advanced with the development of multi-channel arrays and novel processing strategies resulting in the dissipation of ethical concerns regarding them as many patients began developing significant post-operative speech recognition. Despite these empirical advances, the challenges of performing basic science studies within the inner ear leave many significant unknowns regarding the details of neural activation by CIs.

CIs are believed to function by directly activating primary auditory, Type-1 spiral ganglion neurons (SGNs) with current injected through electrodes implanted within the cochlea. The loudness percept of implantees and intracochlear electrically-evoked compound action potential (eCAP) amplitudes are correlated with the intensity of delivered currents, presumably due to recruitment of additional neurons with increasing intensity (Azadpour et al., 2018; Hughes and Laurello, 2017; Kirby et al., 2012). However, the relative order by which neurons with different intrinsic properties are recruited across different regions of the cochlea by different stimulus paradigms remains poorly understood in vivo (Guérit et al., 2018; Macherey et al., 2017, 2006). Moreover, while single unit recordings in animal models provide some insight, the location of action potential initiation within individual neurons, and how these sites of excitation change, with stimulus level cannot be directly determined in humans (Miller et al., 2006, 2003; Rubinstein et al., 2001).

With these unknowns, it is unsurprising that electrical hearing fails to fully replicate acoustic hearing and that poorly explained variance in outcomes has been a persistent challenge within the field. The factors that have been shown to predict CI outcomes are consistent with the hypothesis of direct activation of SGNs. Between ears within individual subjects, speech outcomes during life are correlated with post-mortem spiral ganglion neuron counts (Incesulu and Nadol, 1998; Seyyedi et al., 2014). Patients with hearing loss etiologies that spare SGNs tend to have superior outcomes to those that produce significant primary neuron death (Eppsteiner et al., 2012; Shearer et al., 2017). Similarly, residual speech recognition is a positive predictor of CI performance (Rubinstein et al., 1999). Conversely, CI performance is inversely related to the duration of hearing deprivation (Medina et al., 2017). Despite these insights, a predictive model incorporating identified epidemiological factors can account for only 22% of variance in CI speech perception (Blamey et al., 1996; Lazard et al., 2012). eCAPs have drawn interest as an objective approach to assess neural health via their responses to stimulation; while eCAP features do exhibit modest correlations with speech outcomes at the group level, enormous variability at the individual level confounds their interpretation (Eijl et al., 2017; Schvartz-Leyzac and Pfingst, 2017). A better understanding of the biophysics underlying CI function may improve prognostics and, in turn, refine implantation criteria.

Compounding this challenge of variance, while CIs do provide remarkable benefits implantees receive only poor facsimiles of some acoustic ques, such as pitch place coding, and completely disrupt others, notably fine temporal structure. The net result is that CIs generally provide relatively poor speech in noise, melody, and sound source location perception (Dorman et al., 2017; Drennan et al., 2015; Imennov et al., 2013; Yamazaki et al., 2017). Substantial effort has been expended attempting to create engineered remedies to these deficits but, since initial advances with multiple electrode arrays and the introduction of continuous interleaved stimulation (CIS) in the 1990s, these innovations have yielded diminished returns or improved one aspect of signal coding at the expense of others (Drennan et al., 2010). One class of fine temporal cues of particular interest are interaural timing difference, leveraged to localize auditory objects in the azimuthal plane in acoustical hearing. Clinical CI processing strategies discard this information when they extract the envelope of sounds and, unsurprisingly, CI users without residual acoustic hearing generally cannot detect ITDs using their clinical processor. In the research setting, it is feasible to synchronize the processors of bilateral implantees and select pitch-matched electrodes to present low-rate pulse trains with ITDs (Kan et al., 2015; Kan and Litovsky, 2014; Litovsky et al., 2012, 2010). Unfortunately, even with these refinements no CI users can detect ITDs with the precision typical of acoustic listeners and many cannot detect even supraphysiological ITDs. This raises the concerning possibility that the nature of CI electrical stimulation may place fundamental limitations on what temporal cues it is possible to provide. Additionally, the large inter-subject variability highlights the poorly understood impact of neural health on outcomes.

Experiments in animal models of deafness and CI stimulation have yielded some insights into these fundamental mechanisms of CI function. A number of groups have recorded single unit responses from the central axons of SGNs entering the brain stem in response to intracochlear electrical stimulation. In these experiments, the thresholds of individual neurons vary widely, likely due to a combination of variability in neuron intrinsic properties and the inability of these experiments to control the distance from the electrode. Nevertheless, significant correlations between the response properties of these individual neurons have been identified with stimulus level and pulse waveform, notably pulse polarity (Javel and Shepherd, 2000; Miller et al., 1999; Shepherd and Javel, 1999). These findings highlight how the details of electrical stimulation may interact with the biological substrate of the inner ear in complex and functionally important ways. With prolonged durations of deafness, cats and guinea pigs exhibit reduced SGN counts; importantly, this phenomenon appears progressive, though with species specific time courses (Kroon et al., 2017; Shepherd et al., 2004; Shepherd and Hardie, 2001; Sly et al., 2007). In addition to this frank degenerative process, a reduction in the quantity of myelin surrounding the peripheral process of neurons has been observed in both humans (Leake et al., 1991) and mice (Tagoe et al., 2014) following deafening. These degenerative and demyelination processes, along with other pathological changes in the damaged cochlea, produce increases in both auditory evoked brain stem and SGN single unit response thresholds with increasing pre-procedure duration of deafness (Shepherd et al., 2004; Shepherd and Javel, 1997). Single unit recordings from one set of experiments in rats found substantial variability of response latency and jitter between individual fibers but no significant effect of deafness duration, while those of another in guinea pig study exhibited decreasing response latency with duration of deafness (Shepherd et al., 2004; Sly et al., 2007). At the neural population level, eCAPs recorded in guinea pigs exhibited a multitude of changes in morphology and growth function properties in cohorts with different durations of deafness; though there was again huge degrees of inter-animal variability in these recordings (Ramekers et al., 2014).

Despite this body of data, many important questions remain. How are the structural pathologies observed at the microscopy level impacting electrophysiological outcomes? Do these changes occur in humans and how much of variability in CI outcomes do they drive? Are there fundamental limitations of electrical stimulations ability to deliver certain cues driven by the level and waveform dependence of response timing properties, and might these limitations vary with the health of the neural population?

1.2 Overview of data chapters

Since cochlear implant function involves direct depolarization of spiral ganglion neurons by applied current, SGN physiological health must be an important factor in CI outcomes. This expected relationship has, however, been difficult to confirm in implant recipients. Suggestively, animal studies have demonstrated both acute and progressive SGN ultrastructural changes (notably axon demyelination), even in the absence of soma death, and corresponding altered physiology following sensorineural deafening. Whether such demyelination occurs in humans and how such changes might impact CI function remains unknown. To approach this problem, we incorporated SGN demyelination into a biophysical model of extracellular stimulation of SGN fibers and explored responses of single fibers and populations of fibers, comparing their behavior to animal and human results at different levels.

In **Chapter 2**, we begin at the single-fiber level with an exploration of response properties of individual fibers spanning entire parameter space corresponding to simulated myelin diameter and extent of fiber affected. All simulated fibers were stimulated distally with anodic monophasic, cathodic monophasic, anode-phase-first (AF) biphasic, and cathode-phase-first (CF) biphasic pulses presented by a extracellular disc electrode and monitored for spikes centrally. Not surprisingly, axon sensitivity generally decreased with demyelination, resulting in elevated thresholds, however, this effect was strongly non-uniform. Fibers with severe demyelination affecting only the most peripheral nodes responded nearly identically to normally myelinated fibers. Additionally, partial demyelination (<50%) yielded only minimal increases in threshold even when the entire fiber was impacted. The temporal effects of demyelination were more unexpected. Both latency and jitter of responses demonstrated resilience to modest changes but exhibited strongly non-monotonic and stimulus-dependent relationships to more profound demyelination. Normal, and modestly demyelinated, fibers were more sensitive to cathodic than anodic monophasic pulses and to CF than AF biphasic pulses, however, when demyelination was more severe these relative sensitivities were reversed. Comparison of threshold crossing between nodal segments demonstrated stimulus-dependent shifts in action potential initiation with different fiber demyelination states. For some demyelination scenarios, both phases of biphasic pulses could initiate action potentials at threshold resulting in bimodal latency and initiation site distributions and dramatically increased jitter. In short, simulated demyelination leads to complex changes in fiber sensitivity and spike timing, mediated by alterations in action potential initiation site and slowed action potential conduction due to non-uniformities in the electrical properties of axons. Such demyelination-induced changes, if present in implantees, would have profound implications for the detection of fine temporal cues but not disrupt cues on the time scale of speech envelopes. These simulation results highlight the importance of exploring the SGN ultrastructural changes caused by a given etiology of hearing loss to more accurately predict cochlear implantation outcomes.

In **Chapter 3**, we extend this approach to consider heterogeneously myelinated populations of fibers with either normal or aberrant mean levels of myelination. By considering populations of neurons, we explore how natural variability in the intrinsic properties of neurons may interact with pathological changes to shift population response properties. For normally myelinated populations, the distribution of ratios of myelin diameter to axolemma diameter, termed the g-ratio, was matched to those empirically measured by Wan and Corfas in mice (Wan and Corfas, 2017). Demyelination was applied by shifting the mean of this distribution while maintaining the normal level of variance. We hypothesize that this normal g-ratio variance would represent a lower bound for variability in pathological populations. Application of single anode-first biphasic pulses to these populations enabled assessment of population firing efficiencies and spike latency distributions.

This procedure resulted in profound differences in the recruitment and timing properties of fibers across populations with different myelination states. As in our single fiber studies, with modest to moderate demyelination the input-output curves of populations are nearly normal. With more severe demyelination-distribution means, populations become less sensitive, resulting in elevated thresholds; these shifts are relatively modest except in the event of extreme myelin loss. Substantial myelination variance produced shallower slopes of input-output curves due to slower recruitment of fibers with different myelination states. Moreover, in populations including some extremely demyelinated fibers, these fibers failed to respond even at the highest current intensities tested, yielding submaximal population firing efficiencies.

Response-latency distributions were even more sensitive to both the averages and variances of the demyelination severity distributions. As average myelin loss increased, slowed conduction velocities led to increased latencies and broadening of latency distributions. In populations containing severely demyelinated fibers, central initiation dramatically reduced response latencies in some fibers, yielding bimodal latency distributions. Modest increases in myelination variance at these elevated average demyelination levels further increased jitter and the incidence of bimodality.

Ultimately, we want to be able to predict how structural changes in SGNs will manifest in the encoding of information of relevance to listeners. We hypothesize that demyelination will dramatically alter populations' abilities to encode fine temporal structure information while largely sparing envelope coding. To explore this question, we delivered low-rate pulse train stimuli like those used in a psychophysical interaural timing detection tasks to different populations (Litovsky et al., 2012). The latency distributions of populations' responses were subjected to a receiver-operator characteristic (ROC) analysis to determine ITD just-noticeable differences (JNDs). Poorly myelinated populations exhibited dramatically elevated ITD JNDs even when different model assumptions were explored. Overall the spectrum of JNDs observed for these different populations was sufficiently large to cover that observed in psychophysical measures of CI user abilities. This result suggests that poor neural synchrony due to microarchitectural changes in SGNs may set fundamental limits on the ability of electrical stimulation to deliver fine temporal structure information.

Electrically evoked compound action potentials (eCAPs) are intracochlear recordings of cellular responses to implant stimulation that can be obtained in both humans and animal models. In principle these recordings provide an objective measure of neural response to stimulation and a method of bridging findings between the human and animal model literature. Unfortunately, in practice there is enormous eCAP variability between individuals, and even amongst electrodes within a single implant, that cannot be adequately explained and frustrates interpretation and synthesis of results. **Chapter 4** explores impacts of neural degeneration on the morphology and growth functions of electrically-evoked compound action potentials (eCAPs) and compares these results to those recorded in animal models of chronic deafness and CI stimulation to gain insight into the sources of eCAP variability observed in CI users. eCAPs are intracochlear recordings of cellular responses to implant stimulation that, in principle, provide an objective measure of neural response to stimulation and a method of bridging findings between the human and animal model literature. Unfortunately, in practice there is enormous eCAP variability between individuals, and even amongst electrodes within a single implant, that cannot be adequately explained and frustrates interpretation and synthesis of results. We extended our stochastic, biophysical, computational model of electrical stimulation of spiral ganglion fibers to simulate eCAPs in populations with different levels of diameter-dependent fiber degeneration. Simulated eCAPs recapitulate many of the key morphological features of those recorded both in CI recipients and animal models while enabling simultaneous analysis of spiking activity.

To gain insight into the neural mechanisms underlying eCAP changes, we first explored how charge integration changes with the distribution of fiber diameter across the population. The firing efficiency growth function was simulated for each population to biphasic pulses with different phase durations. With long phase durations, degenerated population growth functions were remarkably similar to those of the normally populations, albeit with elevated thresholds, however, with short phase durations pathological populations exhibited reduced growth function slopes. Strength-duration analysis of the fibers constituting the populations enabled estimation of their temporal integration properties. Diameter-dependent degeneration produced significant changes in the distributions of both fiber rheobases and chronaxies. Both the mean and the variance of the fibers' rheobase distributions increased with degeneration severity; in contrast, while mean chronaxie increased chronaxie variance decreased. These findings demonstrate that shifts in diameter distributions may produce significant changes in physiological properties across the population.

We next explored what effect these changes would be expected to have on eCAP growth function morphology. Adenis et al. (2018) explored eCAP threshold growth functions in acutely and chronically stimulated guinea pigs to stimuli where delivered charge was controlled by varying either pulse amplitude or phase durations (Adenis et al., 2018). They observed great between-animal heterogeneity of relative growth functions, particularly in chronically deafened animals. eCAP growth functions of normal simulated populations recapitulate key features of the acutely deafened animal responses. Notably, with high total charge delivery, response amplitudes to phase-duration-based stimuli lagged those to amplitude-based stimuli of equal net charge, reflecting the importance of neural time constants even amongst healthy neurons. Diameter-dependent degeneration yielded response growth functions that exhibited many of the key dimensions of variability observed by Adenis et al., including alterations in relative slope and peak response amplitudes but that failed to capture others, notably thresholds. While eCAP growth functions exhibited a notable effect of diameter-dependent degeneraiton with long pulse widths, spike efficiency functions did not. Analysis of spike latency and eCAP peak width demonstrates that this variable amplitude growth is due to eCAP amplitudes reflecting both fiber recruitment and response synchrony.

Ramekers et al. performed a similar series of experiments characterizing the eCAP amplitude growth function (AGF) properties of animals with varying durations of deafness in response to stimuli with different inter-phase gaps (IPGs). They observed a number of significant changes in AGF functions in animals with long durations of deafness that correlated with the SGN counts of the animals. In healthy animals, AGF slope increases when the stimuli IPGs are increased from 2 to 30 µs. The most prominent change they observed with prolonged duration of deafness was a reduction in this change in AGF slope, a phenomenon they termed the ‘IPG effect’. Characterization of the AGFs of stimulated populations reproduces this effect; populations with altered diameter distributions exhibit a reduced change in AGF slope with increasing IPG compared to normal ones. Analysis of the population firing efficiency growth functions demonstrates that they parallel the changes observed in the eCAP AGFs, suggesting that the change in the later is due to reduced recruitment. Based on the observed elevation of time constants in small fibers, we hypothesize this change in IPG sensitivity is due to poorer release from opposing polarity interference in the demyelinated populations since the IPG changes are a relatively small proportion of the fibers’ elevated chronaxie. These results suggest that asymmetric sensitivities of fibers of different size to damage may lead to changes in the distribution of physiological properties that underlie much of the variability in eCAP properties and that continued attention to natural and pathological variability in neural responses may help unravel these dynamics.

Chapter 2: Effects of simulated demyelination on single unit properties

Coauthored by Gabrielle O’Brien and Jay T. Rubinstein.

The content in this chapter was published as “Simulated Auditory Nerve Axon Demyelination Alters Sensitivity and Response Timing to Extracellular Stimulation” in Hearing Research, 2018 Issue 361 p 121-137.

2.1 Introduction

While the overwhelming majority of cochlear implant recipients with bilateral, post-lingual deafness report at least some improvement in speech recognition and quality of life, there is substantial variability in just how much individual implant recipients benefit from their device (Blamey et al., 1996; Lazard et al., 2012; Orabi et al., 2006). Some individuals achieve near perfect performance on tasks requiring speech recognition in quiet while others receive far less benefit (Poissant et al., 2014). Binaural hearing-dependent tasks, such as localizing sound sources based on interaural timing and level cues, are particularly variable in recipients of bilateral implants, even with optimized delivery of fine temporal structure information, pitch-matching of electrodes, and device synchronization (Kan and Litovsky, 2014; Litovsky et al., 2012). This diversity of CI outcomes is only partially accounted for by pre- and peri-operative factors (Lazard et al., 2012).

Since CI function involves direct depolarization of spiral ganglion neurons (SGNs) by extracellular current, it is presumed that SGN physiological health is an important factor in CI outcomes. Of the epidemiological factors that correlate with outcomes, most predictive pre-operative factors are implicitly related to the neural integrity, including duration and etiology of deafness (Blamey et al., 2012, 1996; Lazard et al., 2012; Rubinstein et al., 1999). This expected relationship has been challenging to directly demonstrate in humans. One of the few studies of post-mortem human temporal bones found significant loss of SGN somata in older individuals, particularly in the basal cochlea; this loss was greater when both inner and outer hair cells were absent, suggesting that progressive SGN loss does occur in humans, particularly those with HL (Zimmermann et al., 1995). A study correlating threshold measures of CI recipients in life with post-mortem SGN counts observed no inter-subject correlation but a significant interaural correlation (Incesulu and Nadol, 1998). Other, less direct, lines of evidence also support the hypothesis that SGN integrity is critical to outcomes. Patients with SGN sparing, non-syndromic etiologies of deafness have significantly better outcomes than those with either genetic lesions impacting SGNs or infectious etiologies known to cause nerve damage (Shearer et al., 2017). Collectively, these findings suggest that SGN function is critical to CI functionality but that gross measures that reflect only the presence of SGNs may not provide sufficient detail into their functional status and capture only part of clinical variance.

Limited human and animal studies have demonstrated both acute and progressive SGN ultrastructural changes, notably axon demyelination, even in the absence of soma death, and corresponding altered physiology following sensorineural deafening. Loss of myelination within the peripheral process precedes that of the central process, and ultimately degeneration of these processes and cell death in both humans and cats (Hardie and Shepherd, 1999; Leake and Hradek, 1988; Shepherd and Javel, 1999). More recently, Tagoe et al. (2014) noted a reduction in myelin lamellae number and a downward shift in the distribution of myelin thickness following deafening via acoustic over-exposure in rats. Collectively, these studies indicate the structural integrity of SGNs, particularly myelin insulation of internodal segments, is damaged following deafening; and the time course, while not fully characterized, suggests progressive processes. Thus far, due to technical constraints, no studies exploring the relationship between SGN myelination and behavioral measures of hearing have been performed in humans. There are, however, case reports of febrile deafness in patients with autoimmune demyelinating disorders in which elevated core body temperature produced temporary hearing impairment, highlighting the important interaction of myelination and auditory nerve function (Cianfrone et al., 2006).

Comparison of electrophysiological responses to extracellular stimulation in acutely and long-term deafened animals suggests that substantial changes in neural function do occur, but they are highly dependent on the details of experimental design. Some groups found increases in both auditory evoked brain stem and SGN single unit response thresholds with increasing pre-procedure duration of deafness in rats and cats (Shepherd et al., 2004; Shepherd and Javel, 1997) while another group observed the opposite relationship in Guinea Pigs (Sly et al., 2007). Single unit recordings from Shepherd et al.'s 2004 rat experiments show substantial variability of response latency and jitter between individual fibers but no significant effect of deafness duration, while those in Sly et al.'s 2007 Guinea Pig study exhibited decreasing response latency with duration of deafness. These results highlight the complex and potentially diverse changes in fiber electrophysiological properties after deafening and the need for a theoretical framework with which to ground an understanding of these changes.

Computational models of the CI electrode-neuron interface have the potential to create a mechanistic link between the anatomical and electrophysiological neural changes observed in animal models of HL. Ultimately, such an approach may help explain CI performance variance in human implant recipients. Previously, many studies of myelination and current spread have used analytical models to assess how subthreshold currents spread through fibers (Basser, 2004; Koles and Rasminsky, 1972; Rushton, 1951). While these analytical models can shed light on electrotonic effects, they cannot make any predictions about the suprathreshold behavior of fibers and do not account for the stochastic behavior of neurons introduced by small populations of ion channels; stochasticity that is critical to the dynamic range of populations of neurons (Chow and White, 1996;

Imennov and Rubinstein, 2009; White et al., 2000). More recently, empirically derived point-process models have been used to explore neural response to extracellular stimulation. These models are generally able to replicate the electrophysiological behavior of single neurons recorded in animal models and can encode amplitude-modulation information (Goldwyn et al., 2012; Joshua H. Goldwyn et al., 2010). More recently a similar model was extended to simulate both central and peripheral action-potential initiation, facilitating recapitulation of differential responses to opposite polarity monophasic stimuli as observed in cat neurons by Shepherd and Javel in 1999 (Joshi et al., 2017). However, the empirical nature of these models makes interpretation of individual parameters challenging, thus, it is difficult to make predictions regarding how parameters might be changed in different pathological states. Moreover, there currently exist no data exploring chronaxie or rheobase within chronically deafened animals with which to construct such phenomenological models.

In contrast, biophysical models, while more computationally intensive and harder to design, have parameters explicitly related to the physical and electrical properties of the neurons they attempt to simulate. As such, it is possible to predict how reduced internodal myelination would manifest in the model. Previous studies have explored the effect of peripheral process degeneration using this approach and observed shifts in site of action potential generation (Briaire and Frijns, 2006; Rattay et al., 2001b).

This model was selected for the following experiments because it is one of the simplest in which interactions between the spatial spread of current and inhomogeneities in the myelination of axons can be explored. In the present study, we first explored how different stimulus waveforms initiate responses in different locations in a sound level-dependent manner even in normal fibers. We then explored the effect of fiber internode myelination by systematically varying severity and distribution of myelin loss. The response properties of these different simulated fibers provide insight into the biophysical sources of changes observed in recordings from animal models of long-term sensorineural HL and shed light on psychophysical phenomena in human CI users. They may also constrain the types of variability in psychophysical outcomes that would be expected with such neural pathology.

2.2 Methods

2.2.1 Segmented cable model with stochastic channel behavior

The biophysical model used in this study represents the peripheral and central axons of Type 1 SGNs as a single segmented cable, as previously described (Imennov and Rubinstein, 2009; Mino et al., 2004; O'Brien and Rubinstein, 2016). Briefly, the membrane potential within each segment during stimulation by an extracellular electrode is described by a partial differential equation (Eq. 1) relating axial current to capacitive, leak, applied, and ionic currents according to Kirchoff's law (illustrated in Fig 1A):

$$\frac{-h^2}{R_a(x)}\frac{d^2V_m(x,t)}{dx^2} = C_m(x)\frac{dV_m(x,t)}{dt} - \frac{V_m(x,t)}{R_m(x)} + \frac{h^2}{R_a(x)}\frac{d^2V_{ext}(x,t)}{dx^2} + I_{ion}(x,t) \qquad (1)$$

Behavior of each of these currents is dictated by biophysical parameters, originally derived from anatomical and physiological data from model organism, principally feline, auditory nerves. Individual parameters were then allowed to vary within 10% of empirical values until simulated relative spread, spike latency, jitter, chronaxie, relative refractory period, and conduction velocity were within 10% of values recorded from felines in response to intracochlear electrical stimulation. The present study uses identical parameters to those used in Imennov and Rubinstein, 2009 except for the explicit changes described in Sections 2.2.2 and 2.2.3.

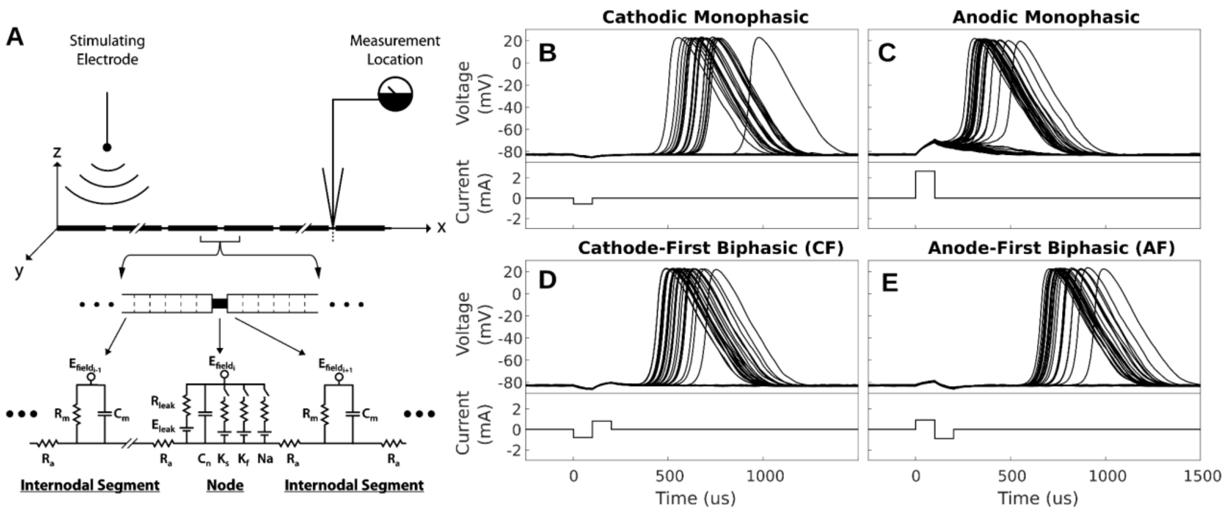
A
Stimulating Electrode
Measurement Location
z
x
y
$E_{field_{i-1}}$
E_{field_i}
$E_{field_{i+1}}$
R_m
C_m
R_{leak}
E_{leak}
R_a
C_n
K_s
K_f
Na
Internodal Segment
Node
Internodal Segment
Cathodic Monophasic
Anodic Monophasic
Cathode-First Biphasic (CF)
Anode-First Biphasic (AF)
B
C
D
E
Voltage (mV)
20
0
-20
-40
-60
-80
Current (mA)
2
0
-2
0
500
1000
1500
Time (us)

Figure 2.1- Responses of model neurons to monophasic and biphasic stimuli.

(A) Wiring diagram illustrates auditory nerve fibers modeled as segmented wires via a core-conductor approach. Each segment is characterized by its membrane resistance (R_{leak}), membrane capacitance (C_m), and axial resistance (R_a). Internodes are divided into 9 adjacent segments which have dynamics governed solely by passive. Node of Ranvier segments have additional voltage dependent elements for sodium channels (Na), fast potassium channels (K_f), and slow potassium channels (K_s); each of which are defined by channel density, channel conductance, ionic reversal potential, and the number of channels within the open state. Electrodynamics within each segment are expressed by relating axial, membrane leak, membrane capacitive, and ionic currents using Kirchoff's law (see Eq. 1). A stimulating electrode placed 3 mm from fiber over 10 node of Ranvier segment provides a field potential (E_{field}) that varies with distance from the electrode. Fibers are 36 nodes long, the approximate number of nodes between the feline auditory periphery and cochlear nucleus, and most recordings are taken from node 32. Reprinted with permission from Imennov and Rubinstein, 2009. **(B-E)** Responses recorded from node 32 of 36 of normally myelinated fibers (Rel. Myelination = 1) to 50 presentations of the 4 stimuli waveform types described. For each waveform type, current amplitude was selected to produce an action potential response probability of 0.50. Cathodic **(B)** and anodic **(C)** monophasic stimuli and responses are depicted in the top panels while cathode-first **(D)** and anode-first **(E)** biphasic stimuli and responses are depicted in the bottom panels.

Each fiber consisted of 36 nodes, with intervening internodes, the approximate number existing between the auditory periphery and cochlear nucleus of felines. Within the segmented cable model, myelinated internodal regions were divided into nine segments each of which possessed electrodynamics described completely by passive axial, leak, and capacitive currents. The biophysical parameters governing the behavior of a standard internodal segment are listed in Table 1. Internodal segment length, plasma membrane caliber, and axonal resistance remained constant for all described experiments while myelin thickness, membrane capacitance, and membrane resistance were experimentally manipulated as described in Section 2.2.2.

In contrast, nodes of Ranvier were represented as single segments possessing both passive elements and stochastic, voltage dependent ionic currents. The parameters governing nodal segment behavior were held constant at the values in Table 1. The behavior of stochastic, voltage-dependent ion channels within nodal segments was modeled using a Markov jump process (Gillespie, 1977; Mino et al., 2004; Mino and Grill, 2002). Total ionic current was defined as the sum of sodium, slow potassium, and fast potassium currents. This procedure enabled computationally efficient simulation of channel dynamics within each segment while maintaining an accurate representation of their stochastic behavior (White et al., 2000).

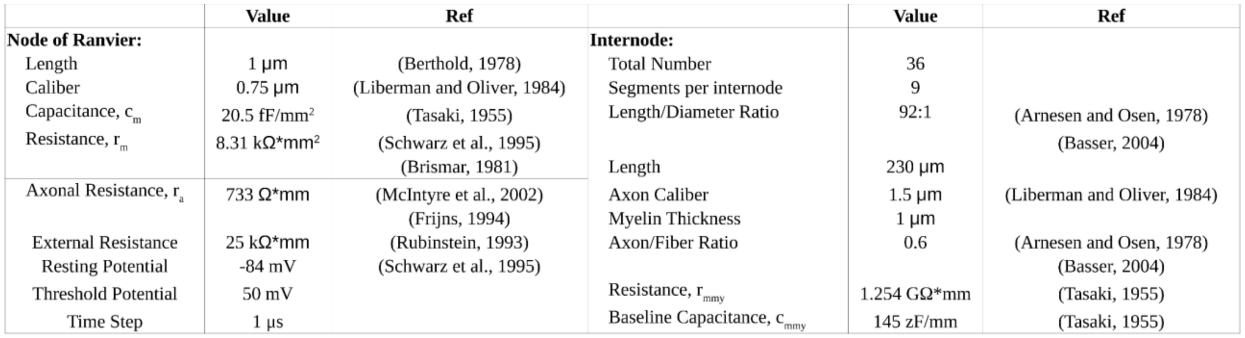

	Value	**Ref**		**Value**	**Ref**
Node of Ranvier:			**Internode:**		
Length	1 μm	(Berthold, 1978)	Total Number	36	
Caliber	0.75 μm	(Liberman and Oliver, 1984)	Segments per internode	9	
Capacitance, c_m	20.5 fF/mm^2	(Tasaki, 1955)	Length/Diameter Ratio	92:1	(Arnesen and Osen, 1978)
Resistance, r_m	8.31 kΩ*mm^2	(Schwarz et al., 1995)			(Basser, 2004)
		(Brismar, 1981)	Length	230 μm	
Axonal Resistance, r_a	733 Ω*mm	(McIntyre et al., 2002)	Axon Caliber	1.5 μm	(Liberman and Oliver, 1984)
		(Frijns, 1994)	Myelin Thickness	1 μm	
External Resistance	25 kΩ*mm	(Rubinstein, 1993)	Axon/Fiber Ratio	0.6	(Arnesen and Osen, 1978)
Resting Potential	-84 mV	(Schwarz et al., 1995)			(Basser, 2004)
Threshold Potential	50 mV		Resistance, r_{mmy}	1.254 GΩ*mm	(Tasaki, 1955)
Time Step	1 μs		Baseline Capacitance, c_{mmy}	145 zF/mm	(Tasaki, 1955)

Table 2.1- Morphological and biophysical parameters.

Simultaneous solution of numerical approximations of the system of differential equations described by Eq. 1, with the relevant ionic currents and applied field induced currents (described in section 2-3), by an implicit Crank-Nicholson scheme yields the potential within each segment of the model fibers for each time step of the simulation (Mino et al., 2004). A time step of 1 μs was used for all simulations. Simulations were performed using custom-built C code, using a MatLab wrapper for managing input parameters and analyzing output data.

2.2.2 Parameterization of demyelination

To adapt the model to simulate pathological alterations in SGN axons, we implemented a modified version of the core-conductor model of myelinated axons (Basser, 2004; Koles and Rasminsky, 1972). The core-model treats myelinated axons as a single-layer of resistive-capacitive medium separating resistive compartments. The membrane capacitance and resistance across internodal segments can then be described by Eqs. 2 and 3, respectively:

$$\frac{C_{my}}{L} = \frac{2\pi\kappa_{my}\epsilon_0}{\ln(D/d)} \tag{2}$$

$$\frac{R_{my}}{L} = \frac{\rho}{2\pi L}\ln(D/d) \tag{3}$$

Where κ_{my} is the dielectric constant of myelin, ρ is the resistivity of myelin, ε_0 is the permittivity of free space, D is the myelin sheath outer diameter, d is the plasma membrane diameter, and L is the length of the internode. From these relationships, the core-conductor model predicts a decrease in the internode membrane space constant and a fixed time constant with decreasing myelin thickness.

A shortcoming of this model is that membrane resistance approaches 0 and capacitance ∞ in the limit of complete myelin loss. We addressed this asymptotic behavior by incorporating the internodal plasma membrane resistance and capacitance in series with the myelin sheath's, creating a core-dual conductor model. Since the specific resistance of lipid bilayer without ion channels embedded in it is of a similar order to that of myelinated axon (10^6-10^8 ohm*cm^2 and 4.45*10^8 ohm*cm^2, respectively), we chose to fix resistance as we decreased myelin width (Imennov and Rubinstein, 2009; Montal and Mueller, 1972). Assuming the plasma membrane dielectric constant remains consistent between nodal and internodal segments, the plasma membrane capacitance of the internode can be estimated using the nodal value divided by the constriction factor. The total internodal capacitance can then be calculated by adding the plasma membrane and myelin contributions in series:

$$\frac{1}{C_{internode}} = \frac{1}{C_{my}} + \frac{1}{C_{m,internode}} = \frac{\log(D/d)}{\log(1/0.6)C_{my,normal}} + \frac{c_{constric}}{C_{m,node}} \tag{4}$$

This procedure for varying membrane capacitance while freezing membrane resistance to simulate changes in myelin width produces similar capacitance values to the simple core-conductor model for most values of D but preserves finite capacitance in the limit of no myelination (Fig 2C). Fixing the resistance leads to substantial differences in predicted resistance between the models at extreme amounts of demyelination as well. A consequence of these changes is that this model predicts a constant, static space constant for demyelinated fibers but a monotonic increase in time constant with reduced myelin thickness.

Using this novel approach to calculate internodal membrane capacitance and resistance we modified a single model peripheral axon's membrane capacitance to represent many gradations of demyelination, diagrammed in Fig 2A. This procedure can be applied to any subset of internodes, enabling us to simulate anything from partial, solely peripheral demyelination to complete demyelination of the entire fiber, see Fig 2B.

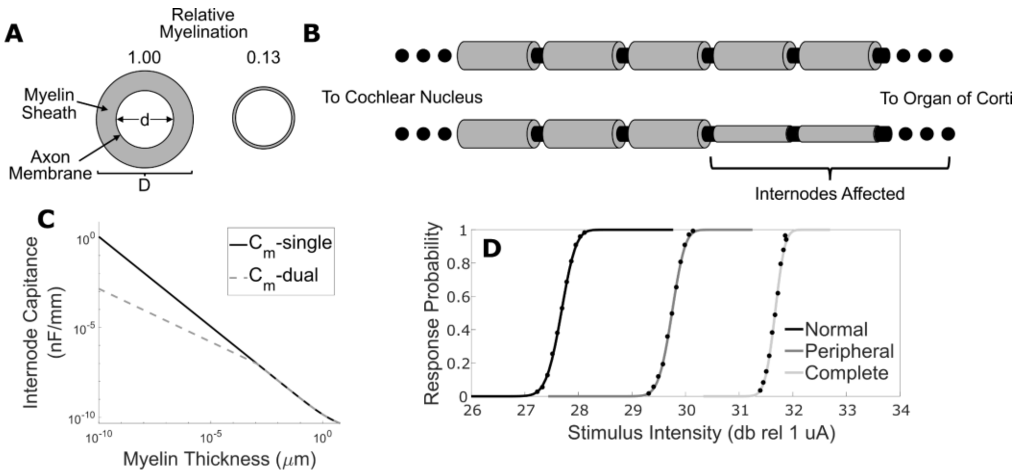

Figure 2.2- Demyelination shifts input-output functions of fibers**.** Using our approach to calculate internodal membrane capacitance presented (Eq. 8) it is possible to modify a single model peripheral axons' membrane capacitance to represent any gradation of demyelination **(A)**. This procedure can be applied to any subset of internodes, enabling simulation of anything from peripheral to complete demyelination **(B)**. **(C)** Internodal specific capacitance calculated by dual conductor (solid black) and single conductor (dashed grey) models is plotted as a function of myelin thickness for a 1.5 µm caliber fiber. **(D)** Input-output functions illustrating response probability plotted as a function of monophasic cathodic stimulus current pulse intensity are presented for normal, peripherally demyelinated (95% reduction in myelin width impacting first 10 internodes), and centrally demyelinated (95% reduction in myelin thickness impacting first 28 internodes) fibers.

2.2.3 Application of extracellular currents

Simulated SGN axons were stimulated by an extracellular disk electrode as derived previously by Rubinstein and used in previous versions of this model (Imennov and Rubinstein, 2009; Mino et al., 2004; O'Brien et al., 2016; Rubinstein, 1988). Briefly, by assuming that injected current propagates through an isoresistive medium, the applied potential difference between adjacent segments can be expressed as a function of the injected current and the segment-electrode distance. The field potentials along the fiber can then be calculated for each time step during stimulation for a selected current waveform. In the present study, fibers were presented with one of 4 different stimulation waveforms following a delay of 1 ms. Initial experiments were performed with simple monophasic 100 μs pulses of either cathodic or anodic polarity, as used in Miller et al. 1999, to facilitate ease of interpretation (waveforms illustrated in Fig 1B & C, lower panels) (Miller et al., 1999). Subsequently, charge balanced, biphasic pulses with either anodic (AF) or cathodic (CF) phase first (Fig 1D & E, lower panels, respectively, no inter-phase gap, and 100 μs/phase duration were used for their relevance to the stimulation paradigm used in CIs and for comparison to recordings from animal models of SNHL (Galvin and Fu, 2009; Shannon, 1992; Shepherd et al., 2004; Shepherd and Javel, 1999). Following stimulus presentation, simulations were continued for 4 ms to enable monitoring of fiber-potential evolution. For each stimulus waveform, amplitudes were selected to produce the desired response probabilities for a block of simulations.

2.2.4 Stimulus selection and response analysis

For each fiber-stimulus waveform pair, an iterative process was used to identify the current-pulse amplitudes required to produce action potentials with a range of response probabilities. We first identified the stimulus amplitudes between which a fiber's response probability varied between 0 and 1 using coarse sampling of currents between 0.5 mA and 150 mA using 25 Monte Carlo simulations per fiber-intensity pairing. After identifying this initial range, we linearly sampled the current-amplitude space between these two stimulus intensities using blocks of 500 Monte Carlo simulations per pairing. The amplitude range tested was refined until the resulting stimulus input/response probability output curve could be fit with a cumulative normal distribution function (CDF) using least-squares fitting. We define the stimulus intensity at a response probability of 50%, the CDF mean (μ), as threshold. Relative spread (RS), a measure of dynamic range, was defined as the CDF variance (σ) divided by its mean. The CDF defined threshold and RS were used to further refine the range of stimulation intensities and the 500 block simulations repeated until sampling between threshold – 2*RS and threshold + 2*RS resulted in no substantial trial to trial variation in calculated threshold or RS.

For each fiber-stimulus pair, the latency between stimulus onset and threshold crossing at the recording node (node 32) was calculated for each trial generating an action potential. From this distribution of latencies, the mean latency and jitter (latency standard deviation) were calculated for each stimulus amplitude. The described simulation enables recording of potentials within each segment of the fiber. By identifying the segment in which the membrane potential first crosses threshold, the node of Ranvier responsible for action potential generation was found for each trial. From the resulting distribution of initiation sites, the mean initiation site and variance in initiation location were calculated.

The latency of response arrival at the recording node was decomposed into initiation and conduction delay components. Initiation delay is defined as the time interval between stimulus onset and the first action potential arising within a fiber node, termed the initiation node. Conduction delay is defined the time interval between the first action potential initiation and action potential arrival at the predefined recording node. From these quantities, the mean conduction velocity of action potentials between the initiation and recording nodes can be determined via Eq. 5:

$$\langle \boldsymbol{V_{conduction}} \rangle = \frac{\boldsymbol{d_{internodal}} * (\boldsymbol{N_{Rec}} - \boldsymbol{N_{Ini}})}{(\boldsymbol{t_{Rec}} - \boldsymbol{t_{Ini}})} \qquad (5)$$

2.2.5 Simulating interaural timing difference detection

To explore potential ramifications of demyelination on fine temporal cue encoding, we simulated the ITD distributions produced by delivery of biphasic pulses to different fibers, which in this case represent the populations of neurons nearest corresponding electrodes in 'left' and 'right' simulated cochlea. For each case, normal fibers were used in the left cochlea while those of the right were variably demyelinated. AF biphasic pulses, intensity matched by response probability, were then delivered simultaneously bilaterally. The distribution of ITDs produced by repeatedly subtracting a randomly selected right fiber latency from one from the left over 1000 trials is presented.

2.3 Results:

2.3.1 Different passive responses to opposing polarity currents drive stimulus-dependent variation in fiber sensitivity

To better understand how CI stimulation is encoded by SGNs we first explored the response patterns of normal fibers to different stimulus waveforms. Membrane potential responses of normally myelinated fibers (myelin thickness = 1 μm) to cathodic monophasic, anodic monophasic, CF biphasic, and AF biphasic stimuli are illustrated in Figure 1B-E, upper panels. For each waveform type, current amplitude was selected to produce an action potential firing efficiency of 0.50. Note responses to all four stimulus types exhibit a passive, deterministic-appearing behavior at the recording site that is hyperpolarizing for cathodic polarity pulses and depolarizing for anodic ones. Viewed as a function of distance from the electrode (data not shown), these passive responses consist of depolarization and hyperpolarization of the fiber immediately underlying the electrode, for cathodic and anodic pulses respectively, with an opposing shift in membrane potential along the more central axon. This predominantly passive response is followed probabilistically by an action potential of variable, but stimulus dependent, latency. Other trials exhibit no membrane potential change during this latter period, indicating response failure.

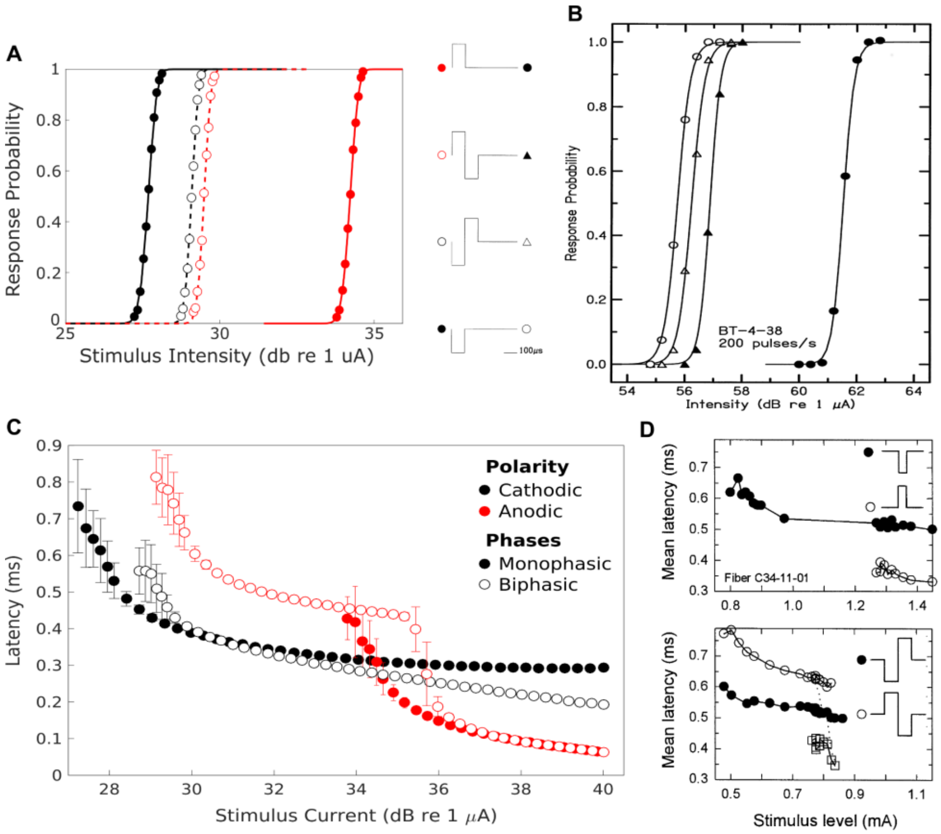

Figure 2.3- Normal fiber input-output curves and latencies vary with stimulus waveform. **(A)** Response probability averaged over 500 Monte Carlo trials, of normal simulated fibers to varying current intensities of cathodic monophasic, anodic monophasic, cathode-first biphasic, and anode-first biphasic stimuli (markers). These response profiles are fit with a CDF (lines). **(B)** Input/output functions using similar stimuli produced from recordings from spiral ganglion central axons in response to intracochlear electrical stimulation by Shepherd and Javel in 1999 for comparison (reprinted with permission). **(C)** Mean latency between stimulus onset and action potential arrival at node 32 is plotted as a function of stimulus current for each of the 4 stimulus waveforms applied to normally myelinated fibers (n = 500 monte carlos). Error bars represent jitter, the variance of the latency distribution. Solid markers and lines correspond to monophasic stimuli while empty markers and dashed lines correspond to biphasic stimuli. Black markers and lines indicate waveforms with cathode leading phases while red ones indicate anodic leading phases. **(D)** Latency-intensity functions for responses to monopolar stimuli recorded from cats by Miller and Colleagues. Monophasic pulses (top panel) were 39 µs in duration while biphasic stimuli (bottom panel) were 100 µs/phase with no interphase gap. Cathodic monophasic and CF stimuli plotted as filled markers while anodic monophasic and AF plotted as open markers. AF latencies separated into long (open circles) and short (open squares) populations. Adapted, with permission, from Miller et al., 1999.

To more thoroughly characterize the interaction between stimulus-waveform, intensity, and fiber responses; Figure 3A contains plots of the response probabilities of normal fibers as functions of current intensity for the four stimuli. The stimulus intensity necessary to produce a given response probability is substantially lower for cathodic than anodic monophasic stimuli ($\text{Thresh}_{\text{Cathodic}}$ = 27.68 and $\text{Thresh}_{\text{Anodic}}$= 34.23 dB re 1 µA). Biphasic stimuli generated input-output functions falling between these extremes but substantially closer to the cathodic monophasic curve ($\text{Thresh}_{\text{CF}}$ = 29.09 and $\text{Thresh}_{\text{AF}}$ = 29.50 dB). This reflects the fact that the depolarizing center of the cathodic phase of biphasic pulses initiates action potentials in the periphery (data not shown). The biphasic stimuli result in thresholds elevated with respect to the cathodic monophasic stimulus due to the hyperpolarizing effects of the adjacent anodic phase; an effect modestly more prominent with the AF biphasic stimulus type. Input-output functions to the monophasic pulses possessed similar RSs ($\text{RS}_{\text{cathodic}}$ = 0.0506 vs $\text{Rs}_{\text{anodic}}$=0.0499) while those to biphasic pulses exhibited substantially lower values (RS_{CF} = RS_{AF} = 0.0402). This modest decrease in dynamic range for the biphasic pulses reflects the requirement that the depolarizing stimulus be sufficiently large to overcome the antecedent or subsequent hyperpolarizing phase. These simulation observations qualitatively resemble the input/output functions produced from recordings of spiral ganglion central axons in response to intracochlear electrical stimulation by Shepherd and Javel in 1999 (Fig 3B). Although Shepherd and Javel used a bipolar electrode configuration for these recordings and the present simulations use a monopolar configuration, at the single fiber level the qualitative similarity in relative threshold sensitivity is notable.

2.3.2 Suprathreshold initiation site shifts lead to decreases in AF stimulus induced response latencies

The different distributions of passive responses also lead to variations in action potential initiation site that drive stimulus specific response timing characteristics. Latency between stimulus onset and central action potential arrival is plotted as a function of current magnitude for each of the stimuli applied to normal fibers in Figure 3C. For all stimulus waveforms, fiber response latency and jitter initially decrease with increasing stimulus intensity. Each stimulus waveform produces responses with characteristic mean latency at threshold. Responses to solely anodic stimuli exhibit the shortest latency at threshold (0.3607 ms) due to central action potential initiation. Cathodic stimuli produce responses with substantially longer latency (0.6336 ms), resulting from peripheral initiation and conduction delay. Biphasic pulses also initiate action potentials at this node closest to the electrode but are subject to pulse sequence-dependent effects. CF biphasic pulses produce responses with a shorter latency (0.5230 ms) compared to monophasic cathodic pulses owing to the more intense current at threshold required to initiate action potentials before the onset of the hyperpolarizing phase. In contrast, AF biphasic stimuli produce responses delayed by 199 μs (0.7535 ms) relative to monophasic cathodic stimuli due to the combined effect of the first phase duration and the requirement to overcome the consequent hyperpolarization.

Latencies of responses also vary with stimulus type at intensities above threshold. Response latencies to cathodic and anodic monophasic stimuli decay with growing current intensity until they asymptote to minima, (approximately 290 and 60 μs respectively). Biphasic stimuli induced response latencies exhibit more complex behavior. Initially they decay at a similar rate to cathodic monophasic stimuli, however, instead of approaching an asymptote, the latter demonstrate polarity order-dependent behavior. Increasing CF biphasic pulse currents produces a near linear reduction in latency due to the anodic polarity pulse facilitating conduction of the peripherally generated stimulus. In contrast, latencies to AF biphasic stimuli initially approach a local minimum before exhibiting an abrupt and dramatic decrease in latency near the threshold for anodic monophasic stimuli. Additional increases in current intensity result in another exponential decay phase that parallels that of anodic monophasic responses. This pattern of latency changes is produced by an abrupt transition from peripheral AP initiation by the cathodic phase to central initiation by the preceding anodic phase.

These simulated latency findings exhibit marked similarity to the latency-stimulus functions recorded from cats in response to monopolar stimulation by Miller et al. (Fig 3D) (Miller et al., 1999).

Responses to monophasic stimuli (top panel) exhibit lower latency, albeit with higher threshold, to anodic stimuli. Latencies for both monophasic stimuli initially decrease with increasing stimulus intensity but ultimately approach asymptotic values; asymptotic anodic monophasic latencies are ~200 µs shorter than those for cathodic monophasic stimuli. Response latencies to biphasic stimuli (lower panel, different fiber) instead exhibit either a gradual decline, for CF stimuli, or gradual decay punctuated by an abrupt shift to shorter latency, for AF stimuli. As with the simulation results, responses to AF stimuli with intensities in this transition region exhibit bimodal latency distributions (separately plotted in Fig 3D, bottom panel).

2.3.3 Moderate demyelination negligibly impacts thresholds and only modestly alters timing

Input-output functions illustrating response probability plotted as a function of monophasic cathodic stimulus current pulse intensity are presented in Fig 2D for normal, peripherally demyelinated (95% reduction in myelin width impacting first 10 internodes), and centrally demyelinated (95% reduction in myelin thickness impacting first 30 internodes). Peripheral demyelination results in an elevated threshold (29.75 dB) relative to the normal fiber (27.68 dB) with a reduced relative spread (0.045 vs 0.051). Demyelination extended to involve the central internodes of the fiber causes a further increment in threshold (31.67 dB) and decrement in dynamic range (RS = 0.034).

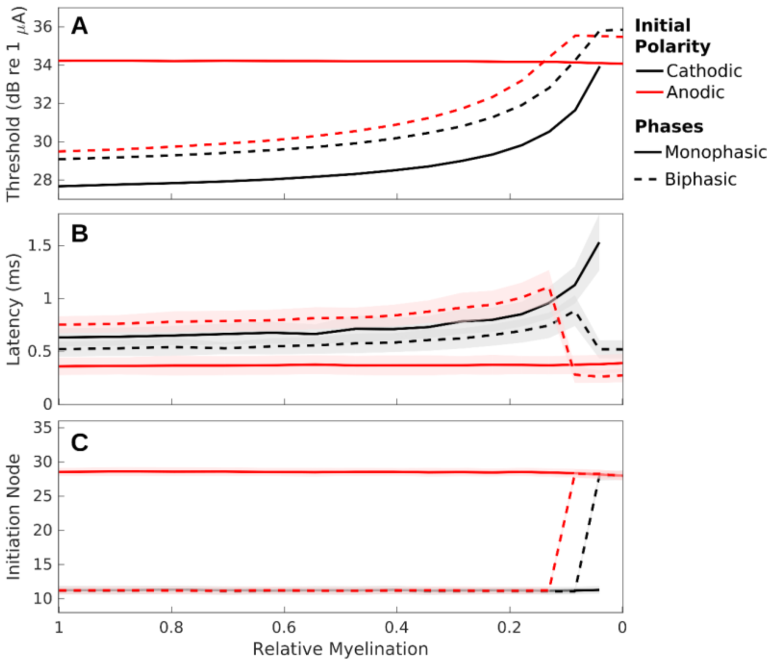

Figure 2.4- Peripheral demyelination alters fiber sensitivity, response timing, and initiation site**.**

Response properties to cathodic (solid black) and anodic (solid red) monophasic stimuli and cathode-first (dashed black) and anode-first (dashed red) biphasic stimuli are presented as a function of myelin thickness for demyelination affecting the first 16 internodes. **(A)** Thresholds (mean of CDF fit to input-output function) plotted in units of decibels relative to 1 µA. **(B)** Mean latencies at threshold with error representing jitter. **(C)** Mean initiation sites at threshold with error represent initiation site variance. Myelin thickness is plotted on the abscissa, with normal myelination corresponding to a thickness of 1 µm, on the left, and complete demyelination to 0 µm, on the right. Each data point derived from 500 Monte Carlo simulations with a set of fiber-stimulus pairings.

To explore the impact of demyelination in finer detail; Figure 4 presents thresholds (A), mean latencies at threshold (B), and mean initiation sites at threshold (C) to cathodic and anodic monophasic stimuli and CF and AF biphasic stimuli as a function of myelin thickness for peripheral demyelination affecting the first 16 internodes. Modest amounts of demyelination, <~50% reduction in myelin width, produce only minute changes in threshold (<0.5 dB in all cases) and modest changes in latency (64 μs and 113 μs for peripheral and central, respectively) for the cathodic stimulus type. Anodic stimulus-induced response thresholds and latencies do not change at all in the case of peripheral demyelination; however, centrally demyelinated fibers exhibit modest changes in threshold (0.31 dB) and latency (46 μs) with <50% reduction in myelin thickness to this stimulus type. With these modest amounts of demyelination, initiation site means and variances for the different stimulus types remain constant. Cathodic monophasic and biphasic stimuli all initiate APs at a mean location of about node 11 while anodic monophasic stimuli initiate action potentials centered around node 28.

2.3.4 Severe peripheral demyelination alters response properties to cathodic, but not anodic, monophasic stimuli

More severe peripheral demyelination leads to profound changes in sensitivity to cathodic monophasic stimuli (Fig 4A). A 96% reduction in myelin thickness produces an approximately 6.27 dB threshold increase while complete loss leads to failure of the fiber to conduct action potentials. This increase in threshold is accompanied by a concomitant decrease in dynamic range with RS reduced to 50% of normal. Even with this extreme level of peripheral demyelination anodic thresholds and RS remain unperturbed.

Severe peripheral demyelination also dramatically altered response timing to cathodic but not anodic monophasic responses (Fig 4B). Cathodic response latency increased exponentially with reduced myelin thickness up to a loss of 96%. Again, in the absence of myelin fibers cannot initiate or propagate action potentials. Response jitter decreases for the changes in myelin thickness producing exponential increases in latency. In contrast, anodic monophasic stimuli induced response latency and jitter remain nearly constant over the entire range of myelin thicknesses for peripheral loss. The mean site of action potential initiation, at threshold, for cathodic and anodic monophasic pulses remained constant (Fig 4C), except for parameter pairings where cathodic stimuli failed to produce responses.

2.3.5 Response properties to biphasic pulses exhibit discontinuous non-monotonic changes with severe peripheral demyelination

While at least 13% of myelin remains, response thresholds and latencies to the 2 biphasic waveforms (black and red dashed traces) nearly parallel those to cathodic alone (Fig 4A&B). Initial thresholds and latencies exhibit the relatively small translations due to the waveform-dependent effects presented in section 3-1. As with cathodic monophasic stimuli, response threshold increases, and RS decreases, in a monotonic fashion for these biphasic stimuli with peripheral demyelination until myelin loss becomes severe (<13% remaining). This relationship ultimately results in substantially elevated thresholds, with increases of 5-6 dB between thresholds for normally myelinated fibers and those demyelinated by 90%. With still more extreme peripheral demyelination, thresholds for CF and AF stimuli plateau. These plateaued thresholds parallel the near constant thresholds of fibers to anodic monophasic stimuli. While normal fibers are more sensitive to CF than AF stimuli, this relationship becomes inverted for fibers with sever myelin loss resulting in greater relative sensitivity to AF stimuli.

Mean latencies of responses to these biphasic pulses increase approximately exponentially with decreasing myelin thickness up to this limit as well (Fig 4 B). With more severe demyelination (>87% reduction in myelin thickness) responses to biphasic pulses exhibit abrupt non-monotonic changes, deviating significantly from the patterns observed with cathodic monophasic stimuli.

Plateauing of biphasic response thresholds in the setting of peripheral demyelination is accompanied by dramatic decreases in mean response latencies. CF stimuli response latencies increase with severity of peripheral demyelination from a baseline of 0.52 ms to a maximum of 0.85 ms with 92% demyelination. With >92% myelin loss, this latency abruptly drops back to 0.51 ms. Likewise, AF response latency is 0.75 ms at baseline, increases to a maximum value of 1.11 ms with 87% demyelination, and then abruptly drops to 0.28 ms with 92% or greater myelin loss. The low latencies of these heavily affected fibers are similar to the constant latency exhibited by responses to anodic monophasic pulses, even when peripheral myelin is absent. These observed non-monotonicities in response latencies to biphasic pulses as demyelination becomes more severe are driven, principally, by changes in the site of action potential initiation (data not shown). Both cathode-first and anode-first stimuli abruptly transition from initiating action potentials peripherally to centrally with severe loss of myelin.

2.3.6 Both initiation and conduction delay are prolonged in demyelinated fibers

With demyelination affecting 12-20 nodes, AF pulses produce responses that increase in mean latency of responses at threshold as loss of myelin becomes more severe, up to the abrupt transition to central initiation with extreme myelin thinning. This increase in latency reflects both a modest increase in the conduction delay along the fiber (Fig 5a), reflecting a modest reduction in conduction velocity (Fig 5b), and a more substantial and variable delay in initiation. The abrupt transition to central initiation corresponds with a dramatic decrease in conduction delay, due to both a reduction in the distance action potentials need to travel and increased conduction velocity due to the broad nature of the depolarizing surround facilitating conduction. The high variability in conduction velocity at these extreme values results from rounding errors introduced in the small interval between initiation and recording due to the discrete time steps of the simulation.

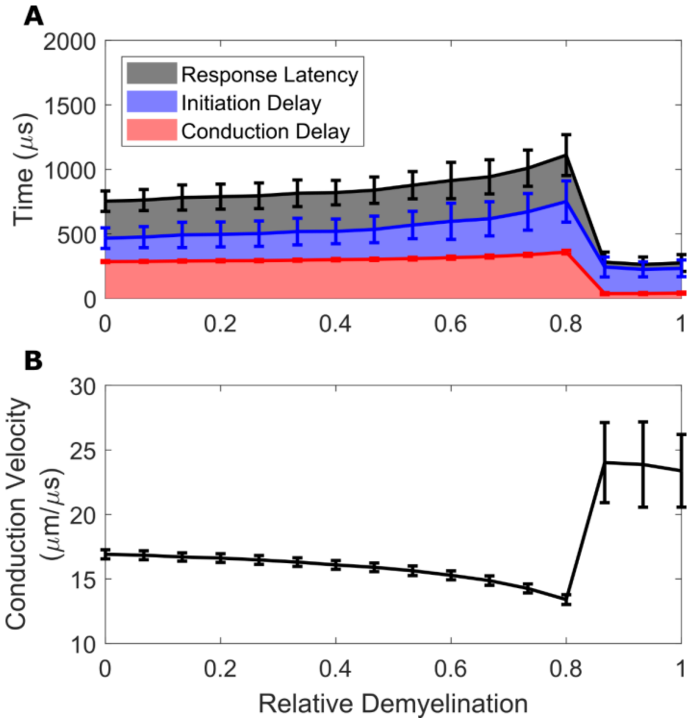

Figure 2.5- Initiation and conduction delays both contribute to latency changes**.** Response mean delays **(A)** and conduction velocity **(B)** are presented for responses to AF stimuli as a function of relative demyelination severity affecting the peripheral-most 16 nodes. **(A)** Latencies represent the elapsed simulation time between stimulus onset and recording node AP arrival (black); initiation delays that between stimulus onset and first AP threshold crossing at any node (blue), and conduction delays that between initiation time and recording node AP arrival (red). **(B)** Mean conduction velocity during conduction delay. Error bars represent standard deviations.

2.3.7 Thresholds are robust to demyelination

Visualizing the entire parameter space created by varying myelin width and the number of internodes affected provides additional insight into the impact of demyelination on response properties. Response thresholds, plotted in Fig 6, generally demonstrate a surprising robustness to the demyelination procedure but become dramatically elevated with extreme demyelination. Cathodic, CF, and AF waveforms (A,B,&C, respectively) produce responses with thresholds of 27.68, 29.09, and 29.49 dB in normal fibers, respectively. With demyelination affecting less than 10 internodes these thresholds change by less than 5 dB regardless of degree of myelin thinning. Conversely, when myelin thickness is at least 50% of normal, thresholds for these stimulus types change by less than 4 dB regardless of the number of internodes affected. Threshold changes for these stimuli types only become functionally important with greater than ~70% loss of myelin involving at least the 10 most peripheral internodes. While the baseline threshold for anodic monophasic stimuli (B) is substantially higher than for the other stimuli types (34.22dB), modified fiber thresholds show even greater robustness, only exhibiting elevation of at least 5 dB with greater than 90% demyelination of the entire fiber.

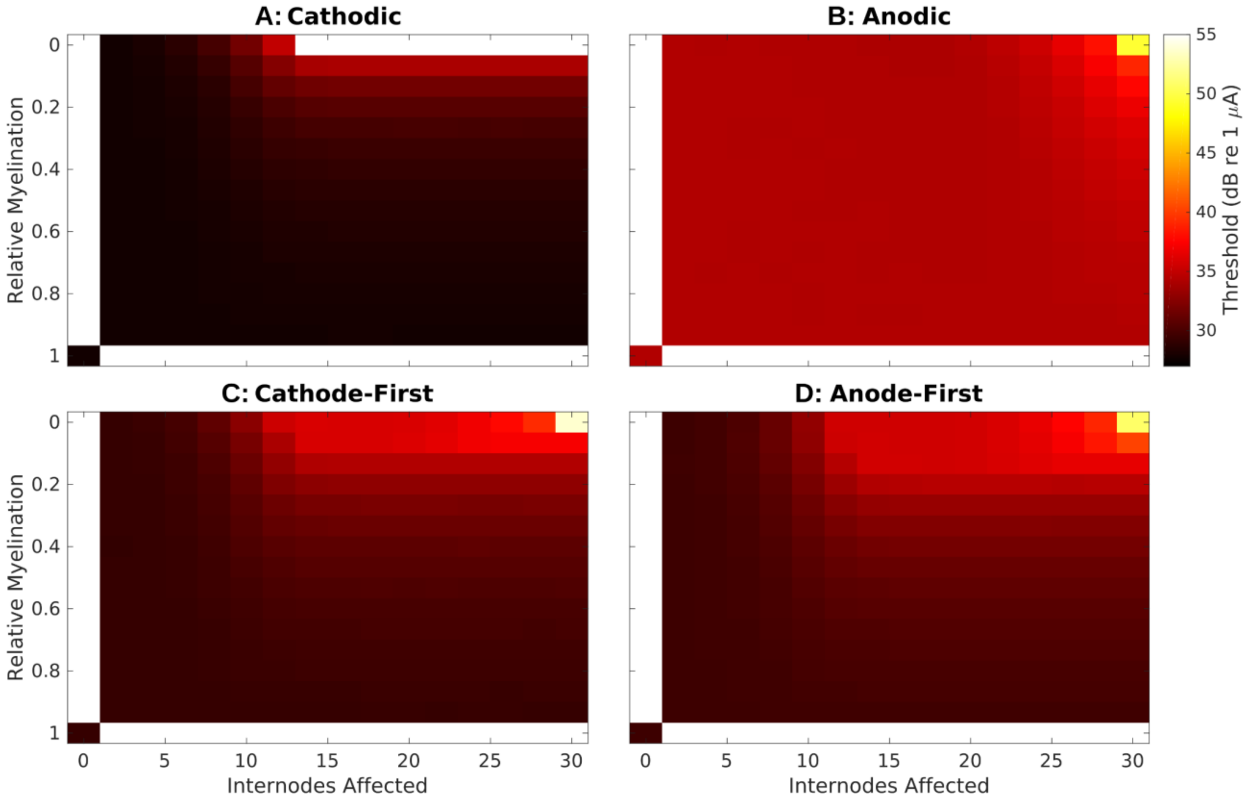

Figure 2.6- Thresholds vary with both severity of demyelination and stimulus waveform. Threshold (color-mapping) is presented over the entire variable space created by the parameters of myelin thickness (ordinate) and number of internodes affected (abscissa) for each stimulus tested. Thresholds for monophasic stimuli are presented in the top two panels, cathodic in **(A)** and anodic in **(B)**, while those for biphasic stimuli are presented below, cathode-first in **(C)** and anode-first in **(D)**. Response thresholds for normal fibers are presented in the bottom left corner for each waveform. Myelin thickness decreases moving up the ordinate and number of internodes affected (beginning peripherally) increases along the abscissa, resulting in maximal demyelination in the top right.

2.3.8 Varying the number of internodes demyelinated alters threshold, dynamic range, and response latency in polarity-dependent manner

When demyelination impacts more than the 10 most peripheral nodes of a fiber, cathodic stimuli produce responses that increase in threshold (Fig 6A) and decrease in dynamic range (data not shown) with decreasing myelin thickness. The magnitude of this effect becomes more dramatic as additional internodes are involved until with 14 or more affected the relationship becomes that described in section 3-4 for 16 internodes affected. A complete absence of myelin involving at least the first 14 internodes prevents action potentials at the recording node due to initiation and conduction block. These increasing thresholds coincide with decreases in dynamic range (data not shown).

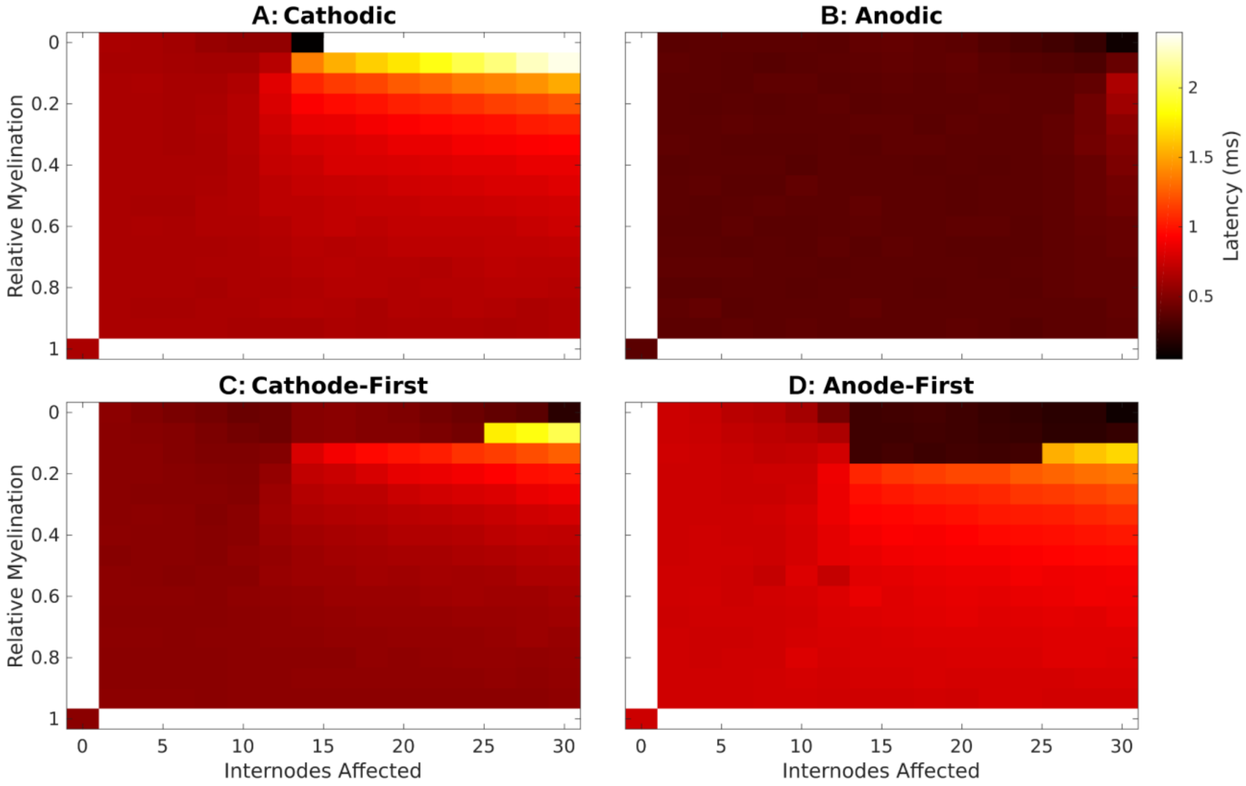

Figure 2.7- Response latencies varies with both severity of demyelination and stimulus waveform.

Mean response latency, at threshold, is plotted as described in Fig 6.

Mean latencies of responses to cathodic monophasic stimuli, at threshold, (Fig 7A) demonstrate substantially greater sensitivity to this demyelination procedure. While demyelination affecting less than the 10 most peripheral internodes generally has little effect on mean latency regardless of severity, once demyelination involves more than 10 internodes, latency increases in a manner proportional to the number of internodes affected and exponentially related to the decrease in myelin thickness.

Unlike in the case presented in 3-4, responses to anodic monophasic stimuli can be impacted by broad demyelination provided it impacts more than the most peripheral 20 internodes. Generally, the pattern of threshold (Fig 6B) and latency (Fig 7B) changes seen in fibers with varying myelin thickness applied to the entire fiber in response to anodic stimuli parallels the changes observed with peripheral demyelination and cathodic monophasic stimuli. At the extreme of complete fiber involvement, as myelin thickness decreased responses to anodic stimuli exhibited monotonic increases in threshold, ultimately resulting in a 15.09 dB threshold change, and 70% reduction in relative spread. Response latency first increases modestly with loss of myelin, up to 96% reduction, but then decreases to near 0 ms as the site of initiation shifts to the recording site.

Despite these observed changes in response latencies, mean initiation sites for monophasic stimuli change only in the most extreme limit of myelin loss. Cathodic monophasic pulses initiate action potentials almost exclusively at the peripheral site underlying the electrode with only a modest shift to more central nodes in regions of the parameter space adjacent to where conduction failure begins. Anodic monophasic pulses, in contrast, produce responses exclusively at more central locations with a shift even further centrally with complete demyelination.

2.3.9 Non-monotonicities in biphasic response properties are consistent across a broad range of extents of demyelination

Whereas response thresholds and latencies to cathodic monophasic stimuli increase exponentially with decreasing myelin thickness affecting at least 14 internodes until failure of action potential generation occurs, those to biphasic stimuli initially follow similar exponential trajectories but then exhibit dramatic non-monotonicities. The relative myelination corresponding to this transition differs with polarity order; this transition generally occurs for CF and AF stimuli with relative myelinations of 0.08 and 0.13 respectively. Thresholds in this region are of the same order, but slightly larger than, the corresponding thresholds for anodic monophasic stimuli. With this transition, the relative sensitivity of fibers to CF and AF pulses is inverted, with AF producing lower thresholds. The dynamic ranges of responses to biphasic stimuli follow those for cathodic monophasic, except for the lower baseline RS described previously, prior to the inflection point. With more severe myelin loss, response dynamic ranges to these pulse types abruptly increase to near that for normal fibers. More central demyelination involvement results in further decreases in the RSs of responses to biphasic stimuli, following a similar pattern to those for anodic monophasic stimuli in this regime.

As with monophasic pulses, demyelination affecting less than the 10 most peripheral internodes has inconsequential impact on mean latency regardless of severity for biphasic stimuli. With loss affecting 12 or more internodes, coincident with the changes in threshold and dynamic range, mean response latencies to biphasic stimuli initially increase as relative myelination decreases up to the mentioned inflection regions. With more pronounced myelin thinning, mean latencies to biphasic pulses precipitously drop to values comparable to those produced by monophasic anodic stimuli. The net effect is that biphasic response latencies exhibit abrupt transitions between extremely high and low latency with modest change in applied demyelination for some regions in the parameter space explored.

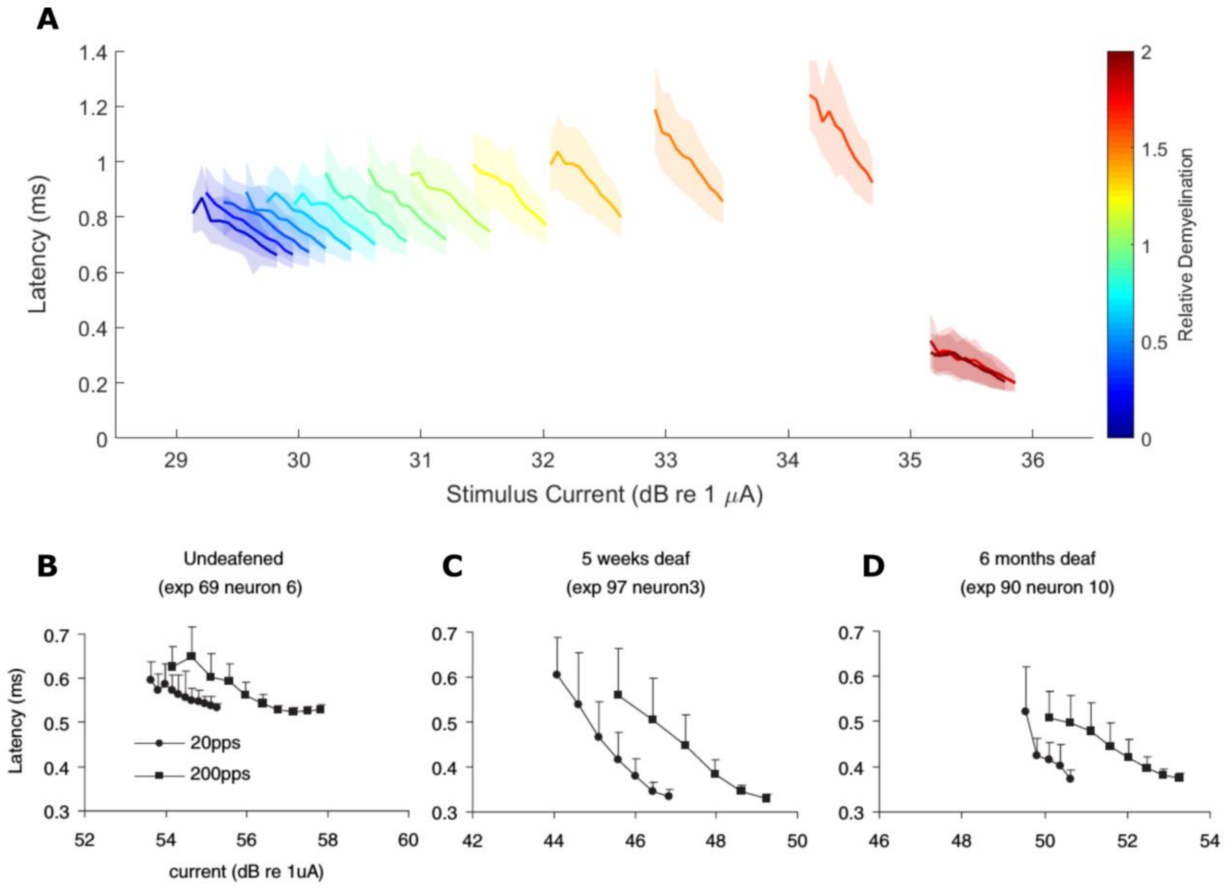

Figure 2.8- Response Latency-Stimulus Intensity Function Slopes Change with relative myelination. **(A)** Mean response latencies (solid lines) ± jitter are plotted for fibers with different degrees of relative demyelination (color-mapping) as a function of stimulus current. **(B-D)** Mean latency ± jitter of single fiber responses recorded from guinea pigs deafened either acutely **(B)**, 5-weeks **(C)**, or 6-months **(D)** prior to implantation by Sly and colleagues. Cathode-first biphasic pulses were 50 µs/phase with a 10 µs interphase gap using a monopolar electrode configuration. Circles and squares represent pulses delivered at 20 and 200 pps, respectively. Adapted, with permission, from Sly et al., 2007.

Demyelination changes the slope of latency-intensity curves in addition to the threshold magnitude (Fig 8A). The slope of these functions becomes steeper with loss of myelin thickness until myelin thickness loss that produces an abrupt drop in latency for biphasic pulses in the setting of peripheral myelin loss. Thereafter, the slope of these functions returns to approximately that of normally myelinated fibers. This pattern of latency-intensity slope changes is consistent with the findings of Sly and colleagues from single unit recordings from SGN central axons in guinea pigs; they observed a steeper response latency-stimulus intensity slope in an animal deafened for 5 weeks prior to implantation (C) when compared to an acutely deafened control (B). A chronically (6 mo.) deafened animal's responses (D) exhibited shallow slopes, similar to the control animal's, at 200 pulses-per-second (pps) but a slope similar to the 5-week deafened animal at 20 pps.

These abrupt non-monotonicities in response properties to biphasic pulses are driven largely by a shift in initiation sites (data not shown). Mean site of action potential generation for these stimuli depend on the precise combination of myelin thickness and number of internodes affected. For most of the variable space, these action potentials are initiated at the periphery, immediately under the stimulating electrode. Beyond the inflection region, fibers abruptly become more sensitive to action potential initiation at more central nodes.

2.3.10 Specific patterns of demyelination lead to pronounced increases in jitter and, in specific cases, bimodal latency distributions

Response jitter at threshold increases across most of the demyelination variable space, for cathodic, CF, or AF stimuli (Fig 9A, AF shown). Fibers with dramatic myelin loss that have not quite reached the inflection region show substantially elevated spread of latencies (Fig 9B compare middle to bottom, normal). Jitter then abruptly declines for fibers activated by biphasic pulses when demyelination becomes severe enough in the periphery to shift response initiation centrally (Fig 9, top).

Supra-threshold response jitters (Fig 9D) are generally much lower due to both more consistent sites of initiation and closer to deterministic ion channel dynamics. However, fibers with specific combinations of demyelination parameters activated by biphasic pulses, in the presented case AF, show profoundly elevated jitter. Histograms of response latencies for these conditions (Fig 9C, middle and top) show bimodal distributions in contrast to the unimodal distributions for normal fibers (Fig 9C, bottom).

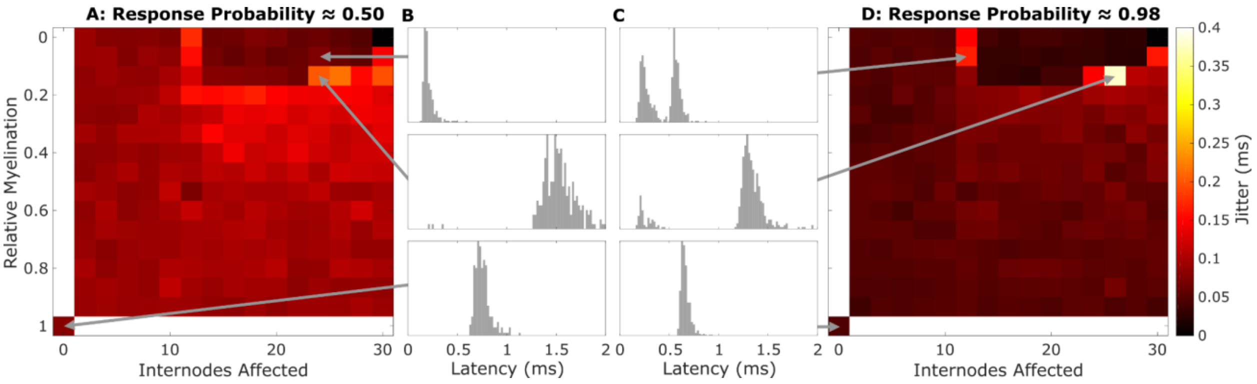

Figure 2.9- Response jitter elevated by slowed electrodynamics and multiple initiation sites**.** Jitter, standard deviation of response latencies, is plotted over the variable space described in Fig 5 for AF biphasic stimuli at threshold **(A)** and suprathreshold **(D)**. **(B)** and **(D)** show histograms of response latencies for the indicated fiber-stimulus pairings with a window of 0-2 ms post-stimulus and a bin width of 40 μs.

2.4-Discussion

2.4.1 Healthy fiber response thresholds and latencies differ between stimulus waveforms

To better understand how CI stimulation is encoded within the primary neurons of the auditory pathway, and the impact of pathology upon this encoding, several groups have performed single unit recordings from SGN axons as they enter the brain stem of cats. Shepherd and Javel's 1999 study found the polarity of stimuli could lead to variations in threshold and latency of neural responses indicating these different phases may activate neurons in different locations (Shepherd and Javel, 1999). Similarly, Miller et al.'s finding of bimodal latency of responses to monophasic CI stimulation suggests the presence of multiple potential sites of activation even within a single fiber and in response to a single stimulus polarity (Miller et al., 1999). Such variations in site of activation have the potential to profoundly alter encoding of timing cues, however, the biophysical factors mediating which initiation site a stimulation paradigm activates are not well understood. The present work suggests these stimulus waveform-dependent dynamics may be explained by the antisymmetric electrotonic effects that anodic and cathodic currents have upon membranes and the subsequent variation in sites of action potential initiation. This effect interacts with cochlea and fiber structure to produce the complex interactions observed in electrophysiologic recordings.

2.4.2 Simulations provide insight into complexity observed in animal models of hearing loss

These simulation results provide a novel perspective from which to consider conflicting electrophysiological findings observed in animal models following deafening. Studies of single unit responses to intracochlear CF biphasic electrical stimulation have observed both increases and decreases in threshold with duration of deafness (Shepherd et al., 2004; Sly et al., 2007). In contrast, our simulations show consistent increases in response threshold for single fibers as demyelination becomes more severe though this effect is modest except in the most extreme cases. A number of scenarios might reconcile these disparate findings. For instance, demyelination may generally promote higher thresholds in individual fibers but asymmetric degeneration, impacting primarily smaller high threshold fibers, complicates this trend. In at least some hearing loss settings such asymmetries have been observed and are thought to interfere with population level coding of stimulus intensity (Furman et al., 2013; Kujawa and Liberman, 2009). Another possibility is that changes to the electrical structure of the cochlea following hair cell loss might alter tissue impedance, ultimately lowering neural thresholds despite loss of neural insulation. Finally, while both studies explored the impact of duration of deafness on single unit responses to stimulation, they used different animal models (rats and guinea pigs in the 2004 and 2007 studies, respectively). It's likely that there exist significant differences in the progression of cochlear pathology in these different species.

Timing properties of SGNs in these studies exhibit similarly complex relations to duration of deafness. Latency of single unit responses showed no significant change with progressive deafness in the 2004 study, however, the 2007 one found a progressive decrease with duration of deafness, consistent with our findings (Shepherd et al., 2004; Sly et al., 2007). Interpretation of this data is challenging both due to variations in the details of deafening and because the experimental approach precludes the possibility of determining where a recorded unit lies in the cochlea relative to the electrode. The latter effect may lead to different patterns of SGN activation than occur in human implantees and cause results to be sensitive to the details of single unit selection. Our findings suggest that depending on the specific progression of demyelination within a fiber, both increases and decreases in latency at threshold may be possible. As such, depending on the precise details of the mechanism and duration of deafness, different distributions of demyelination severity might exist within animals leading to large between fiber variability.

Our results suggest opportunities for developing a better understanding of the relation between structural and electrophysiological dynamics following deafening in animal models. We observed dramatic changes in the relative sensitivity of fibers to different pulse polarities with severe demyelination. We believe that comparing input-output functions of responses to AF and CF biphasic stimuli for animals with varying durations of deafness would provide insight into how myelination was changing. We predict that duration of deafness will correlate with the average ratio of CF to AF thresholds due to the peripheral processes of fibers becoming more difficult to depolarize. Additionally, when this ratio nears 1, fibers will be particularly likely to possess multiple action potential initiation foci resulting in a greater frequency of bimodal latency distributions. The incidence of such bimodality would then be expected to decrease as demyelination, and/or peripheral process degeneration, progressed still further to involve nearly all fibers.

In addition to altering single fiber properties, pathological perturbations of SGNs are expected to alter population signal encoding. Based on our preliminary single fiber results, we predict demyelination will generally not alter populations' sensitivities substantially but that heterogeneity in the amount of demyelination across a population may lead to profound dispersion in spike times and loss of temporal fine structure information. While this an area of great interest, implementing heterogenous demyelination within a population will require careful grounding in histopathological data to achieve reasonable representations of pathology across populations.

2.4.3 Only extreme demyelination shifted thresholds sufficiently to promote current spread and pathological recruitment

The simulations in the present study suggest that thinning of the myelin sheath surrounding SGNs may alter how they are excited by extracellular stimulation. Decreased myelin thickness that affects more than just the most peripheral nodes, lead to increased thresholds particularly in scenarios where fibers are depolarized by cathodic polarity pulses. The magnitude of this change, however, was exponentially related to the diameter of remaining myelin leading to relatively modest changes of little practical significance until demyelination becomes more severe than is consistent with the histopathological literature. In the extreme case of complete loss of myelin, we observed the absence of action potentials due to failed conduction of responses to monophasic cathodic stimuli. Response thresholds to anodic phases exhibited complete resistance to peripheral demyelination and only exhibited substantial change with broadly distributed near complete loss of myelin. These threshold changes suggest, in the extreme, that demyelination might require elevated current amplitudes generating increased spread of excitation within the cochlea and greater channel interaction; however, fiber thresholds are overall remarkably robust to this myelination perturbation. Additionally, demyelination generally resulted in a decrease in the dynamic range of fibers, suggesting they begin behaving more deterministically. Such a reduction in dynamic range would interfere with the detection of loudness cues and could promote pathological recruitment. Overall these effects generally occurred only at remarkably extreme amounts of demyelination consistent with the clinical observation that most CI recipients receive at least some benefit in speech recognition in quiet from their device.

2.4.4 Demyelination induced timing changes may alter binaural timing cues

Efforts to deliver fine temporal information potentially critical to temporal pitch coding and certainly to interaural time differences rely on precise neural responses to individual pulses from a cochlear implant. As such, pathology-induced latency changes in responses to single pulses are expected to set limits on the quality of such information that can be delivered. Since even with relatively modest perturbations of myelin, timing of stimulus-induced action potentials changed in ways that could have dramatic behavioral impact. Although phonetically relevant temporal information in speech is unlikely to occur in a window shorter than ~ 20 ms (Rosen, 1992; Saberi and Perrott, 1999), the binaural system utilizes interaural differences on the order of tens of microseconds (Bernstein and Trahiotis, 2015; Zwislocki and Feldman, 1956). Our demyelination simulations predict latency changes of an order relevant to the latter but not the former.

With demyelination involving at least the most peripheral 10 nodes, latency of action potentials initiated by cathodic polarity pulses increased with both the extent of fiber affected and severity of myelin thinning due to reduced conduction velocity along demyelinated axons. For instance, a 77% reduction in myelin involving the first half of a fiber resulted in a mean latency delay of 175 μs for responses to monophasic cathodic pulses which, if paired with healthy fibers contralaterally, would introduce an interaural timing difference artifact, leading to an error on the order of 20-30° in perceived sound source location (Nordlund, 1962). More severe demyelination introduces even larger errors; severe demyelination (87%) impacting at least 16 nodes of a fiber stimulated by monophasic cathodic stimuli yields delays of greater than 300 μs, nearly half the maximum possible ITD for humans. In contrast, anodic-phase induced responses exhibited almost no change in latency unless severe demyelination was applied to nearly the entire fiber.

The different relationships between fiber response properties and myelination state for opposite polarity pulses has a dramatic implication for biphasic pulses. Both CF and AF biphasic stimuli produce responses with thresholds and latencies like cathodic monophasic stimuli in normal fibers, those with demyelination affecting fewer than the first 10 nodes, and those with broad demyelination but retaining at least 15% of their myelin. In fibers with demyelination of greater severity and broader distribution, response properties become more like those to anodic monophasic stimuli. This behavior is due to abrupt changes in site of action potential initiation when demyelination impacts the region of fiber normally depolarized by cathodic polarity pulses but spares the central portion of fibers activated by anodic ones. This shift in relative phase sensitivity profoundly alters the timing of responses.

Normal hearing listeners have been shown to make lateralization judgements using ITDs extremely rapidly and to weight the onset ITD of pulse train stimuli particularly strongly (Brown and

Stecker, 2010; Freyman, 1997; Klein-Hennig et al., 2011). Providing implantees access to these cues will, therefore, require faithful encoding of timing of single pulses. To illustrate the potential magnitude of the latency variability observed in our simulations on fine temporal structure coding, expected onset ITDs between cochlear nucleus arrival times of coincidentally delivered AF biphasic pulses are plotted for different degrees of myelination asymmetry in Fig 10. AF biphasic pulses were selected since modern implants typically use biphasic pulses and latency effects were more pronounced with AF pulses (though they were still present and substantial with CF pulses). While fibers with 87% demyelination impacting the first 16 internodes stimulated by AF biphasic pulses exhibit a mean latency that lags that of normal fibers by 350 μs, similarly affected fibers with slightly greater, 92%, demyelination respond with mean latency leading normal fibers by 470 μs; a net difference of 820 μs, significantly greater than the maximal physiological ITD (compare Fig 10A,B,&C). If a fiber population contained fibers with both such demyelination states a single biphasic stimulus would produce population activity with a large degree of temporal distortion.

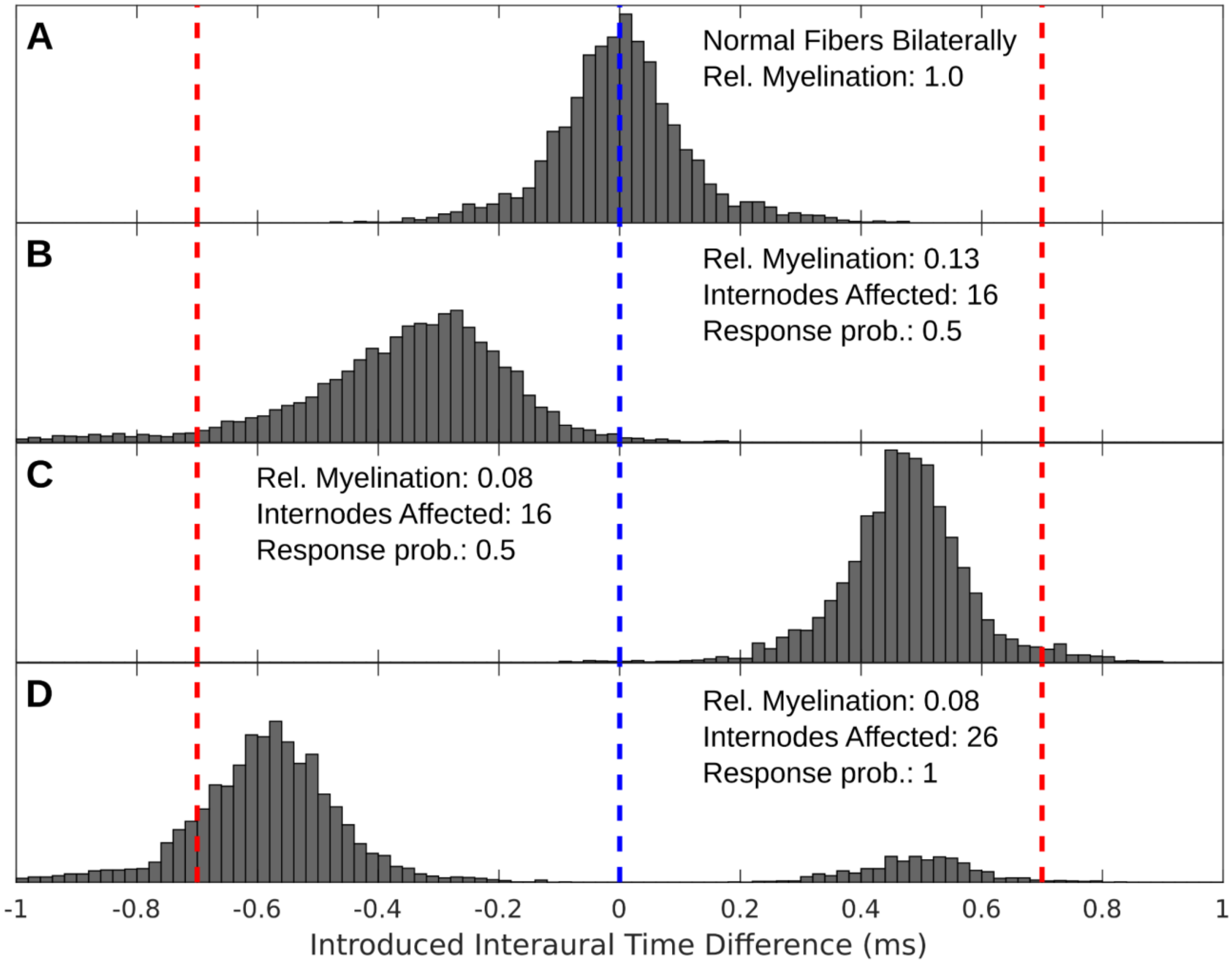
A
Normal Fibers Bilaterally
Rel. Myelination: 1.0
B
Rel. Myelination: 0.13
Internodes Affected: 16
Response prob.: 0.5
C
Rel. Myelination: 0.08
Internodes Affected: 16
Response prob.: 0.5
D
Rel. Myelination: 0.08
Internodes Affected: 26
Response prob.: 1
-1
-0.8
-0.6
-0.4
-0.2
0
0.2
0.4
0.6
0.8
1
Introduced Interaural Time Difference (ms)

Figure 2.10- Asymmetric demyelination introduces interaural timing difference artifacts**.** Histograms of pathology induced interaural time difference artifacts were constructed by repeatedly subtracting latencies sampled from the 'right' fiber's distribution from that of the 'left' to anode-first biphasic pulses presented concurrently to both sides. Here the induced interaural timing difference is presented on the abscissa and frequency of these outcomes is plotted on the ordinate. This procedure presumes a situation where the electrodes stimulating both sides are synchronized and that they have independent, but ideal, mappings. For each panel, the left fiber was kept normally myelinated and the myelination state of the 'right' was varied: **(A)** normal fiber, **(B)** fiber with first 16 internodes 87% demyelinated, **(C)** fiber with first 16 internodes 92% demyelinated, and **(D)** fiber with 26 internodes 92% demyelinated. For (A-C), stimulating pulses were delivered at threshold for both sides while for (D) the stimuli used produced a response probability of 0.98 on their respective side. For each fiber pairing, 10,000 random samplings were taken from the distributions of response latencies.

In addition to these dramatic between fiber response latency differences, we observed elevated response jitter and bimodal latency distributions, depicted in Figure 9C&D, for some fibers, resulting from stochastic activation of both peripheral and central sites. While only captured for fibers with specific parameter pairs in this work, we intuit there must be some stimulus intensity for each fiber that leads to comparable sensitivity to both phases of biphasic pulses. Figure 10D illustrates how a fiber with bimodal latency distributions could stochastically provide opposing ITD cues. In this scenario, it would be impossible for downstream elements of the auditory pathway to decode the spike timing of single SGNs to ascertain the true relative phases of binaural acoustic stimuli, even if there exists plasticity in the circuit. These elevations in between and within fiber jitter may lead to interaural decorrelation, which is the measurement underlying the framework of a many of theories of binaural hearing (Bernstein and Trahiotis, 2017).

While the observed timing deficiencies are large enough to affect ITDs, they are not likely to affect speech discrimination in quiet since the relevant timing properties occur on a scale at least an order of magnitude larger. However, since normal spatial hearing is dominated by perception of fine-structure ITD cues (Wightman and Kistler, 1992) and perceived spatial separation of speech and noise facilitate improved speech intelligibility (Freyman et al., 1999; Hawley et al., 2004), poor transmission of ITD cues will have serious, detrimental effects to hearing speech in everyday (i.e. noisy) environments. As poor speech perception in noise is the chief complaint of most people with hearing loss, there is a potentially important connection to be made between the physiological impact of demyelination and behavioral performance in certain tasks.

2.4.5 Human psychophysical predictions

Studies comparing thresholds between CF and AF biphasic stimuli within humans have revealed no statistically significant average difference between these two pulse types (Macherey et al., 2006). However, recent work has found that individual patients tend to exhibit a clear sensitivity difference, that can vary between electrode, but that these variations tend to average out between patients (Macherey et al., 2017). Moreover, this group found that all patients exhibited lower maximum comfortable levels with anodic polarity dominated waveforms. The present study suggests that the variability in relative sensitivity between these different pulses may be partially due to differences in the myelination state of SGNs near the electrode in question. As such, we predict that in a large cohort there should exist a correlation between average CA/AC threshold ratio and duration of deafness. Moreover, our simulations predict such changes in relative sensitivity should coincide with alterations in the fidelity of response timing. We anticipate that when the CA/AC threshold ratio is greater than 1.0, detection of ITDs should be superior with AF pulses. Additionally, when thresholds to CF pulses are lower ITD detection is predicted to be better at lower stimulus strengths, below the onset of bimodal latency distributions.

2.4.6 Neuron structure and channel distribution simplifications may mask additional complexity

In the present simulations, the stimulating electrode was placed over node 10 to avoid terminal effects in the numerical solutions. Rattay and colleagues observed initiation sites substantially more peripheral to those found in the present study but this previous work positioned electrodes nearest the peripheral-most nodes (Rattay et al., 2001b). The more central positioning of the electrode in the present study is likely why the more lateral excitation site is substantially more central than that observed by Rattay et al.

The presented model does not explicitly treat the cell body as a unique structure, distinguish between peripheral and central axons segments, or account for heterogeneity in the distribution of ion channels between nodal segments. Other simulations have incorporated such structural asymmetries and found they may alter model behavior, however, due to a paucity of electrophysiological, structural, and expression studies involving the cell body such simulations introduce additional poorly constrained parameters (Frijns et al., 2000; Rattay et al., 2001a). Additionally, while excitatory channels are present at each node of Ranvier to support saltatory conduction, particularly dense Nav1.6 expression has been observed in the nodes immediately adjacent to the cell body (heminode and initial segment) and in fiber terminals adjacent to hair cells (Hossain et al., 2005); this excitatory channel distribution may also critically contribute to the site of cochlear implant action potential generation. Exploring the impact of these other structural elements is critical but simulating them effectively will require more constraining morphometric and histopathological data.

The model used in the present study was constructed and tuned such that it produced responses with similar characteristics to feline ANFs in the absence of explicit modeling of a soma or asymmetries in peripheral and central axons (Imennov and Rubinstein, 2009). To a rough approximation, the contributions of these structural elements are, therefore, implicitly incorporated into the tuned parameters. The simulated latency difference between peripherally and centrally initiated events by AF pulses in normally myelinated fibers are of the same order of those recorded by Miller et al. (compare Fig 3C & D) suggesting this spatial variability in excitation is preserved despite the use of implicit soma incorporation and axonal homogeneity (Miller et al., 1999). Nevertheless, the variability in initiation site observed should be viewed as related to electrical distance, impedance, rather than true distance. The presence of a cell body, particularly if its myelination state is subject to change, would introduce a large capacitive load and create larger potential gradients with axial distance than predicted in the current study. While the peripheral and central initiation sites are relatively farther apart in our study than in studies leveraging cell bodies, incorporating the high capacitive load of a discrete soma would reduce this distance and likely bring our findings in line with previous studies. Such changes in relative distance between initiation sites would be consistent with Finley, Wilson, and White's comparison of models with and without soma (Finley et al., 1990).

We opted to constrain our parameter space to demyelination within a simple core-conductor model to simplify interpretation and limit speculation regarding model parameters. Importantly, we anticipate the substantial latency difference due to the difference in the conduction delay between initiation sites would be qualitatively preserved in this setting since while the distance may be shorter the cell body would introduce a high capacitive load, particularly if its myelination state changes.

2.4.7 Myelin-loss-induced changes in adaptation and/or refractoriness may alter responses to pulse trains

While the temporal fidelity of responses to individual pulses is critical for conveying fine temporal structure, modern cochlear implants use relatively high pulse rates to optimize speech reception. The response properties of single neurons, and populations, with different myelination states to faithfully to paired pulses, pulse trains, and more speech-relevant stimuli are, therefore, of great interest. The present model does not exhibit physiological relevant adaptation so responses to such high-rate stimuli will need to be interpreted with care. The addition of non-homogenously distributed additional cation channels to a cell-body-containing model has also been shown to produce a source of adaptation that could be incorporated into a segmented model in the future (Boulet and Bruce, 2017a; Negm and Bruce, 2014).

2.4.8 Other pathological changes may further alter neural responses

This work used a highly simplified model of neural stimulation by extracellular currents and modified only two anatomical parameters: myelin thickness and extent of demyelination. Even considering only these two parameters, more complex relations than those presented here could be used to introduce loss of myelin. We believe the results of the present study are likely robust to such details since the relationships between fiber responses and myelin thickness were relatively insensitive to the exact number of internodes affected. The transitions in site of action potential observed were dramatic so small amounts of within internode variability in the demyelination are unlikely to impact them significantly.

Elements other than internode myelin diameter have been observed to change following deafening, including: increases in node length and diameter, paranode diameter, and juxtaparanode length; and decreases in paranode length and juxtaparanode (Tagoe et al., 2014). Whether changes in internode length occur as well remains unexplored. Moreover, whether such changes occur independently or in concert, due to some common dis-regulation remains unknown. Focal axonal swelling incorporated into auditory nerve fiber models was previously observed to alter conduction velocity even in the absence of internodal myelination loss suggesting the possibility of complex interplay between these structural changes (Kolaric et al., 2013). Work in deafened Guinea Pigs has also observed sub myelin vacuolization due to retraction of neural axoplasm in the absence of significant myelin loss on a shorter timescale than the myelin thinning observed in cats and humans, suggesting at least some species-specific pathological progression (Wise et al., 2017).In addition to changes in the geometry of SGNs, it is possible that their electrical properties might be altered by compensatory or pathological changes in the expression or distribution of ion channels. Such changes have been observed following monocular deprivation in the visual system (Craner et al., 2003). In the setting of the cochlea such changes could dramatically alter action potential initiation and/or propagation.

In addition to these neuron simplifications, we employed a simplified electrical model of the cochlea. The details of the electrical structure of the cochlea will certainly impact where action potentials are initiated. Others have simulated the effects of predicted cochlear electrical structure and found it can dramatically shape where modeled nerves are most easily excited (Briaire and Frijns, 2006, 2000a; Rattay et al., 2001a; van Gendt et al., 2016). Implementing parameter exploration, as performed here, within a multi-compartment model of the cochlea might further improve predictions about where CIs might depolarize SGNs in different functional states. Unfortunately, little is known about these electrical properties to constrain such complex cochlear models and assumptions must be made at some level, thus we opted for a simple model for clarity. Exploring how pathological changes in the electrical properties of the cochlea, such as altered impedance due to tissue fibrosis, impact neural response timing is another valuable avenue of research.

2.5-Conclusions

Collectively, these observations provide some insight into how a dysfunctional periphery may differentially impact encoding of stimulus elements critical to different kinds of tasks. Fibers maintained the ability to produce at least some responses to charge-balanced pulses, like those used in modern implants, even with profound demyelination. Only in the event of demyelination more severe than previously observed in cellular imaging studies would we expect sufficiently elevated thresholds to lead to increased spread of excitation and greater channel interaction. Moreover, while we did not look at longer-term adaptation or refractory effects, the latencies we observed are likely too small to dramatically alter recognition of critical elements of speech in quiet (with relevant features generally lasting >20 ms). In contrast, fine temporal coding, including the phase locking needed to detect ITDs, was dramatically altered even by relatively modest perturbations of myelin. Extrapolating these effects out to populations of neurons, we anticipate that non-uniform changes in ultrastructure will lead to dispersion of the population timing signals which would further degrade implantees ability to utilize fine temporal cues but generally preserve thresholds and modulation detection. This predicted sensitivity parallels clinical observations where most implant recipients experience at least some, and usually substantial, improvement in their ability to recognize speech in quiet but few can perform well when tasks involve detecting speech in noise or ITD-based sound localization.

2.6 Acknowledgments

We would like to thank Drs. Matthew Winn for his intellectual guidance and writing assistance and David Perkel for writing assistance and proofing. This chapter was accomplished with the financial support of an educational gift from Advanced Bionics, the Computational Neuroscience Training Program (NIH-2T90DA032436-06), and the Auditory Neuroscience Training Program (NIH 2T32 DC005361-16) at the University of Washington. It was facilitated though the use of advanced computational, storage, and networking infrastructure provided by the Hyak supercomputer system and funded by the STF at the University of Washington.

Chapter 3- Simulated auditory fiber heterogeneity desynchronizes population responses to electrical stimulation limiting inter-aural timing difference representation

In preparation for submission to the Journal of the Acoustical Society of America.

3.1 Introduction

In individuals with severe to profound sensorineural hearing loss that do not adequately benefit from a hearing aid, cochlear implants (CIs) can provide remarkable restoration of speech reception abilities, particularly in quiet environments.(Poissant et al., 2014) Despite the fact that implants provide dramatic improvements in speech reception for the vast majority of implantees' they generally fail to provide the fine temporal information necessary to properly localize sounds and segregate sources in noisy environments.(Litovsky et al., 2012) In individuals with intact acoustic hearing, interaural timing differences are one of the key cues for localizing sound sources in the azimuthal plane. Such listeners can generally detect ITDs on the order of 10-50 µs, making this binaural circuit one of the most temporally precise in the nervous system.(Bernstein, 2001) Multiple engineering barriers limit implantees' access to these cues. Commercial cochlear implant signal processing strategies typically extract the temporal envelope of input audio and modulate a pulse train carrier with it, consequently discarding much of the fine temporal information in the signal. Additionally, bilateral implants are typically not synchronized which would prevent these cues from being accessible even were they preserved. Unsurprisingly, implantees using these clinical processing strategies do not have good access to these ITD cues.(Francart et al., 2014)

Disappointingly, even in controlled research settings where precisely timed, low rate pulse trains are delivered to bilateral implantees, their just-noticeable-differences are still dramatically elevated over those in acoustic hearing individuals.(Kan and Litovsky, 2014; Litovsky et al., 2012) In contrast, at the single unit level, electrically stimulated neurons exhibit significantly less temporal jitter in their responses compared to those that receive synaptic input from hair cells.(Miller et al., 2003, 2001, 1999) Additionally, at the level of the inferior colliculus, degraded temporal acuity in response to electrical stimulation, particularly in long-term deaf animals, has been observed.(Chung et al., 2016; Vollmer et al., 2005) These results present conflicting narratives where individual primary neurons appear to be supra-naturally synchronized to electrical stimuli, but behavioral evidence and midbrain recordings suggest degradation of fine temporal information. In this study, we present simulations of auditory nerve fiber population responses to low-rate electrical pulse trains that suggest variance in recruitment and response latency at the population level may resolve this disparity.

Several human and animal studies exploring the microarchitectural outcomes of hearing loss have identified pathological changes in SGNs that may contribute to spike latency variance at both the single neuron and population levels. Post-mortem human temporal bone microscopy has found significant loss of SGNs in adult individuals that was greater when hair cells were absent, suggesting progressive SGN loss does occur in humans, particularly those with hearing loss (Zimmermann et al., 1995). Moreover, a study correlating threshold measures of CI recipients in life with post-mortem SGN counts observed a significant interaural correlation between behavioral and histological outcomes (Incesulu and Nadol, 1998). Rigorous time course studies in rats, guinea pigs, and cats demonstrate that they undergo similar levels of degeneration, albeit with species dependent time courses (Kroon et al., 2017; Shepherd et al., 2004; Sly et al., 2007). Beyond complete soma loss, studies have demonstrated both acute and progressive SGN ultrastructural changes, notably axon demyelination, even in the absence of soma death, and corresponding altered physiology following sensorineural deafening. Loss of myelination within the peripheral process precedes that of the central process, and ultimately degeneration of these processes and cell death in both humans and cats (Hardie and Shepherd, 1999; Leake and Hradek, 1988; Shepherd and Javel, 1999). More recently, Tagoe et al. (2014) noted a reduction in myelin lamellae number and a downward shift in the distribution of myelin thickness following deafening via acoustic over-exposure in rats (Tagoe et al., 2014). Collectively, these studies indicate the structural integrity of SGNs, particularly myelin insulation of internodal segments, is damaged following deafening; and the time course, while not fully characterized, suggests a progressive process.

Computational models of the CI electrode-neuron interface provide the opportunity to explore mechanistic links between the anatomical and electrophysiological neural changes observed in animal models of SHL and human fine temporal detection performance. Resnick et al., 2018 outlines an approach for introducing either peripheral or central demyelination into a stochastic, biophysical model of extracellular electrical stimulation of auditory nerve fibers.(Resnick et al., 2018) This model was selected for the this and the present study because it enables exploration of the interactions between the spatial spread of current and inhomogeneities in the myelination of axons while attempting to limit the number of tunable parameters present. By expanding this approach to stimulate populations of neurons with physiologically plausible levels of diameter and myelin heterogeneity, we sought to explore population-level encoding of simple temporal cues in electrical hearing. Here we present simulations suggesting that inter-fiber heterogeneity may lead to temporal dispersion in population-level responses that set important limits on fine temporal encoding, even within relatively intact SGNs, and that significant demyelination further degrades this ability.

3.2. Methods

3.2.1 Population model of single electrode SGN fiber stimulation

The population models presented in this study consist of collections of 200 Type 1 SGN fibers each represented as a single segmented cable, as previously described.(Imennov and Rubinstein, 2009; Mino et al., 2004; O'Brien and Rubinstein, 2016; Resnick et al., 2018) Within individual fibers, the membrane potential within each segment during stimulation by an extracellular electrode is described by a partial differential equation (Eq. 1) relating axial current to capacitive, leak, applied, and ionic currents:

$$\frac{-\hbar^2}{R_a(x)}\frac{d^2V_m(x,t)}{dx^2} = C_m(x)\frac{dV_m(x,t)}{dt} - \frac{V_m(x,t)}{R_m(x)} + \frac{\hbar^2}{R_a(x)}\frac{d^2V_{ext}(x,t)}{dx^2} + I_{ion}(x,t) \qquad (1)$$

Behavior of each of these currents is dictated by biophysical parameters, originally derived from anatomical and physiological data from, principally feline, auditory nerves and were then allowed to vary within 10% of empirical values until simulated electrophysiological properties fell within 10% of values recorded from cats. The present study uses identical parameters to those used in Resnick et al., 2018 except for the specific fiber population manipulations described below. Each fiber consists of nodes, with intervening internodes, with segment lengths that scale with fiber caliber but a constant total length approximately equal to that between the auditory periphery and cochlear nucleus in cats. Internodes are each divided into 9 segments possessing purely passive electrical properties while nodes of Ranvier are represented as single segments possessing both passive elements and stochastic, voltage dependent ionic currents.

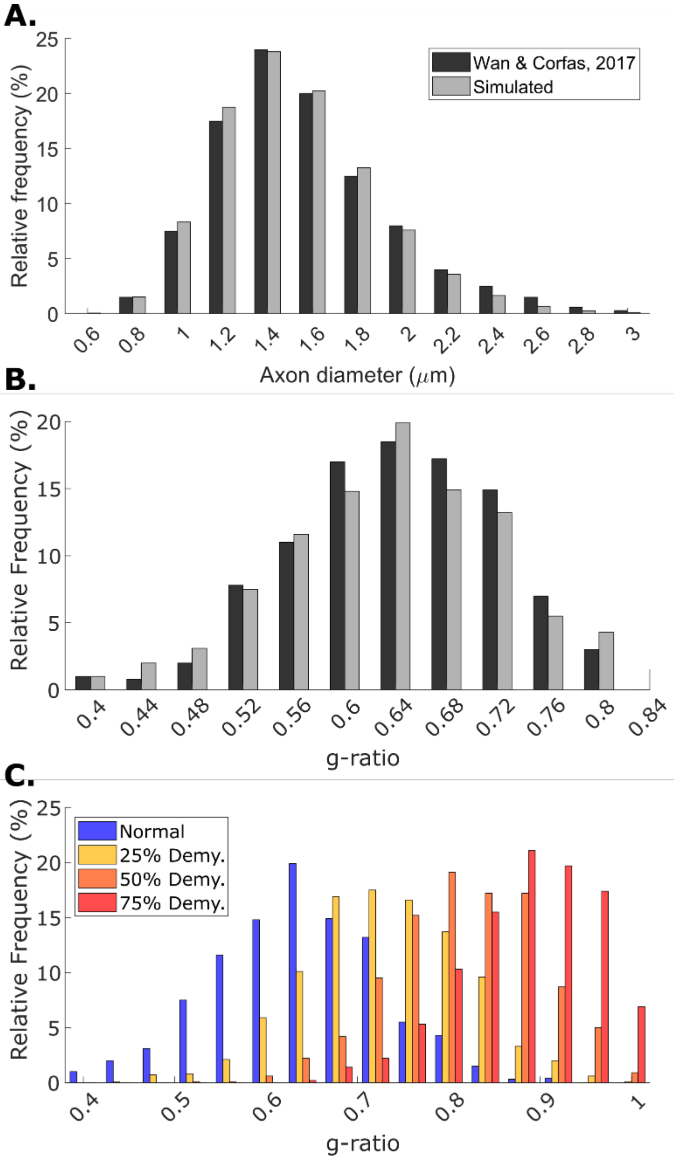

Figure 3.1- Normal and pathological simulated fiber heterogeneity.

(A) Simulated fiber (gray) and experimental (black) peripheral axon diameter distributions. (B) Simulated fiber (gray) and experimental (black) peripheral axon g-ratio distributions. Empirical measurements from normal-hearing mice measured using electron microscopy reported in Wan and Corfas, 2017 (reprinted with permission). (C) g-ratio distributions for four different levels of fiber demyelination.

Internode fiber diameters for the populations were randomly drawn from a log-normal distribution (depicted in **Fig 3.1A**.) with mean of 1.477 µm and standard deviation 0.22 µm, modeled after the distribution of peripheral nerve diameter measurements from acutely deafened mice measured via electron microscopy by Wan and Corfas.(Wan and Corfas, 2017) This empirically derived distribution aligns closely with the distribution used by Imennov and Rubinstein which reproduced the shape of the feline SGN threshold distribution reported by Miller et al..(Imennov and Rubinstein, 2009; Miller et al., 1999)

The length of internodal segments is equal to the product of their diameter and a constant length to axolemma diameter ratio of 92 : 1.(Arnesan and Osen, 1978; M. Charles Liberman and Oliver, 1984) Membrane and axonal resistances of all segments scale with their surface and cross-sectional areas, respectively, and do not vary with myelination state. While nodal segment membrane capacitance was fixed as a product of the membrane specific capacitance and the nodal area, internodal segment capacitance was manipulated to myelin loss as described further below.

The behavior of the stochastic, voltage-dependent ion channels within nodal segments was modeled using a Markov jump process.(Gillespie, 1977; Mino et al., 2004; Mino and Grill, 2002) Total ionic current was defined as the sum of sodium, slow potassium, and fast potassium currents. This procedure enabled computationally efficient simulation of channel dynamics within each segment while maintaining an accurate representation of their stochastic behavior.(White et al., 2000) Nodal segment diameter was defined as equal to the internodal diameter multiplied by the constriction factor 0.5. The number of each channel type was determined by multiplying the nodal surface area times empirically derived ion channel densities, thus the number of channels scale with the square of the fiber diameter.

Simultaneous solution of numerical approximations of the system of partial differential equations described by Eq. 1, with the relevant segment geometrical properties, ionic currents, and applied field induced currents (described in section 2-3), by an implicit Crank-Nicholson scheme yields the potential within each segment of the model fibers for each time step of the simulation.(Mino et al., 2004) A time step of 1 μs was used for all simulations. Simulations were performed using custom-built C code with a MATLAB (MathWorks) wrapper for managing input parameters and analyzing output data.

3.2.2 Introduction of population myelination heterogeneity

Previously, we implemented a modified core-conductor model for simulating fiber myelin loss (Resnick et al., 2018). In this approach, internodal plasma membrane resistance and capacitance were modeled as being in series with the myelin sheath's, creating a core-dual conductor model. Since the specific resistance of lipid bilayer without ion channels embedded in it is of a similar order to that of myelinated axon (10^6-10^8 ohm*cm^2 and 4.45*10^8 ohm*cm^2, respectively), resistance was fixed independent of myelin width.(Imennov and Rubinstein, 2009; Montal and Mueller, 1972) Assuming the plasma membrane dielectric constant remains consistent between nodal and internodal segments, the plasma membrane capacitance of the internode can be estimated using the nodal value divided by the constriction factor. The total internodal capacitance can then be calculated by adding the plasma membrane and myelin contributions in series:

$$\frac{1}{C_{internode}} = \frac{1}{C_{my}} + \frac{1}{C_{m,internode}} = \frac{\log(D/d)}{\log(1/0.6)C_{my,normal}} + \frac{c_{constric}}{C_{m,node}} \qquad (2)$$

We extended this model to reflect normal neural myelination heterogeneity by generating a g-ratio (axolemma diameter : myelin sheath diameter) distribution matched to that measured using electron microscopy in normal-hearing mice by Wan and Corfas, 2017.(Wan and Corfas, 2017)

Our simulated normal distribution with mean value of 0.64 and standard deviation of 0.24, see **Fig 3.1B**. Individual fibers g-ratios were selected from this distribution and used in conjunction with the pseudo-randomly generated internode axolemma diameter according to Eq. 2.

To simulate varying severities and extents of population demyelination the mean of the normal distribution was shifted by modifying the healthy means by a demyelination severity factor (D_{sev}) between 0 and 1 via Eq. 3:

$$g - ratio_{demy} = g - ratio_{health} + (1 - g - ratio_{health}) * D_{sev} \qquad (3)$$

This approach enables simulation of populations with arbitrary mean degrees of demyelination severity while maintaining the normal inter-fiber variance in g-ratio. Additionally, the extent of each fiber impacted was independently modified by applying the demyelination approach to either the peripheral half of or entire fiber. In these experiments, we elected to constrain our simulations to either peripheral, in which only the peripheral half of each fiber is affected, or complete demyelination, in which the entire fiber is affected.

3.2.3 Stimulus selection and response analysis

Simulated SGN axon populations were stimulated by an extracellular disk electrode as derived previously by Rubinstein and used in previous versions of this model.(Imennov and Rubinstein, 2009; Mino et al., 2004; O'Brien et al., 2016; Resnick et al., 2018; Rubinstein, 1988) Briefly, by assuming that injected current propagates through an isoresistive medium, the applied potential difference between adjacent segments can be expressed as a function of the injected current and the segment-electrode distance. The field potentials along each fiber can then be calculated for each time step during stimulation for a selected current waveform. All fibers were treated as co-located 3 mm from the electrode since nerve fibers within the spiral ganglion are often bundled.

Populations were presented with either single pulse or 100 pulse-per-second cathode-first biphasic stimulation with 25 μs phase duration and 10 μs inter-phase gap, a common stimulus waveform for clinical CIs. Following stimulus presentation, simulations were continued for 4 ms to enable monitoring of fiber-potential evolution. For the initial experiments, single pulses were used while 100 ms duration, 100 pulse-per-second stimuli were used for the inter-aural timing difference just noticeable difference experiments.

3.2.4 Simulating interaural timing difference (ITD) detection

To explore potential ramifications of demyelination on fine temporal cue encoding, we simulated the ITD distributions produced by delivery of biphasic pulses to different fibers, which in this case represent the populations of neurons nearest corresponding electrodes in ‘left’ and ‘right’ simulated cochlea. In the present experiments, we constrained our analysis to symmetric pathologies where the myelination state of left and right simulated fiber populations were modified concurrently. Our aim was to explore ideal ITD JND performance based on peripheral firing with minimal assumptions regarding central processing.

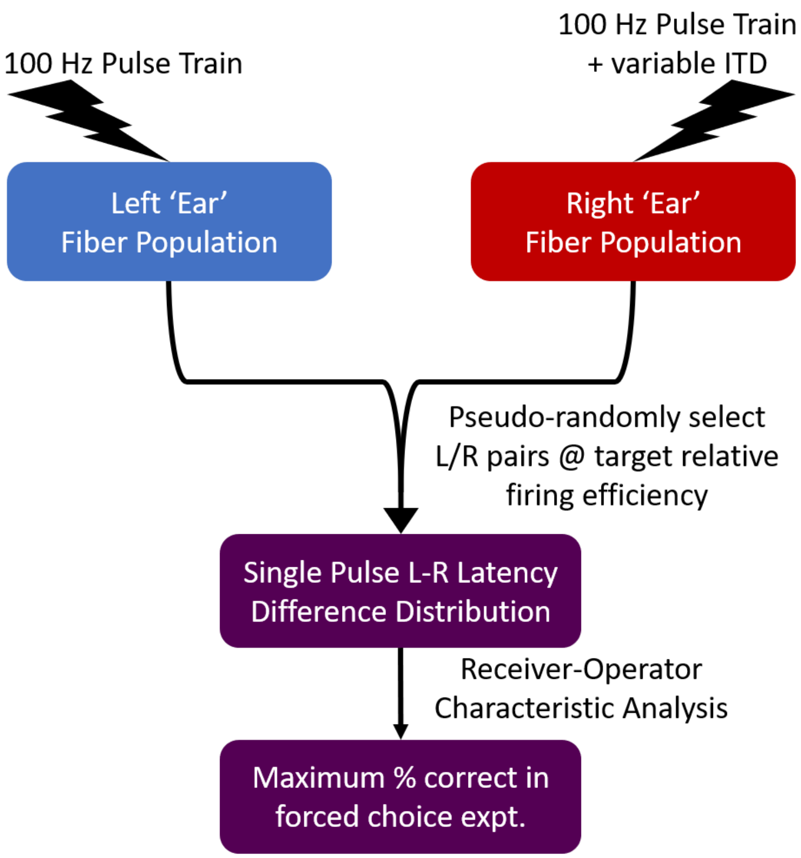

Figure 3.2- Simulated inter-aural timing difference detection task.

Diagram of procedure used for the simulated ITD detection task. Pulse trains (100 Hz) were presented to simulated neural populations with variable ITDs and intensities. Neural population varied in demyelination severity and the extent of fiber affected. Fibers were selected from these populations using one of three different pseudo-random selection strategies: fully-random, active-only, or low-threshold. These fibers were then paired based on their diameters to produce mean L-R latency difference distributions. Receiver-operator characteristic analysis was performed on the latency-difference distributions producing estimates of percent correct in a forced choice task.

Figure 3.2 is a diagrammatic illustration of the simulation strategy. Two populations, representing bilateral implantation, were stimulated with, anode-first biphasic pulse trains, at 100 pulses-per-second, delivered with precisely defined phase differences. At this low pulse rate, period-to-period peri-stimulus time histogram distributions remained consistent over the stimulus duration so spike latencies relative to stimulus onset were pooled for each neuron for all pulses. Fiber pairs between the two simulated populations were selected based on diameter rank order and, for each pair, left-right latency differences were calculated. For comparison between populations, responses for analysis were matched based on relative firing efficiency (rFE), the proportion of fibers responding relative to the maximum response proportion for that population.

To enable exploration of the ramifications of different potential central-processing algorithms, we considered the outcome of performing this analysis on only subsets of the fiber pairs. These subsets were selected either entirely randomly (‘random’), from only fibers responding to at least one pulse at the level selected (‘active’) or selected from active fibers with jitter less than the mean of the population (‘lowest-jitter’).

Population latency difference responses were constructed by drawing single difference values from these single fiber-pair distributions and then averaged to calculate a mean population latency difference response. The discriminability of these mean simulated inter-aural timing differences from the 0-phase difference condition were assessed using a receiver-operating characteristic (ROC) analysis strategy. Percent correct on a 2-interval discrimination task between the stimuli with ITD and the control condition were estimated from the area under these ROC curves. The number of pairs pooled for each mean and the number of repetitions through the entire simulation pipeline were varied experimentally to explore the robustness of the strategy to these parameters.

3.3 Results

3.3.1 Demyelination reduces recruitment function slope and asymptote

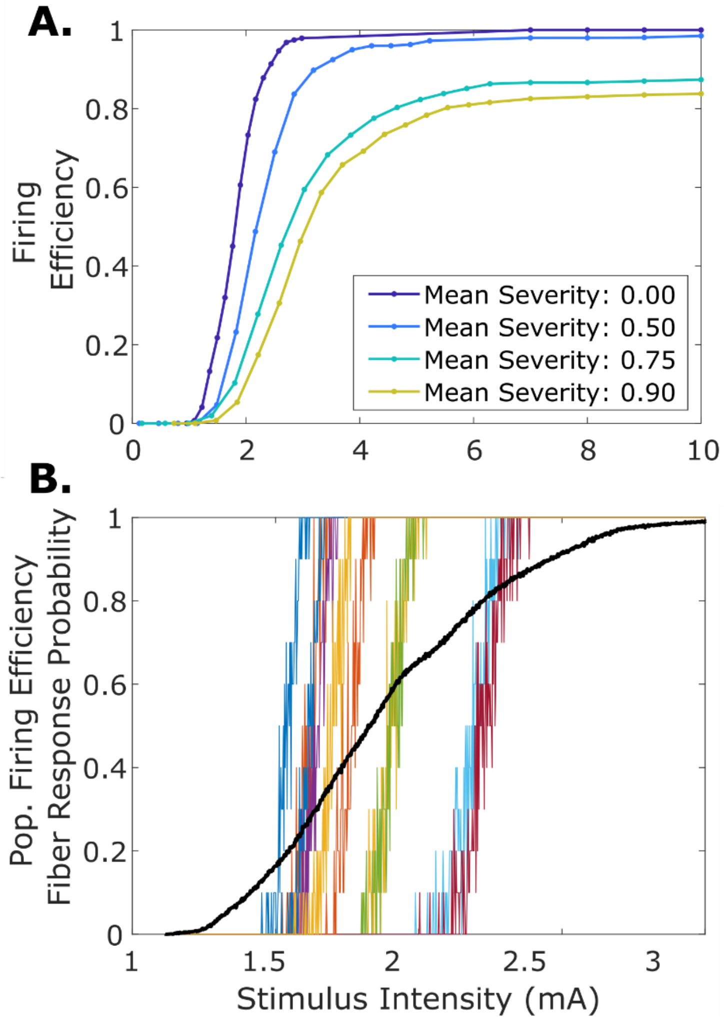

Figure 3.3- Normal and poorly myelinated population firing efficiency growth functions.

(A) Population level firing efficiency growth functions for four different populations: one normally myelinated and 50, 75, and 95% peripherally demyelinated. (B) Comparison of population firing efficiency growth function for normal population and single fiber response probability growth functions of constituent fibers.

We first consider how recruitment of fibers within populations with different levels of peripheral myelin loss varies with single-pulse stimulus intensity (**Fig 3.3A**). The normally myelinated population exhibits monotonic, sigmoidal growth with saturation at full recruitment of all fibers in the population. Myelin loss leads to a rightward shift of the growth functions along with a reduction in asymptotic recruitment efficiency and maximum slope of the growth functions. Each of these changes becomes progressively more severe as the mean level of myelination decreases.

Fig 3.3B illustrates how the response probability growth functions of individual fibers collectively yield the populations growth functions for a normal population. In this example and with demyelinated populations (not shown), individual fibers exhibit a much steeper growth function slope and, consequently, lower dynamic range than populations as a whole. This simple fact suggests that, at least in the setting of electrical stimulation, at any given population response efficiency the majority of fibers are either substantially sub- or supra-threshold while only a small minority of fibers lie within their dynamic range.

3.3.2 Level dependent variability in population response latency distributions

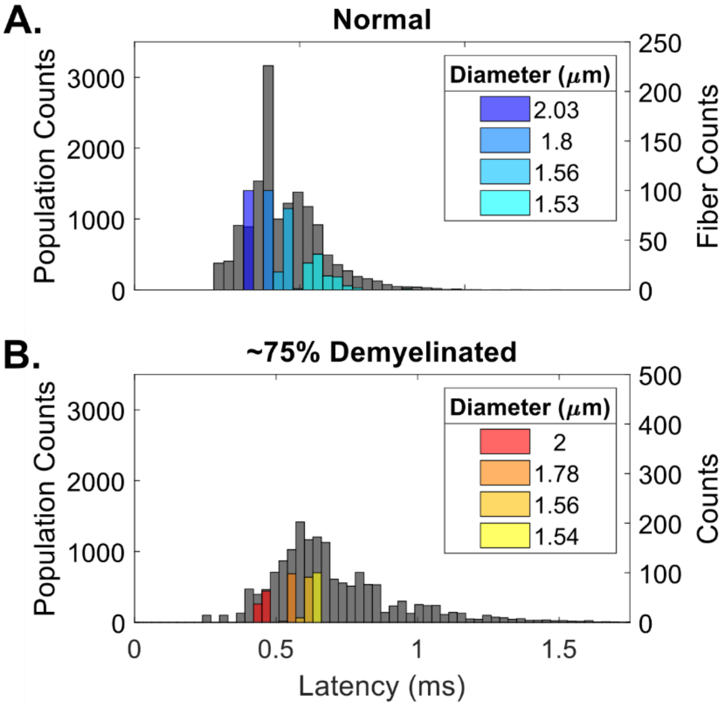

Figure 3.4- Normal and demyelinated population peri-stimulus time histograms.

Distributions of response latencies relative to stimulus onset for normal (A) and 75% peripherally demyelinated populations (gray). Colored distributions represent PSTHs for individual constituent fibers. The demyelinated population exhibits larger mean latency and jitter (F-test for equal variance $p < 0.001$, t-test for equal means $p < 0.001$).

In addition to altering recruitment, shifts in mean population myelin g-ratio also shift the spike timing and synchronicity across populations. **Fig 3.4A** shows how spike latency distributions across a normally myelinated population with representative single fiber distributions for comparison, at a firing efficiency of 0.75. This population distribution exhibits substantial variance while the responses of individual fibers exhibit jitter that is generally 10 to 100-fold smaller than the inter-fiber latency variance. Increased population mean g-ratio generally leads to broader PSTHs than normally myelinated populations even when g-ratio variance is held constant. **Fig 3.4B** shows peri-stimulus time histograms of responses of a population with a mean demyelination of 75% at rFE of 0.75. The demyelinated population latency distribution is substantially broader than that of the normally myelinated ones, despite individual fiber jitters remaining consistent across these 2 conditions (failed F-test for equal variance at $p < 0.0001$).

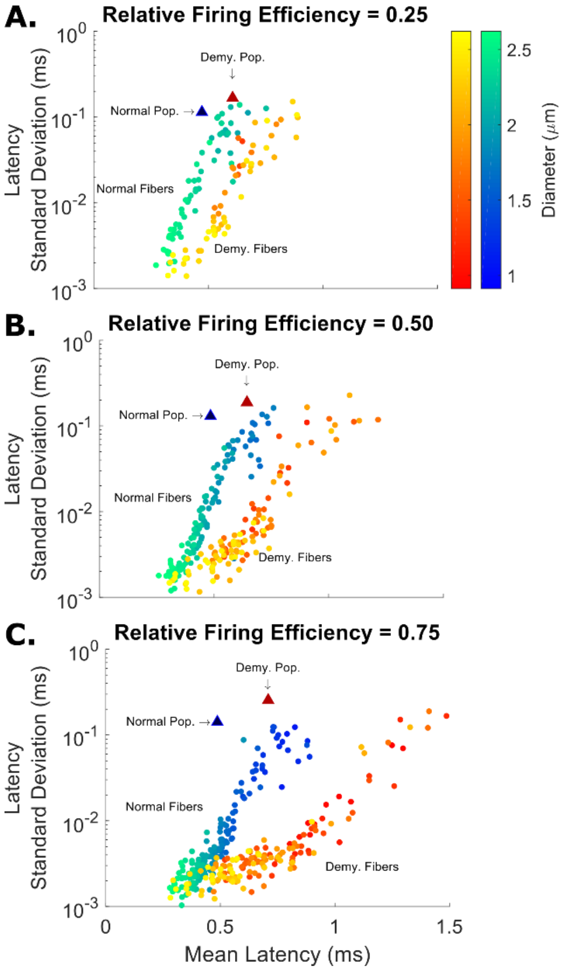

Figure 3.5- Normal and pathologically demyelinated fiber latency vs. jitter scatter plots.

Individual fiber mean latency is plotted against fiber jitter (colored circles) while overall population is plotted against inter-fiber mean latency variance (triangles) for two different simulated populations: normally myelinated (cool colors) and 75% peripherally demyelinated (warm colors). Color-mapping of fiber points represents fiber axolemma diameter. Panels (A), (B), and (C) present these data for firing efficiencies of 0.25, 0.5, and 0.75 relative to the population maximum.

These population level differences in response latency distributions exhibit substantial dependence on stimulus intensity levels. **Fig 3.5 A, B, and C** present fiber jitter plotted against mean fiber latency for each fiber within the selected normally myelinated (blue) and 75% demyelinated (red) populations, circles, at three different rFEs (0.2, 0.5, and 0.75). Population inter-fiber latency variance is plotted against population mean latency for each population as well, using filled triangles. There is relatively little difference between populations' latency distributions at low firing efficiencies, **Fig 3.5A,** because only the well myelinated fibers in the poorly myelinated population are active. At higher recruitment efficiencies, poorly myelinated fibers begin to become active in the lower-mean myelination population resulting in the addition of longer-latency responses to the population distribution and greater inter-fiber response variability. Since the stimulus intensities necessary to reach high FEs in the more poorly myelinated population are so intense, the well myelinated fibers within these populations are significantly supra-threshold in this regime and, consequently, exhibit very low jitter.

Zooming out and considering trends in summary statistics over the populations over all stimulus intensities, it is evident that fiber latencies, but not jitters, differ dramatically based on myelination. **Fig 3.6 A** presents mean latency as a function of firing efficiency for 4 different populations: one normally myelinated, 50 and 75% peripherally demyelinated, and 75% fully demyelinated. In general, mean latency increases progressively with mean demyelination severity across all rFEs. Latency increases modestly with rFE in normal population due to recruitment of smaller fibers with shorter internodes having slower conduction velocities and this increase is supplemented in the demyelinated population by poorly myelinated, slow-conducting fibers being recruited at higher rFEs. **Fig 3.6 B** presents mean fiber jitter with error bars representing inter-fiber jitter standard deviation plotted against population rFE. Notably, jitter decreases with rFE and remains quite consistent across populations at all efficiencies.

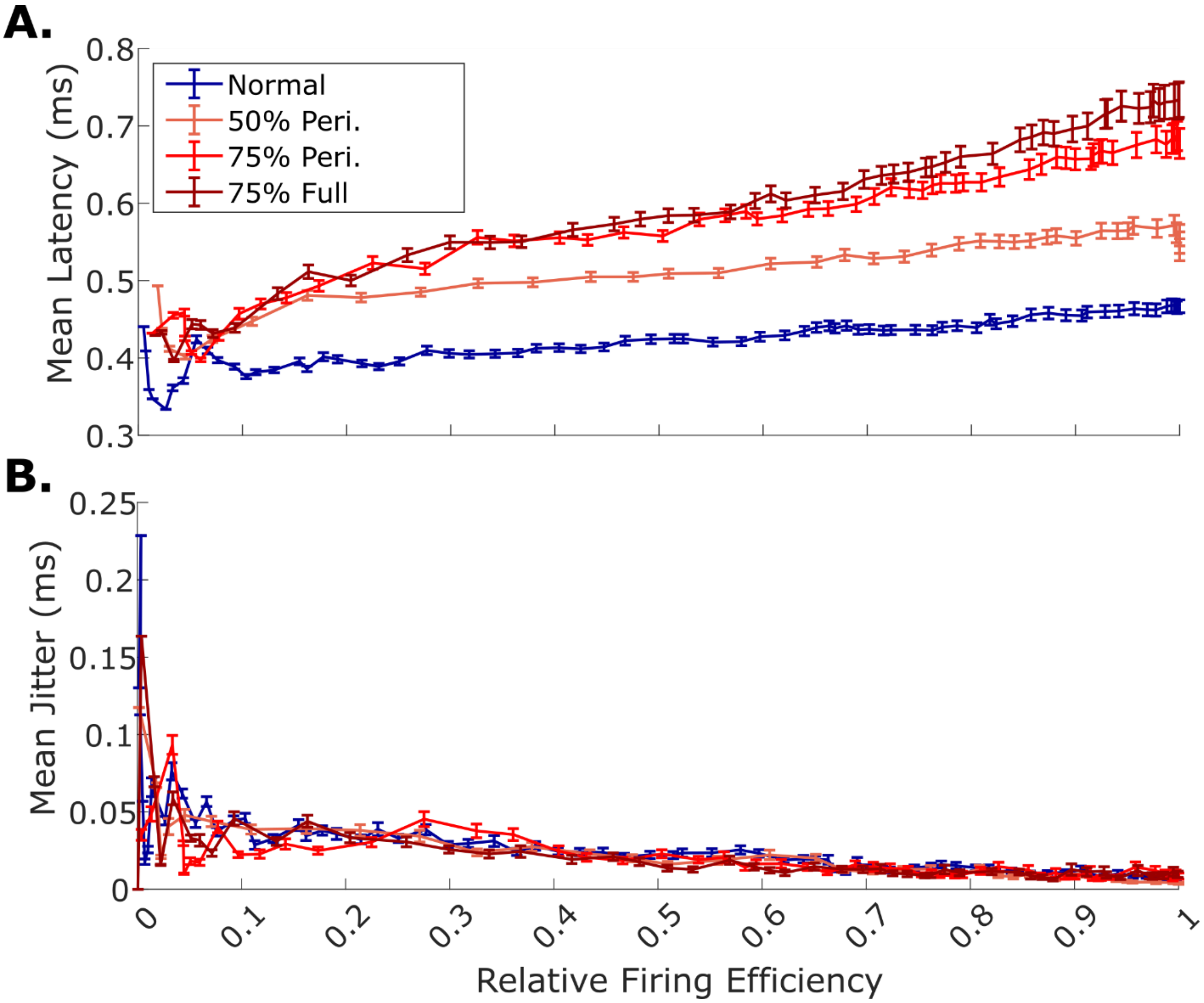

Figure 3.6- Mean fiber timing properties as a function of relative firing efficiency.

Mean latency (A) and mean jitter (B) are plotted as a function of firing efficiency relative to the population maximum for four populations: normally myelinated (blue), 50% peripherally demyelinated (orange), 75% peripherally demyelinated (bright red), and 75% full-length demyelination (dark red). Error bars represent standard deviation.

3.3.3 Population response latency distributions are consistent across pulse train cycles

To explore the predicted impacts of the population timing trends observed, we simulated ITD detection tasks using the responses of populations with different myelination states. The simulated stimuli were 100 ms, 100 pulse-per-second pulse (pps) trains modeled after those used in human psychophysical studies presented in Litovsky et al., 2012.(Litovsky et al., 2012) The pulse train delivered to the simulated left population was phase advanced from that delivered to the right population by a controlled ITD. At 100 pps, both the normal and demyelinated populations exhibited consistent cycle-to-cycle response latency distributions to the stimuli. No populations' response latency means or variances changed significantly between the first and 10th biphasic pulse presentation, data not shown, demonstrating that the 100 pps pulse rate is low enough to avoid the introduction of substantial memory effects. This suggests approximating detection of ITDs at this low rate as a relatively simple receive-operator process is reasonable.

3.3.4 Selection of fiber pairs for simulated ITD task

Introducing a phase delay to the pulse train presented to the 'right ear' population results in the introduction of an inter-aural latency difference between the mean population responses between simulated ears. This can be visualized by selecting pairs of fibers based on their relative diameter rankings within their respective populations and then calculating the mean latency difference of these paired fibers (**Fig 3.7 A and C**). The discriminability of these distributions from the null distribution can then be determined via ROC analysis to simulate discrimination of lateralized sounds from centered ones (**Fig 3,7 B and D**). Integration of these ROC functions enables prediction of the expected percent correct in a two-alternative forced choice task and enables identification of threshold, in the present case defined as 75% correct (**Fig 3.7 E**).

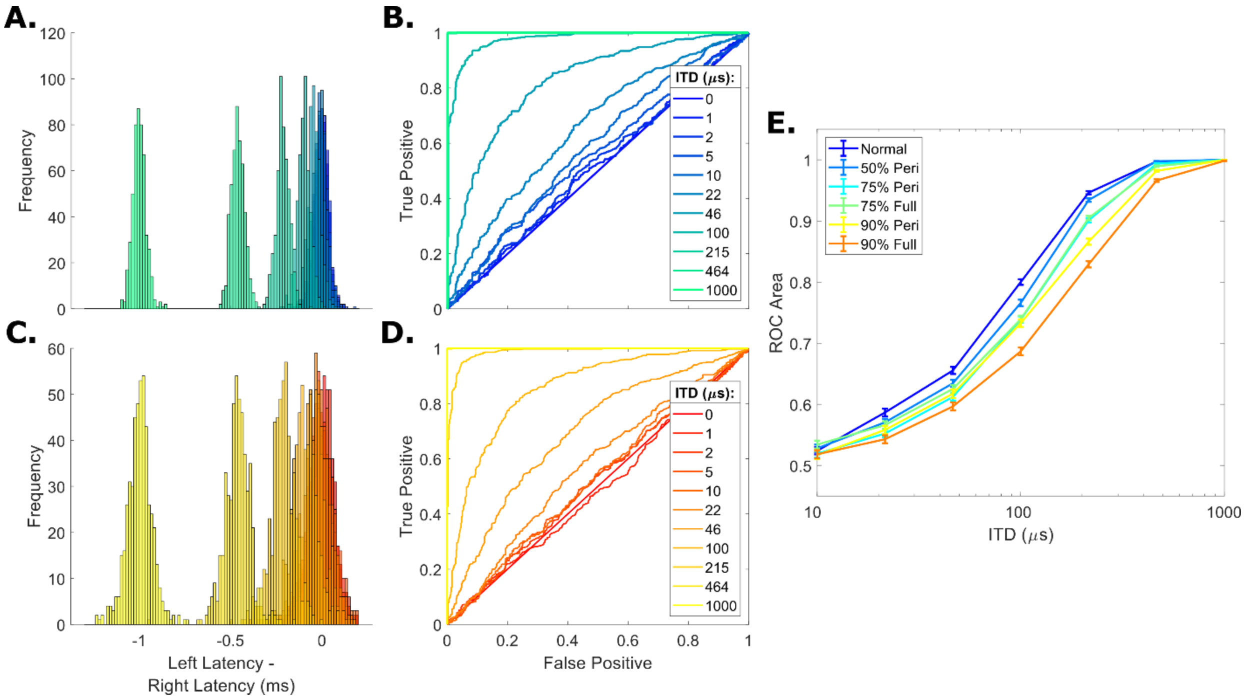

Figure 3.7- Receiver-operating characteristic (ROC) analysis of latency differences.

Left-right population latency difference distributions are plotted for a normal population (A) and 75% peripherally demyelinated population (C). From these latency difference distributions, ROC curves were produced for 10 different ITDs where the no-signal comparison was 0 µs ITD (B and D). Integrating these functions enables calculation of the area under the ROC curve for each population as a function of introduced ITD (E), presented for 6 different populations, an approximation of optimal detection performance. Error bars represent standard error of the mean.

One major consideration for this approach is the selection of the sub-population of fibers contributing to simulated ITD detection. As noted in section 3-1, at any given population firing efficiency the vast majority of fibers are either substantially sub- or supra-threshold. Since deafferented fibers do not exhibit spontaneous activity, many fibers will not fire spikes and cannot contribute to encoding of response timing information. These effects were explored in our ITD-task simulations by modifying the strategy for selecting fibers for comparison in each population and the number of fiber pairs included in the latency mean calculations. **Figure 3.8** provides threshold comparisons across sub-population selection strategies and fiber pair numbers. Limiting the selection to only those fibers with jitter less than the mean of their respective populations yields 75% correct thresholds varying between 10 and 40 µs, depending of the number of pairs selected, significantly below the best CI user JNDs. The active and random selection approaches produce similar optimal performance, with thresholds on the order of ~15 µs, with 200 fiber pairs. However, when only a small number of fiber pairs averaged into the population means random selection strategy produces substantially greater thresholds than the active due to the inclusion of quiescent fibers, yielding a reduced number of functional pairs. For simulations involving population comparisons, we focus on the active and random sub-population selection approaches in order to enable exploration of the importance of failed fiber recruitment and to avoid the aberrantly good thresholds produced via the lowest-jitter approach.

Another important consideration for this modeling approach is the number of fiber pairs included in each mean left-right latency difference. In general, threshold decreases with increased number of pairs but with diminishing returns, and the nature of this relationship depends on the sub-population selection strategy used. When selection is limited to the lowest-jitter fibers, thresholds are quite low, on the order of 50 µs even with only a few fiber pairings and then quickly improve to saturation with only 25 comparisons. In contrast, the other selection strategies provide mean performance on the order of 200 µs when less than 10 fibers are used. This quickly improves to saturated performance for the near-threshold condition with 25 or more comparisons. On the other hand, the sub-saturating approach does not begin seeing threshold improvement until a greater number of fibers are averaged and thresholds continue to improve with this approach beyond 100s of comparisons. A 2-way ANOVA analysis of this data supports the importance of fiber pair number and selection strategy, yielding significant effects for these factors and their interaction with $p < 0.0001$.

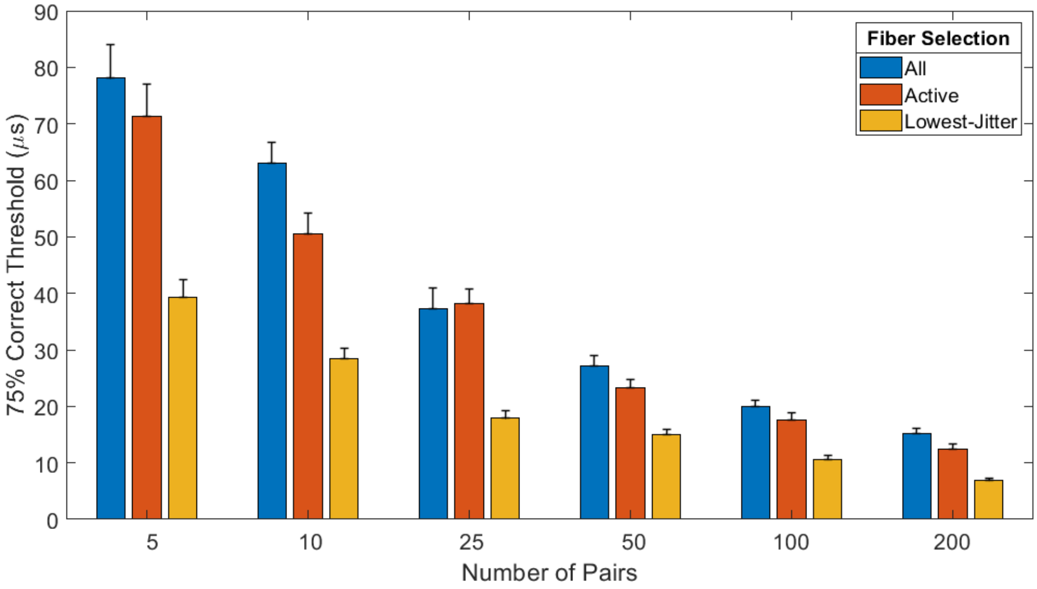

Figure 3.8- Dependence of detection thresholds on fiber counts and selection strategies.

The mean 75% correct threshold found from the ROC area under the curve function is plotted for six different numbers of fiber pairs and three different selection strategies. The number of replicates was 10 for each condition and error bars are standard error of the mean. A 2-way ANOVA yielded significant effects of both fiber selection method and number of pairs on thresholds ($p < 0.0001$), and a strong interaction term between these factors ($p < 0.0001$).

3.3.5 Demyelination Degrades Simulated ITD Task Performance

To explore the effect of heterogenous demyelination within a population on the simulated ITD detection task, we repeated the experiments using populations with varying degrees of both peripheral and progressive demyelination. **Figure 3.7 C** illustrate the distributions of mean latency differences for a population of fibers that is on average 75% demyelinated over 75% of the fiber lengths at a relative firing efficiency of 0.7 using the random sub-population selection strategy. These distributions exhibit significantly larger variance than those of the population with normal myelination heterogeneity (**Fig 3.7 A**). This greater variance in the mean latency distributions results in a downward shift in the resulting ROC curves for the demyelinated population (**Fig 3.7 D**). Integrating such ROC curves for each simulated ITD for each population produces the area under the curve (AUC), percent correct, functions presented in **Figure 3.7 E**. Demyelination yields rightward shifts of the ROC-AUCs that are relatively modest with a low degree of demyelination but become progressively more severe with greater myelin loss. Notably, this effect depends on both the severity of myelin loss and whether it impacts just the peripheral region of axon or entire fiber.

Using interpolation to determine the 75% ITD detection threshold for each population enables comparison of the degree of rightward shift for each population under different stimulus conditions and simulation assumptions. **Figure 3.9 A** presents the 75% ITD detection thresholds for populations with different myelination states using the active-only sub-population selection strategy at three different relative firing efficiencies: 0.2, 0.5, and 0.7. A 2-way ANOVA of this threshold data yields significant effects of population, level, and their interaction (all with $p < 0.0001$). Multiple comparison testing with Bonferroni correction found significant differences between group mean thresholds driven by level and population differences. Notably, normal population threshold decreased modestly with increasing recruitment efficiency from a value of approximately 52 μs at 0.2 rFE to 38 μs at 0.7 rFE ($p < 0.001$). Populations with modes demyelination severity (≤75%) mean thresholds did not change significantly across all rFE. Importantly, strongly demyelinated populations thresholds increased with rFE, for instance a 90% progressively demyelinated population's threshold increases from ~40 μs at 0.2 rFE to ~66 μs at 0.7 rFE ($p < 0.001$), demonstrating the significant impact of increased population-level latency variability can have on temporal cue encoding across a population. The result of these different level-dependent dynamics is that all populations exhibited similar thresholds at low rFE but that those with 90% severity exhibited significantly larger thresholds at high rFE ($p < 0.0001$).

With the random approach (**Fig 3.9B** most of the populations exhibit a monotonic decline in threshold with increased rFE that is dramatically larger than that level-dependent changes observed in the active-only simulation. Thresholds using this strategy are substantially higher at low rFEs across all populations. Again, a 2-way ANOVA of this threshold data yields significant effects of population, level, and their interaction (all with $p < 0.0001$), however, multiple comparison testing with Bonferroni correction found a different pattern of significant differences between group mean thresholds. The normal population's threshold is higher at 0.2 rFE (~100 µs vs. 45 µs) but approaches the active-only thresholds at high rFEs (~40 µs), this level-dependent decrease was significant with $p < 0.0001$. The most severely demyelinated populations exhibited some non-monotonicity in this threshold change, increasing from 102 µs to 125 µs from rFE 0.2 to 0.5 before returning to 100 µs at 0.7 rFE, though these changes were not significant. Again, this results in all populations having similar thresholds at rFE = 0.2 but the normal population having a significantly lower threshold than the poorly myelinated populations at rFE = 0.7 ($p < 0.0001$). The severe peripheral demyelination population exhibited a

By taking the difference of the mean thresholds for each population and relative recruitment efficiency for these two selection strategies, the contribution of poor fiber recruitment can be considered isolated from differences in latency distributions between fibers (**Fig 3.9C**). This difference is large and of similar magnitude (55-65 µs) for most populations at rFE = 0.2 due to the preponderance of inactive fibers. At high rFE, this difference is quite low for the normal population since most fibers are recruited and the latency variability is low, however, in the poorly myelinated fibers the difference remains relatively large (~45 µs). These differences show that improved recruitment improves thresholds for all populations, even when increased latency variability is accounted for, however, this difference is significantly larger for the more normally myelinated populations, indicating the contribution of latency dispersion to elevated thresholds in poorly myelinated populations.

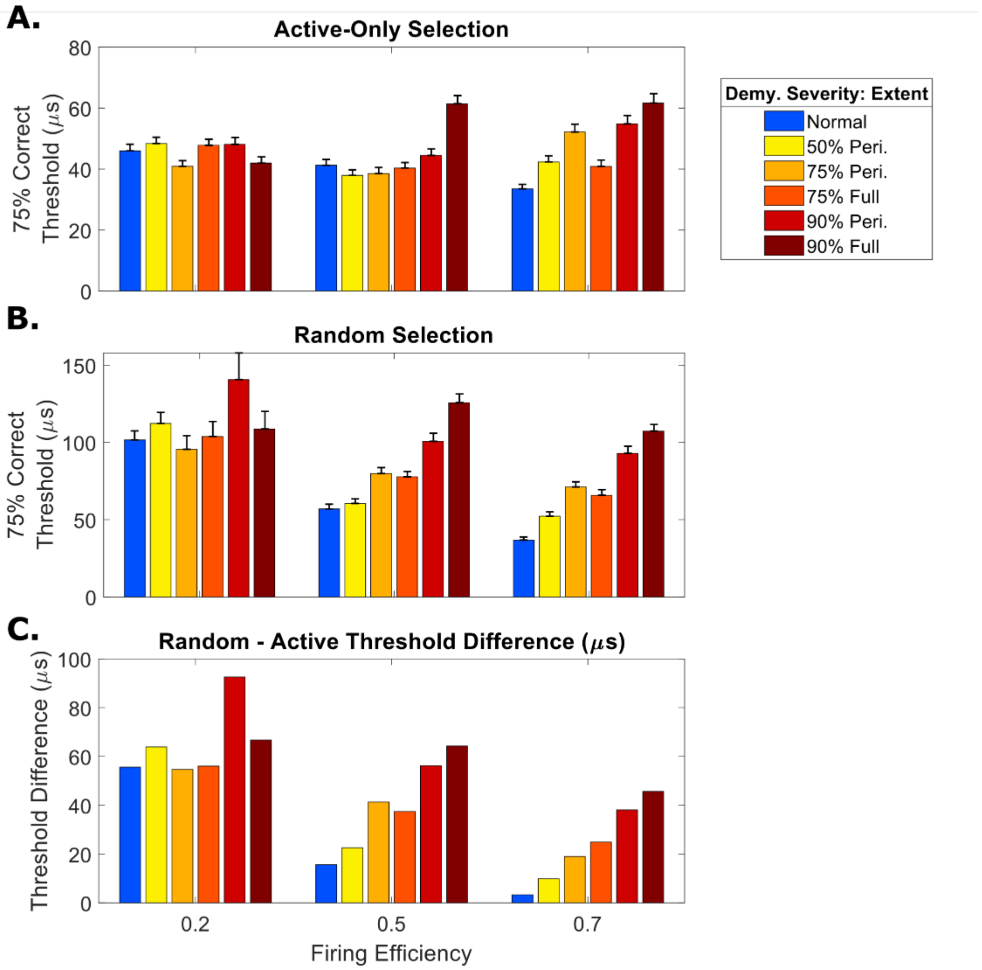

Figure 3.9- Detection threshold variance due to population myelination states.

The 75% correct thresholds are presented as a function of relative firing efficiency for five fiber populations: a normal population; 50%, 75%, and 90% peripherally demyelinated; and 75 and 90% fully demyelinated. Panels (A) and (B) present results using active-only and random selection, respectively while panel (C) shows the threshold difference for each population between simulations produced using these two strategies. A 3-way ANOVA with performed for the active and random selection thresholds found that the population, level, and selection-strategy factors and their 2 and 3-way interactions terms were significant predictors ($p < 0.0001$ level). Error bars for (A) and (B) are standard error of the mean.

3.4 Discussion

The shape of neural recruitment functions for simulated populations changed with their mean level of myelination (**Fig 3.3**). The asymptotic response probability and maximum slope of population input-output functions decreased as mean g-ratio increased. The slope change leads to an increase in dynamic range for poorly myelinated fibers but with fewer active fibers encoding this range. This suggests that despite increased dynamic range these poorly myelinated populations will have fewer discriminable firing efficiency steps. An implication of this reduction is that at any given firing efficiency these populations will have fewer fibers near threshold, neither saturated or entirely quiescent, and, therefore, able to encode information about a signal in the presence of noise.

In addition to whether fibers are within their dynamic range, another important aspect of population activity for encoding timing information is the coherence of response latencies. This feature of population behavior was interrogated by exploring the trial to trial latencies of individual fiber and population responses across the firing efficiency spectrum (**Fig 3.4**) We observed significantly increased population level variation in response latencies that was driven by increased inter-fiber variability in the absence of substantial changes in within-fiber jitter (**Fig 3.5 & 3.6**). Interestingly, this elevated population latency variability is particularly pronounced at high firing efficiencies since at low efficiencies the healthiest fibers are preferentially recruited.

By utilizing these responses in a simulated ITD detection task, we sought to develop an understanding of how population level variance in spike timing might impact human psychophysical performance. This approach requires making a number of assumptions about how the auditory pathway pools and processes spikes from across the population of fibers. Careful consideration of these choices is critical for informing and understanding comparisons between populations differing in physiological health and also suggests testable hypotheses regarding auditory processing more broadly.

3.4.1 Noise likely constrains central processing of timing cues

In this simulation approach, we must select which fiber pairs' latencies are combined into mean responses for ROC analysis. We have explored 3 different selection strategies: random, only active fibers (firing in response to at least one pulse on at least one trial), and those with low jitter (less than the population mean). If the task of the auditory system was to precisely determine timing in noiseless environments the last approach would likely be optimal, and this is reflected in our results where the lowest-jitter selection strategy yields ITD JNDs in the 10s of μs, depending on the number of fiber pairs included. However, this performance is an order of magnitude better than that seen in implantees suggesting other requirements of auditory signal processing may interfere with this strategy. In reality, the auditory system must detect signals in the presence of noise and the lowest-jitter, saturated fibers are most likely to be saturated in noisy conditions and, therefore, will carry little signal information. As such, it is logical that real performance depends at least partly on latency variability in fibers nearer threshold. In contrast, the lowest-jitter selection approach preferentially selects saturated fibers. This result suggests that the real-world demand of detecting signals in noise constrains binaural cue processing and prevents selective analysis of those neurons with the lowest spike jitter.

Degeneration of SGNs with prolonged deafness has been observed in both humans and model animals, though the time course of this process is species dependent.(Incesulu and Nadol, 1998; Kroon et al., 2017; Seyyedi et al., 2014; Shepherd et al., 2004; Sly et al., 2007) While we did not explicitly model degeneration here, with severe demyelination we observed failure to recruit some fibers at all stimulus current intensities tested, resulting in functional degeneration. Comparing the findings with the active-only and fully randomized sub-population selection strategies enables interrogation of the effect of functional fiber loss to be observed in the form of a reduced number of spikes contributing to the latency difference means. The inclusion of sub-threshold fibers led to a significant elevation in ITD JNDs in normal fibers but had an even greater effect in poorly myelinated fibers, (**Fig 3.9)**, underlining the possibility of dramatic temporal processing ramifications of fiber loss.

3.4.2 Estimating number of fiber pairs involved in CI single-electrode ITD judgements

Another important consideration in this modeling approach is the number of different fiber pairs to be included in the population latency difference comparisons. While estimating the number of fibers/spikes involved in this task is difficult, even rough approximation provides useful context for simulation. Forward masking experiments in cochlear implant users by Bierer and Faulkner found psychophysical tuning curve half-widths on the order of 2-4 electrodes, a distance of 2-4 mm.(Bierer et al., 2011) A typical human cochlea contains on the order of 3000 inner hair cells along the ~35 mm cochlea each innervated by ~11 afferent neurons, yielding approximately 30,000 type 1 auditory nerve fibers.(Nadol, 1988) If a pulse recruited half the fibers innervating a region of cochlea the size of an average psychophysical tuning curve half-width, a rough approximation of how many fibers a saturating stimulus at this electrode would recruit, this would yield activity in about 750-1500 auditory nerve fibers. An electrical pulse would recruit fibers nearest the electrode most readily and current would rapidly fall off and recruit fewer fibers as distance from the electrode increased, so we anticipate a significantly lower level of recruitment, perhaps in the hundreds of fibers. At more modest current levels, as would be expected at the maximally comfortable level used in most CI psychophysics, we might expect substantially less than this level of recruitment. As such, in a cochlea without any degeneration of auditory nerves (an unlikely situation in an implanted individual) we anticipate single pulses at MCL to recruit tens to hundreds of fibers but admit this is a quite rough estimate so explored a range of fiber pair numbers (**Fig 3.8**). ITD 75% correct threshold decreases exponentially and monotonically as fiber pair number increases from 5 pairings up to 1000 using the random sub-population selection strategy. With only 5 or 10 fibers this strategy yields a mean 75% threshold of 60 and 80 µs, respectively, approximately the minimum ITD JNDs observed in CI recipients. With 25, 50, and 100 pairings it yields thresholds of 40, 25, and 20 µs respectively that, if a central noise source is invoked, still seem consistent with the psychophysical findings. These thresholds decrease yet further at higher numbers of pairings to the point that they become too precise to be consistent with findings in CI recipients.

With prolonged deafness, spiral ganglion cell counts can decline to 10% or less of the normal value.(Incesulu and Nadol, 1998) As such it is of interest to consider the predicted outcomes of ITD encoding when only tens of fibers are recruited as well. Our ability to select the number of fiber pairs allows us to explore how degeneration would be expected to impact ITD encoding abilities. If we consider thresholds with 100 and 10 pairings coming from the normal population, we observe an approximately three-fold increase in ITD detection threshold, supporting the hypothesis that the number of fibers available to encode timing cues is likely a critical contributor to ITD detection.

3.4.3 Demyelination elevates ITD detection thresholds via latency variability and reduced number of looks

In our comparisons of ITD detection between populations, we explored the impact of demyelination and its interaction with degeneration on encoding temporal information. We focused our analysis on two sub-population selection methods: random (**Fig 3.9 A**) and active (**Fig 3.9 B**) fibers. The first of these methods allows for assessment of the impact of both effects of inter-fiber latency dispersion and poorer fiber recruitment on ITD detection thresholds. In contrast, the second enables assessment of the latency variability effect in isolation. Using the first strategy, demyelination causes a severity-dependent increase in ITD threshold prominent at high relative firing efficiencies but almost non-existent at lower relative firing efficiencies when the most affected fibers are quiescent. When analysis is limited to only active fibers and the recruitment difference is eliminated the demyelinated populations exhibit significant, albeit reduced, elevations in their thresholds. This suggests the latency variability present in demyelinated populations at higher recruitment levels contributes to the degradation of temporal encoding fidelity. By taking the difference in threshold between the completely random and solely active subpopulation strategies (**Fig 3.9 C**) the effect of poorer recruitment can be isolated. The results of this approach suggest that differences in recruitment likely also dramatically degrade ITD detection abilities and that this effect is of approximately the same magnitude as the latency difference effect. In short, increased inter-fiber latency variability and reduced number of looks synergistically degrade fine temporal information available to central binaural cue detectors.

3.4.4 Future directions

These findings suggest that the fundamental nature of electrical current spread interacting with normal heterogeneity in neural properties likely produces unavoidable variability in temporal cue encoding, that is intensity dependent. Moreover, pathological demyelination leads to even greater inter-fiber variability in excitability that produces additional greater latency dispersion and poorer temporal cue fidelity. Interestingly, this behavior was observed even with the simplifying assumption of a perfectly co-localized fiber population and an extremely simple electrical cochlear structure. Implementation of more biological accurate spatial distribution of auditory nerve fibers relative to stimulating electrodes and a multi-compartment cochlear model would be expected to produce additional variability in site of excitation and, therefore, response latencies between auditory nerve fibers. Exploring the magnitude of this variability and how it might interact with demyelination and other pathological changes will be valuable.

The simulations presented focus on electrical stimulation which introduces fundamental changes in neural recruitment. Exploring the nature of population encoding of simple temporal cues in an organ of Corti-based acoustic hearing model, such as that created by Zilany et al. would enable quantification of the expected degree of temporal distortion expected from transitioning from acoustic to electrical stimulation.(Zilany et al., 2014)

Chapter 4- Exploring how diameter-dependent degeneration alter electrically-evoked compound action potentials

4.1 Introductions

Electrically evoked compound action potentials (eCAPs) are Intracochlear recordings of cellular responses to implant stimulation that can be obtained in both humans and animal models. In principal, these recordings provide an objective measure of neural response to stimulation. Consequently, several groups have explored the prospect of using eCAPs to guide implant mapping or as prognostic tools. A relationship between characteristics of the eCAP amplitude growth functions (AGFs) and speech recognition outcomes in adults has been difficult to consistently demonstrate (DeVries et al., 2016; Eijl et al., 2017; Kim et al., 2010; Miller et al., 2008). One of the more promising eCAP related measures involves assessing the effect of stimulus inter-phase gap on eCAP AGF slopes. Schvartz-Leyzac and Pfingst observed a between-ear correlation between the difference in AGF slopes measured with short and long inter-phase gaps (IPGs) and speech recognition performance (Schvartz-Leyzac and Pfingst, 2017). However, this finding depended on a tightly controlled within-subject comparison and has been difficult to extend to between-subject purposes. de Vos et al.'s 2017 meta-analysis concluded the evidence supporting the use of eCAP data for cochlear implant fitting purposes is weak; noting that eCAP thresholds are poor predictors of both T- and C-levels (de Vos et al., 2018). These challenges in identifying clinical roles for the use of eCAPs highlight the principal challenge of interpreting them, how there exists enormous eCAP variability between individuals, and even amongst electrodes within a single implant, that cannot be adequately explained and frustrates interpretation.

To better understand the sources of eCAP variability, several groups have explored how eCAP AGF characteristics change as duration of deafness or implantation increases in animal models. Interestingly, threshold and peak amplitude changes exhibited such large inter-animal variability that no consistent correlation with duration of deafness or spiral ganglion neuron (SGN) density has been found. In contrast, the slope of eCAP growth functions has repeatedly been found to correlate with SGN density (Pfingst et al., 2015; Prado-Guitierrez et al., 2006; Ramekers et al., 2014). Notably, this effect appears even more prominent when the difference in AGF slope between long and short IPG conditions is considered, a phenomenon termed the inter-phase gap (Prado-Guitierrez et al., 2006; Ramekers et al., 2014). This effect suggests a significant change in the temporal integration properties of neural responses. Adenis et al.'s study exploring eCAP threshold growth functions in acutely and chronically implanted guinea pigs to stimuli where delivered charge was controlled by varying either pulse amplitude (PA) or phase durations (PD) provides further evidence for such a change (Adenis et al., 2018). While they observed great between-animal heterogeneity of relative growth functions, particularly in chronically deafened animals, the two groups demonstrated distinct differences in sensitivity to PA and PD stimuli. With high total charge delivery, response amplitudes to phase-duration-based stimuli lagged those to amplitude-based stimuli of equal net charge in acutely implanted animals, reflecting the importance of neural time constants even amongst healthy neurons. While in deafened animals, this differential PA/PD sensitivity was much less prominent. Collectively, these findings point to changes in the temporal integration properties of neural populations as a key feature that changes with prolonged deafness in animal models, however, the biophysical mechanisms that underly such changes are poorly understood.

Studies exploring the microarchitectural outcomes of hearing loss have identified pathological changes in SGNs that may contribute to eCAP changes. Studies correlating threshold measures of CI recipients in life with post-mortem SGN counts have observed significant interaural correlations between psychophysical and histological outcomes (Incesulu and Nadol, 1998; Seyyedi et al., 2014). Experiments in rats, guinea pigs, and cats demonstrate that they too exhibit degenerative processes, albeit with species dependent time courses (Kroon et al., 2017; Shepherd et al., 2004; Sly et al., 2007). Interestingly susceptibility to damage appears to vary across the SGN population in a threshold and diameter-dependent manner. With acute deafening, loss of peripheral dendrites, termed synaptopathy, impacts high-threshold, low-spontaneous-rate fibers synapsing on the pillar side of inner hair cells (Furman et al., 2013; Kujawa and Liberman, 2009; Makary et al., 2011; Wise et al., 2017). Unpublished data from the Ramekers group suggests this susceptibility of large, high-threshold fibers leads extends into peripheral process degeneration; they observed both a reduction in axon counts and downward shift in the diameter distributions of peripheral nerve fibers in guinea pigs with a protracted duration of deafness. In short, these studies indicate that both frank and functional degeneration of SGNs may occur following deafening and the expected functional outcomes of each should be explored.

Previous efforts to simulate eCAPS have focused on putatively normal fibers and so cannot speak to the impact of such pathological changes (Briaire and Frijns, 2005; Rubinstein, 2004). Here we have extended a stochastic, biophysical, computational model of electrical stimulation of spiral ganglion fibers to simulate eCAPs in populations with different distributions of axon size, based on measurements from guinea pigs with different durations of deafness, to explore whether size-dependent degeneration might underlie a portion this variability. These simulated eCAPs recapitulate many of the key morphological features of those recorded both in CI recipients and animal models while enabling simultaneous analysis of spiking activity. Reduced mean diameter and diameter distribution variance produced morphological changes in eCAP waveforms like those observed by Ramekers et al. with long durations of deafness.

By exploring different populations' response growth functions to stimuli with different IPGs or PDs their behavior could be compared to that observed in long-term deafened/implanted animals by Ramekers et al. and Adenis et al. (Adenis et al., 2018; Ramekers et al., 2014). The simulated pathology reproduced many of the key dimensions of variability observed in these studies including alterations in relative slope and peak response amplitudes but failed to capture others, notably thresholds differences between PA and PD-based growth functions. Analysis of fibers' strength-duration curves suggests alterations in the distribution of temporal integration properties across the populations drive much of this eCAP variability. Notably, while eCAP growth functions exhibited a notable decrease in maximum amplitude with long pulse widths, spike efficiency growth functions did not. This analysis of spike latency and eCAP peak amplitude demonstrates that variability in amplitude growth reflects both fiber recruitment and response synchrony changes. These results suggest that asymmetric patterns of neural loss may drive changes in eCAP properties observed with prolonged deafness.

4.2 Methods

4.2.1 Single Fiber Simulation

The population responses in this study consist of collections of 200 Type 1 SGN fibers each represented as a single segmented cable, as previously described, with a modification to the terminal segments of the fiber to approximate the unmyelinated dendritic and central terminals. Within individual fibers, the membrane potential within each segment during stimulation by an extracellular electrode is described by a partial differential equation relating axial current to capacitive, leak, applied, and ionic currents. Behavior of each of these currents is dictated by biophysical parameters, originally derived from anatomical and physiological data from, principally feline, auditory nerves and then tuned until simulated electrophysiological properties were like those determined from cat recordings. The present study uses identical parameters to those used in Resnick et al., 2018 except for the specific terminal process, demyelination, and degeneration approaches described below.

Each fiber consists of nodes, with intervening internodes, with segment lengths that scale with fiber caliber but a constant total length approximately equal to that between the auditory periphery and cochlear nucleus in cats. Internodes are each divided into 9 segments possessing purely passive electrical properties while nodes of Ranvier are represented as single segments possessing both passive elements and stochastic, voltage dependent ionic currents. Internode fiber diameters for the populations were selected to approximate empirically derived diameter distributions from animal models with different durations of deafness, described in further detail below. The length of internodal segments is equal to the product of their diameter and a constant length to axolemma diameter ratio of 92 : 1 (Arnesan and Osen, 1978; M. Charles Liberman and Oliver, 1984). Membrane and axonal resistances of all segments scale with their surface and cross-sectional areas, respectively, and do not vary with myelination state. While nodal segment membrane capacitance was fixed as a product of the membrane specific capacitance and the nodal area, internodal segment capacitance was manipulated to simulate myelin loss as described further below. The terminal peripheral and central segments of the fiber were enlarged by a factor of 20 to represent the large unmyelinated regions of the dendrite and axon terminal (Robertson, 1983). This enlargement was necessary to facilitate the local circuit re-hyperpolarization that produces the P2 peak of the eCAP waveforms. Importantly, this enlargement did not significantly alter the single-unit properties (notably response latency and jitter) of the fibers which were originally tuned to match those recorded in healthy cats.

The behavior of the stochastic, voltage-dependent ion channels within nodal segments was modeled using a Markov jump process (Gillespie, 1977; Mino et al., 2004; Mino and Grill, 2002). Total ionic current was defined as the sum of sodium, slow potassium, and fast potassium currents. This procedure enabled computationally efficient simulation of channel dynamics within each segment while maintaining an accurate representation of their stochastic behavior (White et al., 2000). Nodal segment diameter was defined as equal to the internodal diameter multiplied by the constriction factor 0.5. The number of each channel type was determined by multiplying the nodal surface area times empirically derived ion channel densities, thus the number of channels scale with the diameter squared.

Simultaneous solution of numerical approximations of the system of differential equations described by Eq. 1, with the relevant segment geometrical properties, ionic currents, and applied field induced currents (described in section 2-3), by an implicit Crank-Nicholson scheme yields the potential within each segment of the model fibers for each time step of the simulation (Mino et al., 2004). A time step of 1 μs was used for all simulations. Simulations were performed within MATLAB using compiled executable functions for computationally intensive steps.

4.2.2 Creation of populations with diameter and myelination heterogeneity

To explore diameter-dependent degeneration of auditory nerve fibers, the diameter distributions for the model populations were constructed to match those measured using electron microscopy by the Ramekers group for three different guinea pig populations: acutely, 2-week, and 6-week deaf animals (unpublished data). **Figure 4.1** illustrates the diameter probability density functions determined by the Ramekers group with least-squares optimized log-normal functions fit to them. Model ‘normal’, ‘2-week deaf’ and ‘6-week deaf’ populations were constructed by drawing

200 diameters from each of these log-normal distributions, uniformly distributed in probability space. For these populations, all fibers' g-ratios were selected from the normal myelination heterogeneity distribution described above.

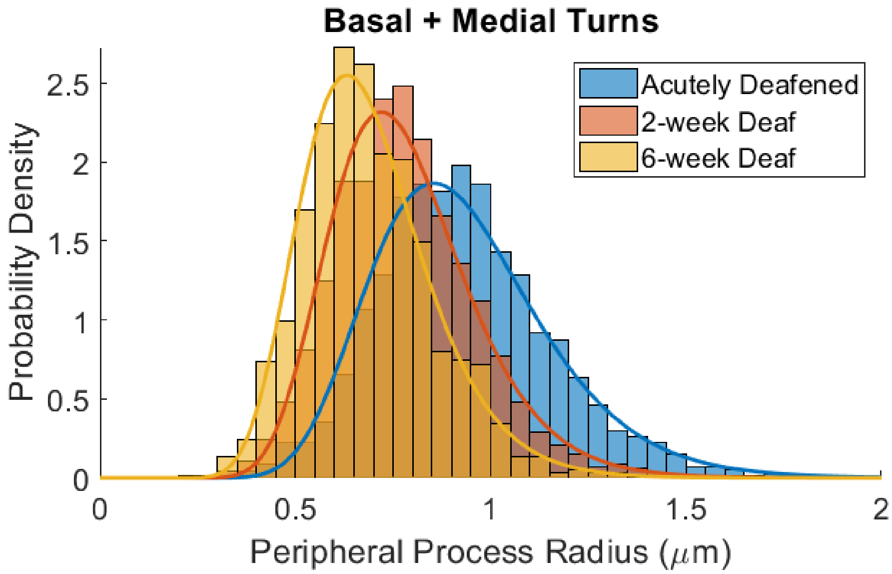

Figure 4.1- Deafness induced shifts in peripheral process diameter distributions.

Histograms of peripheral process radii measured using electron microscopy from acutely deafened(blue), 2-week deaf (red), and 6-week deaf (yellow) Guinea Pigs by Ramekers et al. (unpublished data shared with permission). Overlying curves illustrate least-squares fitted log normal distributions diameters were selected from for degeneration experiments.

Previously, we implemented a modified version core-conductor model for simulating fiber myelin loss (Resnick et al., 2018). In this approach, internodal plasma membrane resistance and capacitance were modeled as being in series with the myelin sheath's, creating a core-dual conductor model. Since the specific resistance of lipid bilayer without ion channels embedded in it is of a similar order to that of myelinated axon (10^6-10^8 ohm*cm^2 and 4.45*10^8 ohm*cm^2, respectively), resistance was fixed independent of myelin width (Imennov and Rubinstein, 2009; Montal and Mueller, 1972). Assuming the plasma membrane dielectric constant remains consistent between nodal and internodal segments, the plasma membrane capacitance of the internode can be estimated using the nodal value divided by the constriction factor. The total internodal capacitance can then be calculated by adding the plasma membrane and myelin contributions in series:

$$\frac{1}{C_{internode}} = \frac{1}{C_{my}} + \frac{1}{C_{m,internode}} = \frac{\log(D/d)}{\log(1/0.6)C_{my,normal}} + \frac{c_{constric}}{C_{m,node}} \tag{2}$$

We extended this model to reflect normal neural myelination heterogeneity by generating a g-ratio (axolemma diameter : myelin sheath diameter) distribution matched to that measured using electron microscopy in normal-hearing mice by Wan and Corfas, 2017 (Wan and Corfas, 2017). Our simulated normal distribution possesses a mean g-ratio of 0.64 and standard deviation of 0.24, see **Fig 3.1B**. Individual fibers g-ratios were selected from this distribution and used in conjunction with the pseudo-randomly generated internode axolemma diameter according to Eq. 2.

4.2.3 Stimulus design

Simulated fiber populations were stimulated by an extracellular disk electrode as derived previously by Rubinstein and used in previous versions of this model (Imennov and Rubinstein, 2009; Mino et al., 2004; O'Brien et al., 2016; Resnick et al., 2018; Rubinstein, 1988). By assuming that injected current propagates through an isoresistive medium, the applied potential difference between adjacent segments can be expressed as a function of the injected current and the segment-electrode distance. The field potentials along each fiber can then be calculated for each time step during stimulation for a selected current waveform. All fibers were treated as co-located 3 mm from the electrode because it simplifies the simulation and nerve fibers within the Spiral Ganglion are often bundled. Populations were presented with individual cathode-first biphasic pulses with experiment-dependent phase duration (PD), pulse amplitude (PA), and inter-phase gaps. Following stimulus presentation, simulations were continued for 4 ms to enable monitoring of fiber-potential evolution.

4.2.4 eCAP simulation

eCAPs for each populations response to each stimulus condition were simulated by first determining the single fiber action potential (SFAP) response for each fiber within the population and then summing them. SFAPs, in turn, were calculated at each time step by modeling the potential at a point recording site due to the currents through each cable segment at that instant, with these segments modeled as point sources. Since the distances between the segments and the recording site is multiple orders of magnitude larger than the dimensions of the segments and electrode, these point source approximations are reasonable. For each segment source, the resistance between the source and the recoding point was determined via Eq. 3, where ε_r is the resistivity of the medium, z_j is the radial distance between the recording point and fiber, and x_j and x_i are the longitudinal positions of the recording point and segment relative to the fiber peripheral terminal, respectively:

$$R_{i,j} = \frac{\varepsilon_r}{4\pi}\sqrt{z_j^2 + (x_i - x_j)^2} \tag{3}$$

The resistive, capacitive, and ionic transmembrane currents through each segment during each time step can be calculated from the potential determined from the solution of the dynamical system described in 2.1 via equation 4:

$$I_{m,i,t} = \frac{V_{m,i,t}}{r_{m,i}} + c_{m,i} * \frac{V_{m,i,t} - V_{m,i,t-1}}{\Delta t} + I_{ion,i,t} \tag{4}$$

In equation 4, $r_{m,i}$ and $c_{m,i}$ represent the membrane resistance and capacitance of segment i, $V_{m,i,t}$ the membrane potential calculated for segment i at time t, Δt the timestep of the simulation (1 µs), and $I_{ion,i,t}$ the ionic membrane current through segment I at time t. This last term is calculated during the initial simulation as the sum of the products of the number of open channels of each type, modeled via a jump-Markov process, and single channel conductance. Finally, the SFAP at point j at timestep t is calculated by summing the potential due to each segment, point-source via equation 5:

$$SFAP_{j,t} = \sum_i I_{m,i,t} * R_{i,j} \qquad (5)$$

The eCAP at a given time step is then produced by summing the SFAPs for all fibers within the population. Artifact reduction to remove the passive transients to the stimulus was performed using a template subtraction approach, feasible in this model because the sub-threshold nature of the template can be directly confirmed for all fibers.

4.3 Results

4.3.1 Phases of the electrically-evoked compound action potential

To gain mechanistic insight into the biophysics underlying the eCAP we sought to explore the electrodynamics producing the phases of constituent eCAPs. Figure 4.2B provides trace of an SFAP produced by a single 1.5 µm fiber in response to a single cathode-first biphasic pulse with key phases of the SFAP indicated. Heat maps of the extracellular potential created by the currents through the fiber are illustrated for the corresponding phases in Figure 4.2C; the stimulating/recording electrode position is indicated 3 mm above the 10th node of the fiber. Marker and panel C1 show the fiber at rest, with only a small number of ion channels stochastically opening and closing along the fiber length. Following capacitive transients induced by the stimulating current (large spikes in B not illustrated in C), the region directly under the electrode depolarizes. This leads to the opening of voltage-gated sodium channels and, in this case, action potential initiation producing the large negative deflection typically termed the N1 peak (C2). Note that during this period there is an efflux of cations from the depolarized region of fiber while the more peripheral regions of the fiber are hyperpolarized and produce negative extracellular potentials due to local circuit currents. Saltatory conduction begins propagating the action potential both ortho- and antidromically along the fiber with re-hyperpolarization occurring in the refractory nodes, mediated principally by potassium channels and capacitive currents (C3 and C4). When the hyperpolarization induced currents in the region near the recording site becomes larger than the more distance depolarization the extracellular potential becomes positive producing the P2 peak. Ultimately, this hyperpolarization allows the sodium channels and the fiber to return to the resting state (C1).

Figure 4.2A illustrates how SFAPs, in gray, for a normally myelinated population of fibers varying only in axon caliber are combined to generate an eCAP (Fig. 4.2A). Note that some fibers do not fire an action potential and do not contribute N1 or P2 peaks to the final waveform. For activated fibers, each responds according to the dynamics described in B and C but with the details of the dynamics shifted by the intrinsic properties of the fiber. Larger, more-sensitive fibers respond faster and produce narrower N1 and P2 peaks than do small fibers. Since the eCAP response is produced by summing these different SFAPs its shape is an amalgamation of all these different features and depends strongly on the features of the underlying neural population.

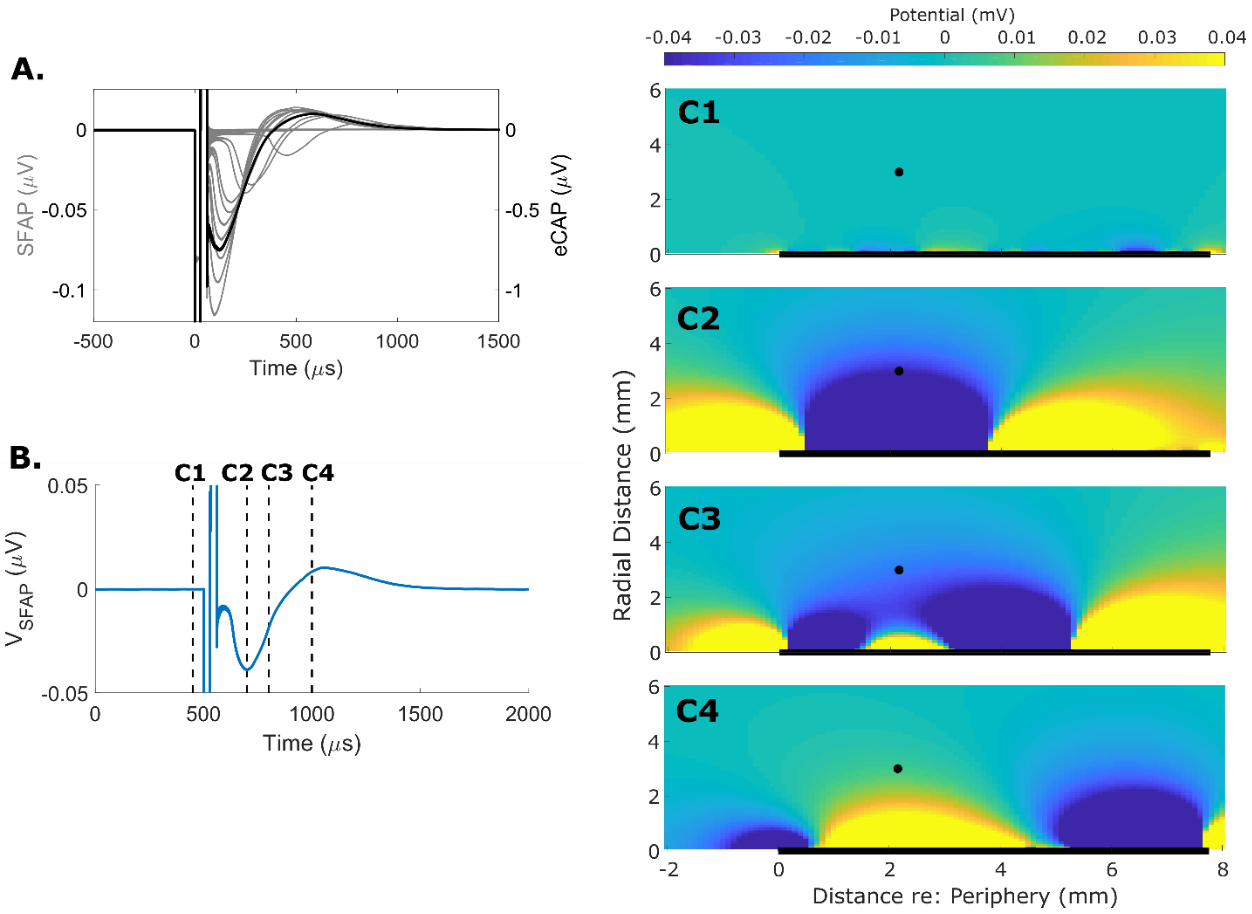

Figure 4.2. SFAP dynamics combine to produce eCAP waveform.

(A) SFAPs (gray) are summed to produce the population eCAP (black). (B) example SFAP with key phases of the fibers response labeled: equilibrium (C1), sodium current-mediated N1 peak (C2), action potential propagation (C3), and local circuit re-hyperpolarization (C4). The extracellular potential (color-mapping) during each of these phases is plotted as a function of axial distance along the fiber, abscissa, and radial distance from the fiber, ordinate, in (C).

4.3.2 eCAP morphology changes with diameter distribution shifts

We next sought to explore how incorporating pathological changes observed in SGN temporal bone microscopy studies impacted simulated eCAPs and how these changes compare with eCAPs recorded in animal models of deafness. To this end, we compared the eCAP morphologies of simulated populations with normal and shifted diameter distributions, representing diameter-dependent degeneration, to those recorded from animals with different durations of deafness. Figure 4.3 A & B reprints results from Ramekers et al.'s 2014 study in which they compared the eCAP responses of animals deafened with kanamycin/furosemide acutely, 2-weeks, and 6-weeks prior to recording (Ramekers et al., 2014). They observed marked changes in the morphology of eCAPs including a reduction in the N1-P2 amplitude difference and broader peaks at all intensities tested. Additionally, they observed less pronounced splitting of the P2 peak in the deafened cohort. Similarly, the eCAP waveforms of diameter-shifted simulated populations (Fig. 4.3 D, respectively) show markedly lower N1-P2 amplitude differences and broader peaks than those of a normally myelinated population (Fig 4.3 C).

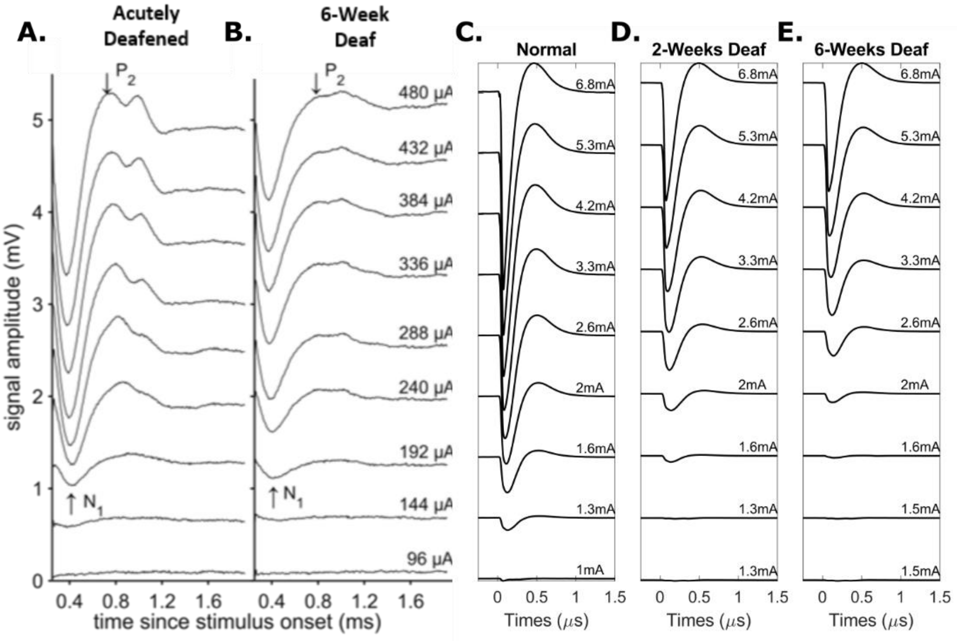

Figure 4.3. Diameter distribution shifts observes with prolonged deafness reproduce observe eCAP morphology changes.

eCAP responses recorded from acutely deafened (A) and 6-week deaf (B) Guinea pig as reported by Ramekersr et al. 2017 (reprinted with permission). Simulated eCAPs from populations with peripheral process diameter distributions matched to group distributions for normal (C), 2-week deafened (D), and 6-week deafened (E) as measured by Ramekers et al. (unpublished data). In both cases, stimuli are cathode-first biphasic pulses with 50 μs phase duration and 30 μs IPG.

4.3.3 Diameter-dependent degeneration increases sensitivity to stimulus pulse width

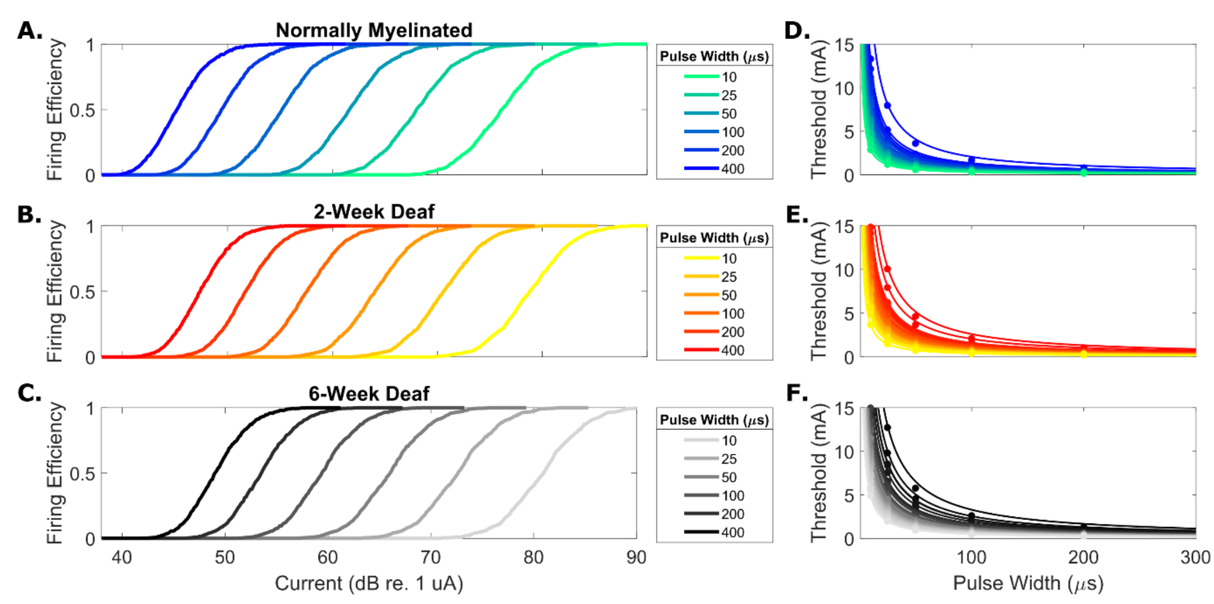

Figure 4.4. Diameter-dependent degeneration shifts thresholds but does not alter sensitivity to phase duration.

Firing efficiency growth functions in response to stimuli with six different phase durations are plotted as a function of current for populations with diameter distributions matched to those of the three groups reported on in Ramekers et al., 2014: acutely deafened (A), 2-week deafened (B), and 6-week deafened (C). (D), (E) and (F) present individual fibers' thresholds at each tested phase duration (dots) along with fitted strength-duration functions for the same populations. Color-mapping indicates fiber diameter.

The broadening of the eCAP N1 and P2 peaks with prolonged deafness and in populations with simulated diameter-dependent degeneration suggests that the temporal response properties of the neurons underlying the activity may be altered. While this cannot be directly interrogated in animal recordings, our simulated recordings provide access to the spike timing of the fibers that produce the extracellular currents. The time constants of individual fibers within each population were characterized by simulating response growth functions for cathode-first biphasic stimuli with variable phase durations, inter-phase gap was held at 8 µs for these experiments and analyzing the strength-duration curves of individual fibers. Figure 4.4 A, B, & C present the firing efficiency growth functions for simulated populations with diameter distributions matched to those measured in acutely deafened, 2-week deaf, and 6-week deaf animals by Ramekers et al. at variable phase durations. For all three populations, growth function threshold decreases, and slope increases as phase duration increases, however, diameter-dependent degeneration leads to increases in threshold with all phase durations. This can also be appreciated by considering the strength-duration curves for the individual fibers for these populations (Fig. 4.4 D, E, & F). From the strength-duration curves, the chronaxie and rheobase for each fiber can be determined. Figure 4.5 presents the distributions of rheobase (A) and chronaxie (B) for each fiber in the three different populations. Populations with diameter-dependent degeneration exhibit modestly elevated rheobase mean and variance. While mean fiber chronaxie across the populations with simulated pathology is significantly elevated and the inter-fiber chronaxie variance decreases.

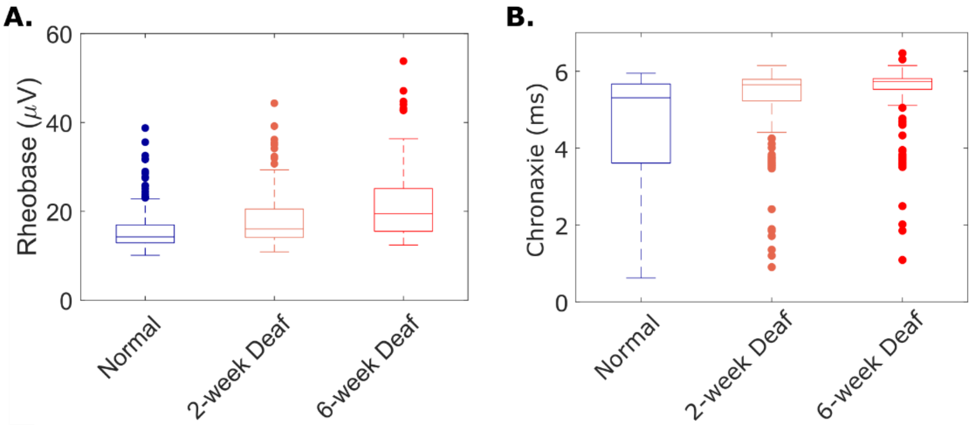

Figure 4.5. Diameter-dependent degeneration elevates mean rheobase and chronaxie.

Estimated rheobase (A) and chronaxie (B) distributions from fitted strength-duration functions for 3 different simulated neural populations: normal (blue), 2-week deaf (orange) and 6-week deaf (bright red).

4.3.4 Diameter-dependent degeneration abolishes relative amplitude/duration preference

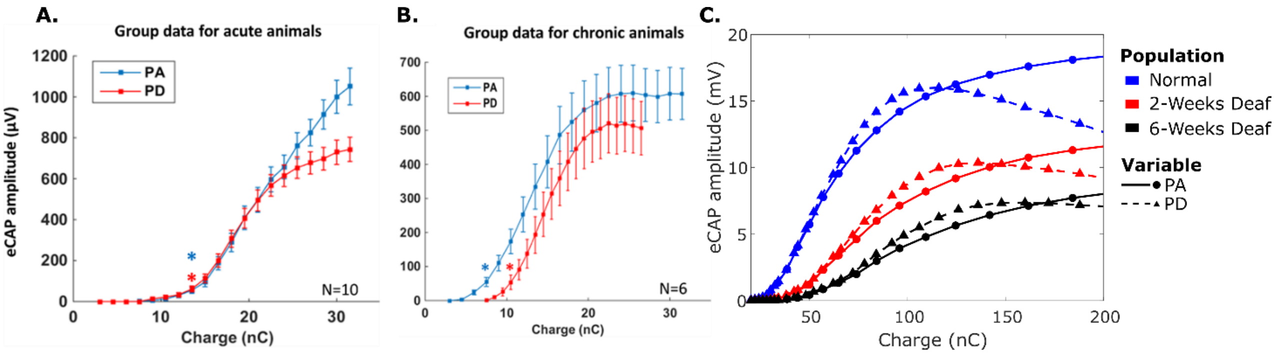

Figure 4.6. Diameter-dependent degeneration reduces relative phase amplitude-duration sensitivity difference.

Group eCAP AGFs for acutely (A) and chronically (B) implanted Guinea Pigs, recorded by Adenis et al., plotted as a function of total single-phase charge (reprinted with permission). Current was incremented either by increasing phase amplitude (PA, blue) or duration (PD, red). (C) presents simulated eCAP AGFs for 3 different populations: acutely deafened (blue), 2-week deaf (red), and 6-week deaf (black). Current incremented by phase amplitude (solid lines and filled circles) or duration (dashed lines and filled triangles).

To explore the impact of these changes in time constants on eCAP AGFs, we replicated the phase amplitude (PA) versus phase duration (PD) AGF comparison performed by Adenis et al. (Adenis et al., 2018). In this experiment, acutely and chronically implanted guinea pigs were stimulated by stimuli with charge incremented by either increasing PA or PD. In the group mean data for acutely implanted animals (Fig 4.6A), with low delivered charge the PA and PD-based AGFs look remarkably similar while with large charge quantities the PA induced N1-P2 amplitudes are significantly larger. The simulated normally myelinated population eCAP AGFs (Fig. 4.6 C, blue curves) reproduce key features of this acute animal group data with little difference between the amplitude of the PA and PD responses at low current delivered but an amplitude difference between the two at high current quantities.

This effect is much less prominent in the chronically deafened animal group data (Fig 4.6B), however, Adenis et al. observed huge inter-animal variance for this group. Additionally, at the group level they observed a significant threshold difference between PA and PD based stimuli for this chronically implanted cohort. While diameter-dependent degeneration failed to (Fig. 4.6 C) recapitulate the threshold difference between PA and PD-based growth functions observed, they do provide insight into the reduced high current PA-PD gap. Diameter-dependent degeneration (red and black curves) produces a dose dependent reduction in amplitudes for both PA and PD-based responses and preferential sensitivity for PA-based stimuli

Interrogation of the spiking behavior of the fibers within the simulated populations suggests these changes can be explained by the interaction between variability in fiber response latencies and time constants. In healthy fibers, the high-PA stimuli recruit all fibers within the brief window of the pulse leading to relatively small variance in response latencies while the high-PD stimuli recruit the most sensitive fibers early but the least sensitive fibers later. This variability in response timing leads to smaller eCAP peaks despite unchanged recruitment (data not shown). In the degenerated populations, the larger and less variable time constants of the fibers make them comparatively more sensitive to long-PD stimuli and more synchronous. This effect mitigates the latency variance effect produced by long pulse widths and leads to relatively higher PD-based amplitudes.

4.3.5 Diameter-dependent degeneration decreases sensitivity to stimulus inter-phase gap

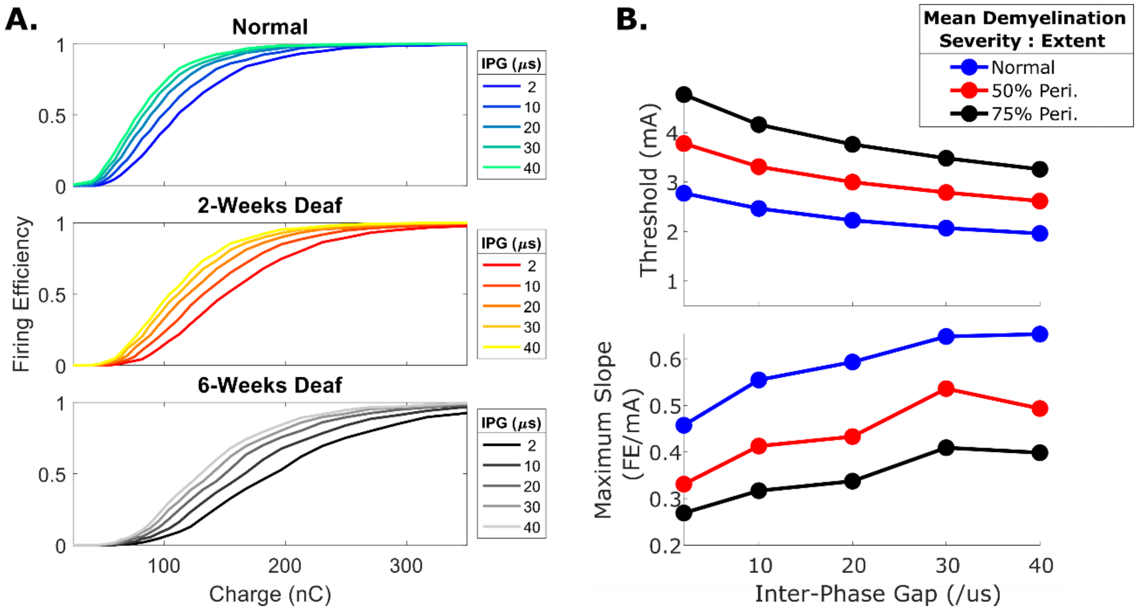

Figure 4.7. Diameter-dependent degeneration reduces impact of inter-phase gap on firing efficiency slope.

Firing efficiency growth functions in response to stimuli with six different IPGs are plotted as a function of charge delivered (A) for three populations with different simulated diameter distributions: 'normal', '2-week deaf', and '6-week deaf'. Coloring indicates stimulus inter-phase gap. Asymptotic firing efficiency (C) and maximum slope (D) are plotted as a function of IPG for these three populations: 'normal' (blue), '2-week deaf' (red), and '6-week deaf' (black).

To continue exploring the impacts time constants on sensitivity to key CI stimulus features, we next simulated the firing efficiency growth functions in response to stimuli varying in IPG. Figure 4.5 A & B presents the firing efficiency growth functions for populations with normal and shifted diameter distributions. Across all IPGs the diameter-dependent degeneration produces elevated thresholds and reduced maximum growth function slopes. These threshold and maximum slope shifts are quantified as a function of IPG in panels C and D. Populations with shifted diameter distributions exhibit a pronounced reduction in threshold (particularly at low IPGs), reduced slopes at all IPGs, and a smaller change in slope between low and high IPGs.

4.3.6 Diameter-dependent degeneration-induced increases in fiber time constants replicate eCAP 'IPG-effect'

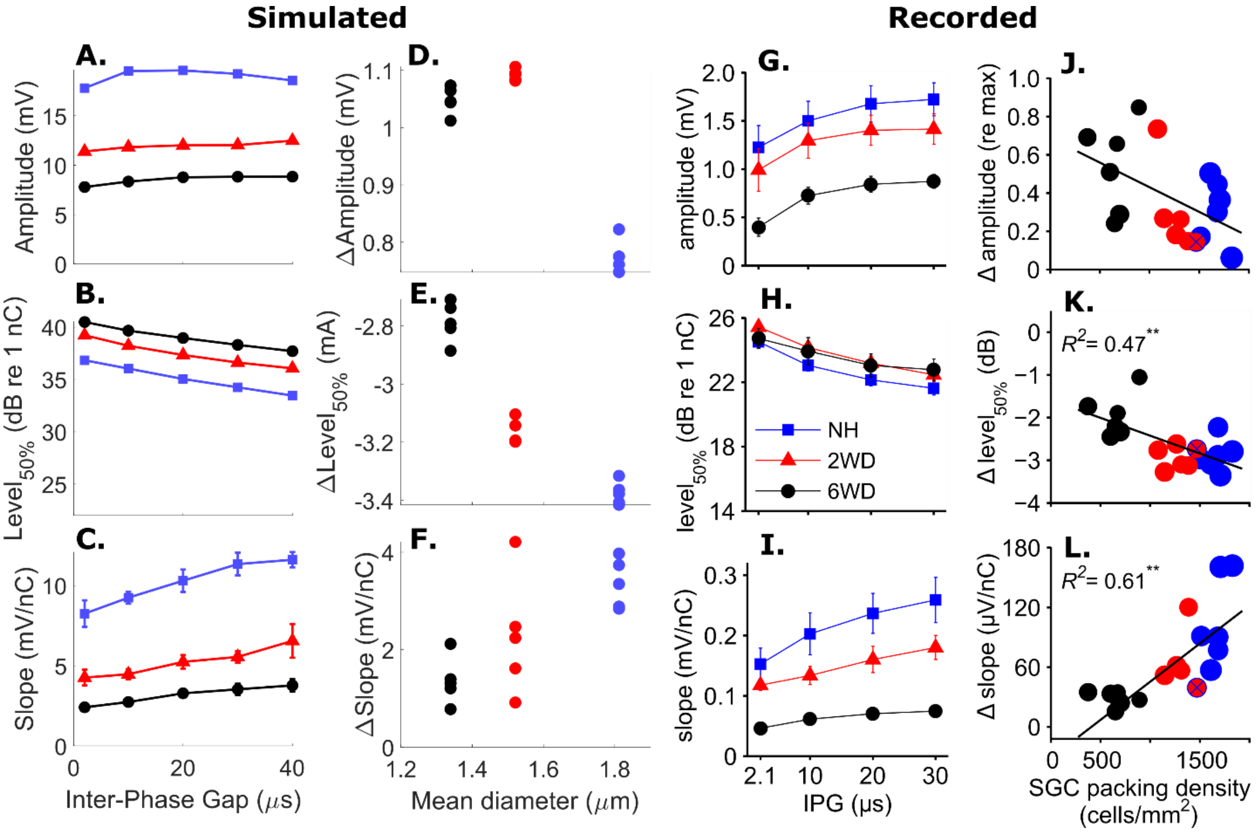

Figure 4.8. Diameter-dependent degeneration reproduces the eCAP 'IPG effect' observed by Ramekers et al.

eCAP AGF asymptotic amplitude (A and G), level at 50% asymptotic amplitude (B and H), and maximum slope (C and I) are plotted as a function of IPG for simulated populations with diameter-dependent degeneration (A-C) and Guinea Pigs with three different durations of deafness (G-I) as reported in Ramekers et al., 2014 (reprinted with permission). The difference between asymptotic amplitudes (D and J), level at 50% asymptotic amplitude (E and K), and maximum slope (F and L) between each populations responses to 30 and 2 μs is plotted as a function of mean fiber diameter for simulated populations (D-F) and spiral ganglion cell (SGC) packing density for Guinea Pigs (J-L). In all panels, simulated and recorded values for acutely deafened (NH), 2-week deafened (2WD), and 6-week deafened (6WD) are represented by blue squares, red triangles, and black circles, respectively.

Ramekers et al. explored the impact of IPG on eCAP AGFs for animals with three different durations of deafness prior to recording: acute, 2 weeks, and 6 weeks (Ramekers et al., 2014). They observed significant changes in both the morphology of the eCAPs, described previously, and growth function shapes for these three cohorts. Peak amplitude and maximum slope increased while current level needed to produce 50% of asymptotic amplitude decreased with increasing IPG for all populations. Peak amplitudes (4.8 G) and maximum slopes (4.8 I) were significantly lower across all IPGs for long-term deafened groups while there was a relatively minor change in current level at 50% asymptotic amplitude (4.8 H). Most notably, however, the effect of IPG on current level at 50% asymptotic amplitude (4.8 K) and slope (4.8 L), defined here as the difference between the quantities with stimuli with 30 and 2 μs IPG, was lower in magnitude for the long-term deafened animals and correlated with the spiral ganglion neuron counts, a phenomenon termed the 'IPG effect'. Spiral ganglion neuron counts were inversely related to the effect of IPG on asymptotic response amplitude (4.8 J) but this effect was not significant.

eCAP growth functions for simulated populations exhibited qualitatively similar effects of IPG on growth function asymptotic amplitude, current level at 50% of asymptotic amplitude, and maximum slope (Fig. 4.8 A, B, & C, respectively). Additionally, the diameter distribution shift used to simulate diameter-dependent degeneration reduced asymptotic amplitude and maximum slope and increased threshold, consistent with the patterns observed in the 2-week and 6-week deafened animal groups. The differences in asymptotic amplitude, current level at 50% asymptotic amplitude, and maximum slope between stimuli possessing 30 and 2 μs IPG are plotted as a function of mean fiber diameter (Fig 4.8 D, E, & F, respectively). Level at 50% asymptotic amplitude monotonically decreases while maximum slope monotonically increases with mean fiber diameter. In contrast, asymptotic amplitude shows a less consistent, non-monotonic pattern.

4.4 Discussion

The simulation approach presented enables simulation of eCAPs recapitulating many of the key morphological features of experimental ones including the size and width of the N1 and P2 peaks. Importantly, the biophysical detail underlying the simulation enables exploration of the mechanistic sources of eCAP variability. Additionally, it allows for simultaneous simulation of the extracellular potentials generated by the fiber populations and access to the spiking activity of the fibers within the population producing this activity. Simulated population exhibited similar eCAP morphology and growth function shape changes as occurs in long-term deafened animals.

The pulse duration study of populations with reduced diameter distribution mean and variance indicates fibers in such populations generally have larger and more variable rheobases, corresponding to threshold with long phase durations, and higher and more consistent chronaxie, representing prolonged and more consistent of fiber time constants. These changes in individual fiber properties produce a more dramatic impact of PD on the firing efficiency growth function slope and threshold of the altered populations where they exhibit relatively greater sensitivity to long over short pulses than do the normal populations. This change in spiking behavior shed light on the PA vs. PD AGF results observed by Adenis et al. in acutely and chronically implanted animals (Adenis et al., 2018). In normal populations, both the PA and PD-based charge increments recruit fibers nearly equally well but at long PDs the temporal variability in the fibers' responses reduces eCAP amplitudes. In contrast, the long-time constants of the fiber populations constructed to match the long-term deafened animals make them relatively more sensitive to long PD stimuli reducing or even inverting the eCAP AGF gap at high current densities. It is important to note that Adenis et al. observed huge amounts of individual variability in the shapes of the PA and PD functions that cannot be fully explained by the effects explored here. Notably, while the effects observed due to diameter distribution shifts can explain the shift in relative sensitivity at high current delivery, they do not account for the threshold differences Adenis et al. observed. Nevertheless, the reduction in PA preference at large delivered currents observed in some animals and our diameter-dependent degeneration model suggests a mechanism for improved recruitment in some individuals with variable PD CI stimulation strategies. In contrast to the increased sensitivity to phase duration noted, we observed a reduced impact of IPG on firing efficiency growth function slopes in the diameter distribution shifted populations. In normal fibers, longer IPGs likely reduce the interfering effects of the opposing pulse polarities. Our hypothesis is that the longer time constants of the smaller fibers mitigate the release from masking produced by the longer IPGs because the fibers' membranes are slower to charge and discharge. This effect extends to simulations of the eCAP AGF slope change with IPG producing a result consistent with that observed in chronically deafened guinea pigs by Ramekers et al. (Ramekers et al., 2014).

While the presented modeling results with simulated degeneration provide useful mechanistic insights into how pathology may alter eCAPs, the simplicity and uncertainty within the model leave many remaining questions. Except for the terminal expansion and internode/node dichotomy, the present model treats the nerve fibers as symmetrical along their length. This is gross simplification as SGN peripheral axons tend to be significantly smaller in both diameter and length than do their central processes (M. Charles Liberman and Oliver, 1984). Additionally, the cell body clearly introduces a substantial impendence load, even if perfectly myelinated (Rattay et al., 2001b, 2001a). Unfortunately, implementing an explicit soma into biophysical model of SGNs is difficult because the electrodynamics governing spike propagation through them are poorly understood. Nevertheless, introducing these inhomogeneities into the fiber structure and exploring how they impact eCAP features is an important next step.

The present model also utilizes an extremely simplified cochlear electrical structure, treating the region between stimulating electrode and fibers as homogenous and isoresistive. Electrical current presented by CIs must travel through endolymph, epithelial tissue, and multiple layers of complex interstitial tissue (including some bone) before reaching SGNs. Other biophysical models of CI stimulation have implemented more complex electrical structures of the cochlea ranging from two-compartment models (Joshua H Goldwyn et al., 2010) to complex boundary-element models reconstructed from micro-computed tomography imaging (Briaire and Frijns, 2000b, 2000a; Frijns et al., 2000; Hanekom and Hanekom, 2016; Kalkman et al., 2016; Malherbe et al., 2015). These simulations provide evidence that changing the electrical structure of the simulated cochlea significantly alters model behavior, particularly regarding how current activates different regions of the cochlea. We elected to use a simplified model because the difficulty of measuring the electrical properties of intact cochlea makes these more complex models poorly constrained and our focus was on the effect of intrinsic property differences between nearby fibers rather than across different regions of the cochlea. Extending this work to explore recruitment of fibers across broader regions of the cochlea using different electrical models will be an important future direction.

Lastly, this work only considers degeneration as possible sources of SGN functional pathology because it was directly observed in Ramekers et al. animal cohort. Other pathological aberrations have been observed in temporal bone studies of humans and long-term deafened animals, including vacuole formation between plasma membrane and myelin (El-Badry et al., 2007; Leake et al., 1991), and fibrosis within different cochlear compartments (Wilk et al., 2016). detailed exploration of the effects of these changes on simulated eCAPs is of great interest but beyond the scope of this work.

Chapter 5- Conclusions and Future Directions

5.1 Discussion of findings

One of the principle challenges in the field of cochlear implants is that fundamental biophysical details underlying how the electrical current presented into the cochlea activates SGNs remain poorly understood. Unsurprisingly given this unexplained detail, there exists a substantial amount of variability in CI outcomes that cannot be accounted for. The presented modeling work outlines a strategy for incorporating pathological changes observed in electron microscopy temporal bone studies into biophysical simulations of cochlear implant simulation of auditory nerve fibers and then assessing the impact of such changes on simulated functional outcomes. In this work we focused our efforts on a single pathological feature, myelin loss, and three different simulated outcomes: single fiber of electrophysiological properties determined via juxtacellular recordings, intracochlearly recorded compound action potentials, and ITD detection. Ultimately, we hope this work lays the foundation for exploring additional types of SGN pathology and additional outcomes while providing insight into key knowledge gaps that suggest needed experiments.

We first explored the parameter space of demyelination severity and extent in a single fiber simulation, exploring the impact of this demyelination of single unit responses, and comparing these results to findings from single-unit recordings of ANFs in the cat. We began by considering the spatial details of fiber excitation in normally myelinated fibers. In such fibers the opposing polarities of cathodic and anodic stimuli produce antisymmetric patterns of depolarization/hyperpolarization. With cathodic current the region directly under the electrode is depolarized while the adjacent fiber segments are weakly hyperpolarized, and vice-versa for anodic current. As such, cathodic current initiates action potential directly under the fiber while anodic current-induced responses require substantially higher current levels and begin more centrally. This produces both a threshold and latency difference for monophasic stimuli of opposing polarities. With biphasic stimuli, fibers' responses are initially driven by the cathodic phase of stimuli, however, at sufficiently high currents the central anodic initiation dominates the response. This change in initiating polarity for biphasic pulses with increasing stimulus intensity produces latency changes that depend on pulse polarity order. At stimulus intensities within this transition region fiber response latency distributions become bimodal due to stochastic contribution of initiation by both polarities. These results demonstrate that, even in a highly simplified system, the intrinsic properties of neurons shape how they respond to applied current in functionally impactful ways.

When the fiber in these single-unit studies was modified to simulate demyelination, these spatial and temporal dynamics of spiking responses became even more striking. We observe substantial non-monotonicities in latency with increasing demyelination. With some myelination states the poor insulation produced by both initiation and conduction delays. While in others, loss of myelin peripherally shifted the site of action potential initiation more centrally resulting in a substantial reduction in latency. As such, latency of individual fibers could be either dramatically increased or decreased by alterations in myelination. Concomitant with these changes in latency, most fibers exhibited relatively little change in jitter, however, some exhibited very high jitter due to multiple initiation sites. Importantly, these timing changes occurred at degrees of demyelination that produced only relatively modest increases in threshold suggesting that deficits in myelination can alter fiber functional properties in the absence of soma degradation. These findings shed some light on sources of variability driving conflicting findings in single-unit recordings from deafened animals.

Current presented by a single electrode activates many SGNs distributed over a substantial length of cochlea, however, no procedure to simultaneously record the spiking of multiple primary auditory neurons simultaneously has been developed. We leveraged a biophysical modeling approach to explore how the intrinsic size and myelination state variability across the SGN population would be anticipated to produce graded recruitment and inter-fiber latency variability. Even within a population with g-ratios matched to that measured in acutely deafened animals (mice), diameter and myelination heterogeneity produces a population dynamic range that is much larger than that of individual fibers and asynchronous responses between fibers. Increasing the mean of the population g-ratio distribution produces a reduction in firing efficiency growth function slope and asymptotic probability that scales non-linearly with mean g-ratio. The net result is an increase in dynamic range from that of a normal population but with fewer fibers encoding this range, necessarily producing fewer discernible steps in the FE growth function.

When first recruited an individual fiber exhibits relatively high response latency and jitter, however, as the stimulus intensity becomes significantly suprathreshold for a fiber the responses that fiber contributes to the population response become lower latency and more consistent. The net result of this dynamic is level-dependent variability in population response latency distributions that depend on the breadth of intrinsic properties present across the population. Even in the populations with normal g-ratio distribution means, this effect leads to substantially greater inter-fiber latency variance than within fiber jitter. This disparity between single-unit and population variance provides a potential mechanistic explanation for why while single-unit responses to low-pulse rate electrical stimulation are tightly phase locked, central jitter and psychophysical detection of fine temporal structure is poorer than in acoustic hearing. Indeed, our simulations of ITD detection in normal populations suggest that this peripheral noise due to intrinsic property variance likely limits encoding of ITDs. In demyelinated populations, even though the g-ratio variance was not varied, the spread of population response latencies was particularly dramatic compared to the normal population but, importantly, without a significant increase in mean jitter. As such, this effect would be anticipated to be difficult to detect at the single-unit level, particularly without tight control of relative site of stimulation between fibers. This elevated simulated inter-fiber latency, in conjunction with a reduced number of looks did lead to elevated ITD JNDs sufficient to account for much of the variability observed between CI users.

Increased g-ratio distribution mean yielded an increase in mean fiber chronaxie and between-fiber variance in chronaxie, while rheobase was relatively preserved. This effect led to functionally important changes in sensitivity to biphasic stimulus phase duration and inter-phase gap. Poorly myelinated populations exhibited elevated sensitivity to stimulus phase duration due to the slowed charging of their membranes. Similarly, slowed discharging interfered with the release from masking normally yielded by an IPG increase.

Extending our biophysical model to enable simulated recording of eCAPs provides a tool in which the behavior of eCAPS can be explored in a setting where the biophysical details of the component neurons may be perturbed, and their spiking monitored. This permits analysis of how neuron properties alter their spike response and ultimately change eCAP morphologies and growth function behavior. We leveraged this tool to prove the mechanisms underlying eCAP AGF characterization studies performed in animals with variable durations of deafness and implantation. Both our normally myelinated population and animals acutely implanted exhibited greater AGF slopes with PA than PD increments at high levels of total charge delivered (Adenis et al., 2018). Demyelination produced a reduction and, ultimately, inversion of this relative PA/PD able to explain much of the enormous between-animal variability in relative PA/PD sensitivity observed in chronically implanted animals, though it could not account for within animal differences in PA and PD-based thresholds. Analysis of the spiking data underlying these eCAPs suggests this change in PA/PD sensitivity is due to a combination of two effects. Long pulses produce greater variability in spike latency than do shorter ones with the most sensitive fibers activated early and the least sensitive late. This leads to broadening of the eCAP peaks and a reduction in N1-P2 for these long PD stimuli even in the absence of differences in recruitment. In demyelinated populations, this effect is conflict with the ability of long PD stimuli to more effectively recruit the fibers with elevated time constants. Analysis of eCAP AGFs for normally and demyelinated populations in response to stimuli with variable IPGs provides an insight into the mechanism underlying the 'IPG effect' observed by Ramekers et al. (Ramekers et al., 2014). In healthy fiber populations, a longer IPG provides greater release from inter-polarity interference resulting in steeper AGFs; this effect is particularly pronounced for IPGs up to ~50 µs. The time constants of demyelinated fibers are so long that they exhibit much less release form interference with these small increases in IPG and, therefore, their AGFs exhibit a reduced change in slope with IPG. In addition to providing insight into the biophysics underlying variability in eCAP responses these simulation findings highlight how fiber physiology places fundamental constraints on the feasibility of modifying recruitment by altering stimulus waveforms in some pathological states.

In short, here we have presented a computational strategy for connecting results across different model systems and levels of the auditory system with the goal of generating insights into the principal mechanisms of CI function. We demonstrate that a simple perturbation, demyelination, into a relatively uncomplicated model of electrical stimulation can reproduce several key experimental results though fails to replicate some critical observations. While there are clear opportunities for extending the computational approach taken, we believe that this general paradigm of using modeling to connect findings across different levels is likely to help elucidate key principles of the electrode-neuron interface.

5.2 Limitations and opportunities

One critical question is how prevalent demyelination actually is in human CI users. While significant myelin loss has been reported in post-mortem human (Leake and Hradek, 1988) and mouse (Wan and Corfas, 2017) temporal bone studies, it has generally not been reported in Guinea pigs (Kroon et al., 2017); one caveat regarding this difference is that studies in Guinea pigs typically utilize aminoglycoside-mediated deafening while the studies that observed myelin loss utilized auditory over-exposure. Given this conflicting evidence some share a sentiment that myelin loss may be a transient state that immediately precedes degeneration. Ultimately, answering this question definitively will require careful time-course analysis of SGNs following controlled deafening and will need to be repeated for multiple deafening strategies.

Other structural deficits have been observed in temporal bone studies from deafened humans and animals. Degeneration of neurons has been a consistent finding (Kroon et al., 2017; Landry et al., 2011). Synaptopathy following auditory over-exposure preferentially affects small-caliber, high-threshold, low spontaneous rate fibers (Furman et al., 2013), and unpublished work from the Ramekers group suggests this asymmetry may exist at the level of peripheral process loss too. Exploring the impact of such diameter-dependent degeneration on model performance using strategies similar to that presented in Chapters 3 and 4 is a compelling future direction for this modeling work.

Going forward, one major direction will be to simulate additional, and more complex, tasks and compare model performance to human psychophysics data. This effort will present significant challenges, both requiring extension of the biophysical model and advanced methods for analyzing the information contained in spike trains. In this work, we focused on responses to single pulses and pulse trains of sufficiently low rate that the cycle to cycle responses were largely independent. Longer stimuli, like those required for any language or spectral task, will require models incorporating adaptation and facilitation (Boulet et al., 2016), however, the precise biophysical details underlying these slow temporal dependencies in SGNs are not well characterized (Boulet and Bruce, 2017b; Negm and Bruce, 2014). Negm and Bruce demonstrated that adding HCN and KLT channels to the soma of simulated fibers can reproduce these delayed temporal effects, but more experimental work will be required to ascertain if these ion channels truly drive these phenomena. Including additional compartment asymmetry into each model fiber, including cell body and variability in peripheral/central axon diameter differences, is also likely necessary for simulating these effects, however, how action potentials propagate across the high impedance load of the soma, particularly the unmyelinated human soma, is unknown (Rattay et al., 2001b). In any case, these cellular substructures would be anticipated to increasing the change in latency between responses induced by cathodic and anodic phases of stimulus, like those explored in Chapter 2.

In addition to possessing differences in intrinsic properties, SGNs within the cochlea exhibit complex spatial organizations. The peripheral processes of these bipolar cells synapse in the organ of Corti within different tonotopic regions of the cochlea and their soma exist within the adjacent region of Rosenthal’s canal. Their central processes then extend into the modiolus, joining the processes of other SGNs to become the cochlear nerve. Accurately modeling this complex spatial organization will require, in addition to implementation of neural sub-compartments, simulation of the complex electrical structure of the cochlea and how current presented through multi-channel electrode arrays interact with it. While a number of groups have created intricate electrical models of the cochlea that accurately simulate its three dimensional structure (Briaire and Frijns, 2000a; Frijns et al., 2001; Hanekom and Hanekom, 2016), it is extremely difficult to know how accurately these models replicate the electrodynamics of the cochlea. This challenge is largely due to the difficulty in characterizing the electrical properties of the intact cochlea, particularly in humans. Progress on this front will likely require advances in empirical techniques for measuring the impedances created by the anatomy of the cochlea.

Appendix 1: Design of psychophysical tasks for assessing human spectro-temporal resolution

In preparation for submission to the Journal of the Acoustical Society of America as ‘Spectral Aliasing in a Spectral Ripple Discrimination Task’. Co-authored by: Anisha R. Noble, MD, MS; Jay T. Rubinstein, MD, PhD; David L. Horn, MD, MS

A1.1 Abstract

Tests of spectral ripple discrimination SRD are widely used to test spectral resolution in cochlear-implanted individuals and have been shown to correlate well with measures of speech identification and discrimination. Additionally, SRD tests have been used to examine development of spectral resolution in normal hearing listeners. Previous work has found that adults with intact acoustic hearing have SRD upper limits around 8-11 ripples per octave (RPO) across various methodologies including phase inversion detection, ripple detection, and density discrimination. These tasks generally use a multiple sine-wave carrier rippled in intensity across frequency. The carrier density used has varied from approximately 30/octave to about 400/octave. Recently, we encountered a non-monotonicity when adapting an SRD task with a 30/octave carrier, the spectro-temporal modulation ripple test, for use with infants. Some subjects were able to distinguish 16 RPO from 20 RPO but failed to do so at lower ripple densities. It was hypothesized that an interaction between the carrier and ripple densities produced “spectral aliasing” when the ripple density was within a few Hz of the carrier density, akin to the Nyquist frequency limit. The present study was designed to test this hypothesis by examining the effect of carrier rate and stimulus duration on SRD.

Participants were 5 normal hearing adults (mean age 31 years old) naïve to the task who participated in a single 2-hour test visit. Stimuli were generated as described by Aronoff and Landsberger with alterations to enable modification of carrier density and stimulus length (Aronoff and Landsberger, 2013). Phase-randomized sinusoidal carriers were spectro-temporally amplitude modulated with a time-variant full wave rectified sinusoid with ripple depth of 20dB, 100ms on/offset ramps, and 5Hz sweep rate. Spectral ripple density varied from 1 to 20 RPO in ¼ $\log_2$ steps. A single-interval yes/no procedure was used with feedback in which the listener raised their hand when a trial contained a ripple density < 20 RPO. In between trials, the listener heard repeating 20 RPO stimuli at 0.5s ISI. Stimuli were presented at 70dB SPL in sound field. Ripple density and starting phase was varied randomly across trials. Each subject was tested in 4 conditions in random order with two within-subject variables: carrier density (33/octave or 100/octave) and stimulus duration (1s or 0.5s).

The effects of ripple density, carrier rate, and stimulus duration on mean proportion correct were examined with a full-factorial linear mixed effects model. Significant main effects of density (negative effect), carrier rate (positive effect), and stimulus duration (positive effect) were found. The only significant interaction was between carrier rate and ripple density. Post-hoc comparisons revealed a non-monotonicity at 16 RPO for the 33/octave carrier but not the 100/octave carrier. If this monotonicity was ignored, the threshold at the 70% point of the psychometric function was approximately 11-12 RPO for the 33/octave carrier but 16-17 RPO for the 100/octave carrier.

This experiment confirms that spectral aliasing limits spectral peak representation of the stimulus and creates a non-spectral beating cue at an RPO ½ of the carrier rate. This will create a ceiling effect when the low carrier rate is used to probe spectral resolution in NH listeners or in CI users who have relatively good spectral resolution (such as bimodal or hybrid listeners). Although using a higher carrier rate can overcome this problem, it should be noted that the task becomes one of probing ripple discrimination rather than ripple detection. It is likely that the upper limit for spectral peak resolution, in normal hearing listeners, is higher than the 20 RPO referent used in the present study.

A1.2 Introduction

The spectral-temporally modulated ripple (SMR) test asks listeners to discriminate between signals consisting of sinusoidal carriers modulated in both the frequency and time domains (Aronoff and Landsberger, 2013). Typically, the time domain modulation frequency is held constant, and subjects are asked to make judgements based on the 'ripple density' the periodic modulation in the frequency domain. As such, this task is designed as a method for probing listeners' spectral resolution in the context of temporal modulation. Performance in this task has previously been shown to correlate well with speech measures in cochlear implant (CI) listeners (DiNino and Arenberg, 2018; Holden et al., 2016; Lawler et al., 2017; Zhou, 2017).

Previous work has found that adults with intact acoustic hearing have spectral ripple density discrimination upper limits around ~11-12 ripples per octave (RPO), with a comparison stimulus of 20 RPOs and the use of 33.33 carrier sine waves per octave to generate the stimuli. We sought to adapt this task to test infants and children to explore the time course of spectral resolution development in both normal hearing and cochlear implanted listeners. We created a version of the task with longer stimuli and larger ripple per octave step sizes to facilitate expedient observer-based testing of young subjects. While pursuing this work, we began observing an interesting non-monotonicity in which some subjects passed when asked to distinguish 16 from 20 RPOs but then failed when dropped down to 13.75 RPOs. This observed non-monotonicity prompted us to explore the stimulus creation strategy in greater depth. We found that interaction between the carrier and ripple densities produces 'spectral aliasing' when the ripple density is within a few hertz of half the carrier density, akin to the Nyquist frequency limit introduced by discrete time series data. With the 33.33 carriers/octave density utilized previously, this leads to prominent beating near 16.666 RPOs that remains significant at both 10 and 20 dB ripple depths. In this letter, we show that this spectral beating introduces an unintended queue that may yield aberrantly poor ripple detection thresholds. By utilizing a higher carrier density, normal hearing listeners discrimination thresholds improves by ~5 RPOs with the same 20 RPO reference stimulus. These data demonstrate the importance of ensuring that the carrier density is sufficiently high to avoid the introduction of unintended artifacts by the discrete time series stimulus generation approach taken.

A1.3 Methods

Participants: Five normal hearing adults were recruited from a University of Washington subject pool for communication and hearing related studies. The inclusion criteria for these participants were: native speaker of American English, no history of ear disease or hearing loss and normal audiometric screening on day of experiment. The mean age of the cohort was 31 years old. Participants were paid $15 per hour for their participation in the study. Data collection for each participant was completed in a single 2-hour test visit.

Stimuli: SMRT stimuli were generated as described by Aronoff and Landsberger with alterations to enable modification of carrier density and stimulus length (Aronoff and Landsberger, 2013). Briefly, phase-randomized sinusoidal carriers, *P(i,t)*, were produced according to Eq. 1:

$$C(i,t) = \frac{\sin(2*\pi*(f(i)*t+U(0,1))}{\sqrt{n_i}} \qquad (1)$$

Where n_i symbolizes the number of carriers, i carrier index, $f(i)$ carrier frequency, and $U(0,1)$ a random number drawn from a uniform distribution within the interval (0,1). Carrier frequencies were uniformly spaced within the logarithmic frequency interval 100 to 6500 *Hz* at the selected carrier densities ($C_{density}$). Each carrier's amplitudes were spectro-temporally modulated with a time-variant full wave rectified sinusoid according to Eq. 2:

$$AM(i,t) = R_{depth} * \left|\sin\left(\left(\frac{i*R_{density}*pi}{C_{density}}\right) + (R_{rate} * pi * t) + \Phi\right)\right| \qquad (2)$$

Where R_{depth} symbolizes ripple depth in dB (20 dB in these experiments), $R_{density}$ ripple density in RPO, R_{rate} temporal ripple modulation rate in Hz, and Φ the ripple phase. Onset and offset ramps, 100 ms each, were applied to the modulated stimuli.

Psychophysical Task: Participants SMR discrimination was tested using an observer-based psychoacoustic procedure designed to facilitate infant testing previously used by Horn et al. (Horn et al., 2017; Jia et al., 2012). This observer-based approach was selected to be comparable with infant testing going forward. Testing was conducted in a single-walled sound booth facing a loudspeaker 1.6 m away at 0 azimuth. Listeners sat alone in the test booth and were instructed to raise their hand when they "heard the different sound that activates the toy." Stimuli were produced via the loudspeaker at 70 dB SPL at a presentation frequency of 0.5 Hz. An observer sat outside the test booth and observed the participant's behavior through a glass window. Stimulus loudness was calibrated before each visit. Participants were presented with a repeating stream of background 'standard' stimuli and were blind to trial initiation. The observer-initiated trials intermittently when the participant was quiet, prepared, and facing forward to control for anticipation and attention effects. Trial type, "change" or "no-change," was determined randomly without the observer's knowledge. To the listener, 'no-change' trials were indistinguishable from the background standard stimuli. Trial presentation began the next full stimulus period after initiation and was followed by a 4-second response window. During this window, the observer marked whether the participant indicated a change had occurred with a keyboard button press. Observer-based response categorization was based solely on the listener's indication with a raised hand. Participants' were reinforced for each correct identification of a 'change' trial by a 4-second activation of a video clip.

For each condition, the task began with an initial training phase, designed to produce association between 'change' trials and the reinforcer, followed by a testing phase. During training, the ripple density was fixed at 4 RPO and 75% of trials were change trials. Trial type varied pseudo-randomly with six change and two no-change trials in each block of eight trials. As the training phases were intended to produce an association between the 'change' stimulus and the reinforcer, listeners were reinforced after each change trial regardless of the observer classification. Training ended when the observer reached a criterion of >80% hit rate and >80% correct rejection rate over 5 consecutive change and no- change trials, respectively. All subjects passed the training phase within one block of eight trials for all conditions. Testing differed from training in 3 key respects: First, ripple density of change trials varied pseudo-randomly within each condition with eight total presentations for each RPO, 2-each with phases of 0, $\pi/2$, π, and $3\pi/2$. Second, change and no-change trials were presented pseudo-randomly with a frequency of 4:1. Finally, listeners were reinforced only on change trials on which the observer indicated a signal.

Each participant completed a block for four different conditions, consisting of stimulus durations of either 0.5 s or 1 s at carrier densities of both 33.333 and 100 carriers per octave. Condition order was randomized between subjects and subjects were blind to this order. For each condition, 'standard' stimuli were 20 RPO and produced using the outlined condition strategy. For the 33.333 carrier/octave conditions, SMRs at ripple densities of 5.657, 8, 9.514, 11.314, 13.454, 16, and 19.027

RPO were presented. For the 100 carrier/octave conditions, 16.708, 17.448, and 18.221 RPO stimuli were also selected to enable more closer approximation of thresholds.

A1.4 Results

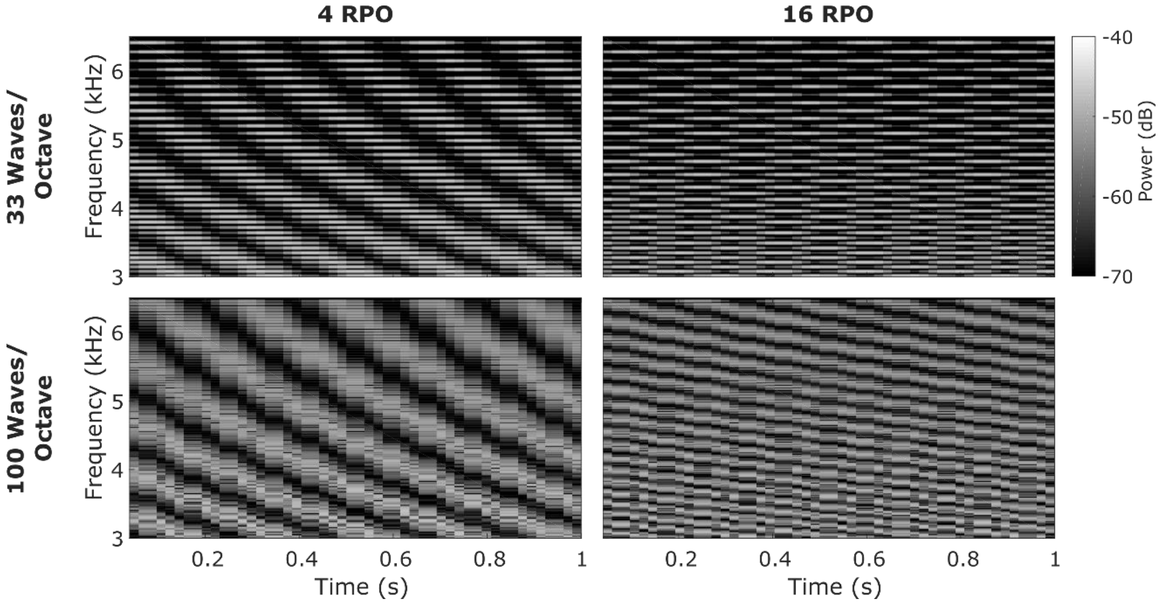

Figure A1.1 Spectrograms of SMR stimuli for 33.33 (top) and 100 (bottom) carrier densities at 4 (left) and 16 (right) RPO. Color mapping is according to relative level in dB. Note that these stimuli are shown without onset and offset ramps. A discrete Fast Fourier Transform frequency resolution of 50 Hz was used.

Figure 1 shows the power spectra of example of the types of SMR stimuli used. The top panels show SMR stimuli produced using 33 carriers per octave with 4 (left) and 16 (right) RPO. Likewise, the bottom panels present similar stimuli but produced with 100 carriers per octave. Both the 33 and 100 carrier per octave-based stimuli produce the expected spectro-temporal sweeps at 4 RPO. Notice, however, that the 33 ripple per octave power spectra shows periodic, unintended absence of signal due the discrete sampling of the ripples. While this effect is not observable in the 100 carrier per octave-based signals' spectra, this is merely due to spectral resolution limits of the discrete fast Fourier transform used. Moreover, while the 100 carrier per octave-based 16 RPO signal maintains the expected spectro-temporal sweeps the 33 carrier per octave version exhibits a more checkerboard like pattern with the desired ripples being interrupted by an unintended lower-frequency signal, in this case with opposing spectro-temporal direction to the desired ripples.

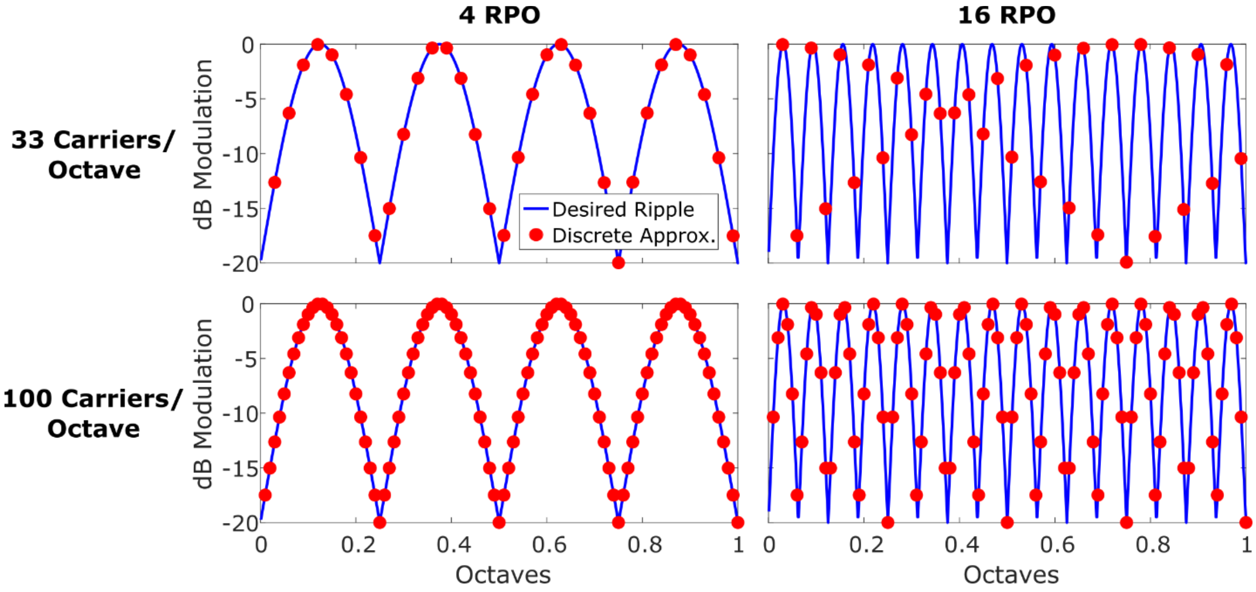

Figure A1.2 Time frozen spectrograms comparing ideal (blue lines) and discretely sampled (red markers) modulation spectra of SMR stimuli for 33.33 (top) and 100 (bottom) carrier densities at 4 (left) and 16 (right) RPO. For each modulation spectra, a single octave representing the frequency range from 100 to 200 Hz is illustrated.

The source of this unintended lower-frequency signal within the stimuli can be best illustrated by considering the discrete sampling of the frequency spectra modulations at a single time points (**Figure 2**). The top and bottom panels illustrate the intended and discretely approximated modulations for 33 and 100 carrier per octave stimuli, respectively. The left panels illustrate the modulation approach for relatively low (4 RPO) ripple densities while the right that of relatively high (16 RPO). For clarity, only a single octave representing the frequency range from 100 to 200 Hz is shown, however, the presented dynamics are consistent across the frequency spectrum. For the 4 RPO stimuli, both the 33 and 100 carrier per octave discrete modulation approaches sample at, or near, both the peaks and troughs of the idealized ripple pattern. Conversely, while the 100 carrier per octave sampling resolution largely captures the full range of the desired rippling on every cycle of the stimulus, the 33 carrier per octave-based stimuli do not. The relatively low spectral sampling density relative to that of the ripples leads to aliasing in the modulation intensity that introduces an additional lower density modulation.

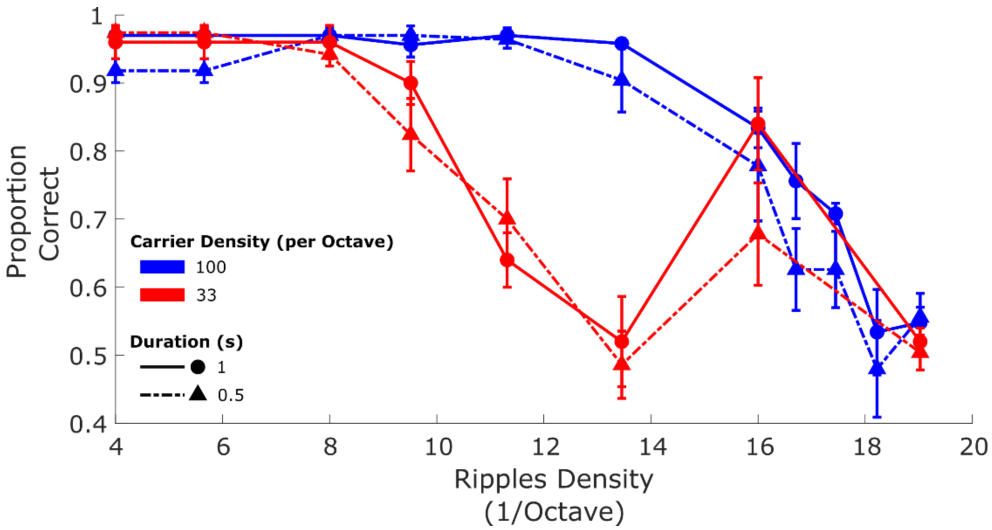

Figure A1.3 Group proportion correct plotted against ripple density for SMR discrimination task.

Mean data for 33.33 and 100 carriers per octave-based stimuli plotted in red and blue, respectively. Long stimuli (1 s) plotted as circular marks and solid lines and short (0.5 s) plotted as triangles and dashed lines. Error bars represent standard error of the mean (SEM) and N = 5 subjects for all conditions. All ripple stimuli were presented at a mean level of 75 dBA with a ripple depth of 20 dB.

To explore how the presence of the lower spectral frequency queue impacts SMR discrimination, a cohort of normal-hearing adults was tested asked to distinguish variable ripple densities from 20 RPO. **Figure 3** presents group mean percent correct data for all subjects from this experiment. With 100 carrier per octave stimuli the group, and individual (data not shown) psychometric curves exhibit a typical shape declining monotonically from saturation to chance. In contrast, the 33.33 carrier per octave yielded strongly non-monotonic psychometric curves that show a reduction in performance from saturation to chance between 8 and 13.454 RPO but a rebound in performance at 16 RPO. The effects of carrier rate, stimulus length, and ripple density on percent correct were examined using a linear mixed-effects model with compound symmetry covariance matrix. This analysis was chosen over a repeated measures ANOVA due to the fact that subjects were not tested at all ripple depths in the 33/octave carrier condition. Significant main effects for all three variables were observed with better mean percent correct scores associated with larger carrier rate [F(1,148) = 63.378, $p < 0.0001$], longer stimulus length [F(1,148) = 8.893, $p = 0.003$],, and smaller ripple density [F(10,148) = 63.229, $p < 0.0001$]. A significant interaction between ripple density and carrier rate was observed [F(7,148) = 17.411, $p < 0.0001$]. Paired comparisons between the two carrier rates at each ripple density revealed no significant differences at 4-8 RPO, 16 RPO or 19.03 RPO [all p's > 0.234] whereas higher carrier rate was associated with higher percent correct at 9.51 – 13.45 RPO [all p's < 0.011]. All other interactions failed to reach significance [all p's > 0.375]. The first 70% crossing, a typical threshold in SMR-based experiments, for the low carrier density signals is approximately 11 RPO for both stimulus durations, while for the high carrier density signals, they are 16.5 and 17.5 for the short and long stimuli, respectively.

A1.5 Discussion

Figure 1 and 2 present evidence that the use of an inadequate density of sine wave carriers can lead to spectral aliasing in SMR stimuli. The use of high carrier densities to produce spectrally rippled stimuli was previously leveraged by Jones et al. and then Horn et al., to produce static spectral ripple stimuli, however, they did not explicitly describe the spectral aliasing effect they sought to avoid in this work (Horn et al., 2017; Jones et al., 2013). In SMR stimuli, this aliasing effect can both interfere with intended ripple queues and introduce unintended low frequency spectro-temporal ripples. The nature of this aberrant queue depends on the difference between the desired ripple density and half the carrier density, akin to the Nyquist frequency in time series data. While we specifically illustrate this aliasing occurring in SMRs and note it in static spectral ripples, any other stimuli generated via band-limited approximation of spectral functions may produce similar effects.

The results of our psychophysical experiment suggest that, with a sufficiently high carrier density, normal hearing adults are able to discriminate 16.5, or even 17.5, ripple per octave SMR stimuli from a 20 ripple per octave standard. In contrast, the predominant carrier density used previously, 33.33 sine wave per octave, yields non-monotonic psychometric functions that suggest listeners begin losing access to desired spectral ripple queues above approximately 11 ripples per octave and may instead attend to the aliasing-induced queues. This finding demonstrates the importance of ensuring a sufficiently high carrier rate is selected to accurately measure SMR detection.

Listeners’ ability to detect ripple densities relatively near the 20 ripple per octave standard also indicates that this testing strategy is probing ripple discrimination rather than ripple detection. Going forward, it likely makes sense to modify this discrimination task by picking a phonetically relevant RPO standard (perhaps one with a ripple density mimicking the distance between formants) and reporting minimal discriminable ripple differences. Alternatively, if absolute SMR detection capabilities are of interest, transitioning to unmodulated standard stimuli and leveraging a sufficiently large number of carriers would avoid aliasing at the highest tested ripple densities. In pure tone discrimination tasks, normal hearing subjects can detect differences of ~1/200th octave in tone frequency (Dai and Micheyl, 2011). While SMR detection is likely more challenging, this suggests that absolute SMR detection thresholds may be substantially higher than previously thought in normal hearing listeners. Experiments using the SMR in CI users are limited to SMR densities below the limit where aliasing becomes significant, suggesting that findings in this population, notably the consistent correlation with speech outcomes, are likely robust to this effect.

Bibliography

Adenis, V., Gourévitch, B., Mamelle, E., Recugnat, M., Stahl, P., Gnansia, D., Nguyen, Y., Edeline, J.-M., 2018. ECAP growth function to increasing pulse amplitude or pulse duration demonstrates large inter-animal variability that is reflected in auditory cortex of the guinea pig. PLoS One 13, e0201771. doi:10.1371/journal.pone.0201771

Arnesan, A.R., Osen, K.K., 1978. The cochlear nerve in the cat: Topography, cochleotopy, and fiber spectrum. J. Comp. Neurol. 178, 661–678.

Aronoff, J.M., Landsberger, D.M., 2013. The development of a modified spectral ripple test. J. Acoust. Soc. Am. 134, EL217–EL222. doi:10.1121/1.4813802

Azadpour, M., McKay, C.M., Svirsky, M.A., 2018. Effect of Pulse Rate on Loudness Discrimination in Cochlear Implant Users. J. Assoc. Res. Otolaryngol. 299, 287–299. doi:10.1007/s10162-018-0658-8

Basser, P.J., 2004. Scaling laws for myelinated axons derived from an electrotonic core-conductor model. J. Integr. Neurosci. 3, 227–244. doi:10.1142/S0219635204000427

Basura, G.J., Eapen, R., Buchman, C.A., 2009. Bilateral cochlear implantation: Current concepts, indications, and results. Laryngoscope 119, 2395–2401. doi:10.1002/lary.20751

Bernstein, L.R., 2001. Auditory processing of interaural timing information: New insights. J. Neurosci. Res. 66, 1035–1046. doi:10.1002/jnr.10103

Bernstein, L.R., Trahiotis, C., 2017. An interaural-correlation-based approach that accounts for a wide variety of binaural detection data. J. Acoust. Soc. Am. 141, 1150. doi:10.1121/1.4976098

Bernstein, L.R., Trahiotis, C., 2015. Converging measures of binaural detection yield estimates of precision of coding of interaural temporal disparities. J. Acoust. Soc. Am. 138, EL474–EL479. doi:10.1121/1.4935606

Berthold, C.-H., 1978. Morphology of normal peripheral axons. Physiol. Pathobiol. Axons 3, 63.

Bierer, J.A., Faulkner, K.F., Tremblay, K.L., 2011. Identifying Cochlear Implant Channels With Poor Electrode-Neuron Interfaces: Electrically Evoked Auditory Brain Stem Responses Measured With the Partial Tripolar Configuration. Ear Hear. 32, 436–444.

Blamey, P., Arndt, P., Bergeron, F., Bredberg, G., Brimacombe, J., Facer, G., Larky, J., Lindström, B., Nedzelski, J., Peterson, A., Shipp, D., Staller, S., Whitford, L., 1996. Factors affecting auditory performance of postlinguistically deaf adults using cochlear implants. Audiol. Neurootol. 1, 293–306. doi:10.1159/000259212

Blamey, P., Artieres, F., Başkent, D., Bergeron, F., Beynon, A., Burke, E., Dillier, N., Dowell, R., Fraysse, B., Gallégo, S., Govaerts, P.J., Green, K., Huber, A.M., Kleine-Punte, A., Maat, B., Marx, M., Mawman, D., Mosnier, I., O'Connor, A.F., O'Leary, S., Rousset, A., Schauwers, K., Skarzynski, H., Skarzynski, P.H., Sterkers, O., Terranti, A., Truy, E., Van De Heyning, P., Venail, F., Vincent, C., Lazard, D.S., 2012. Factors affecting auditory performance of postlinguistically deaf adults using cochlear implants: An update with 2251 patients. Audiol. Neurotol. 18, 36–47. doi:10.1159/000343189

Bond, M., Mealing, S., Anderson, R., Elston, J., Weiner, G., Taylor, R.S., Hoyle, M., Liu, Z., Price, A., Stein, K., 2009. The effectiveness and cost-effectiveness of cochlear implants for severe to profound deafness in children and adults: A systematic review and economic model. Health Technol. Assess. (Rockv). 13. doi:10.3310/hta13440

Boulet, J., Bruce, I.C., 2017a. Predictions of the Contribution of HCN Half-Maximal Activation Potential Heterogeneity to Variability in Intrinsic Adaptation of Spiral Ganglion Neurons. J. Assoc. Res. Otolaryngol. 18, 301–322. doi:10.1007/s10162-016-0605-5

Boulet, J., Bruce, I.C., 2017b. Predictions of the Contribution of HCN Half-Maximal Activation

Potential Heterogeneity to Variability in Intrinsic Adaptation of Spiral Ganglion Neurons. JARO - J. Assoc. Res. Otolaryngol. 18, 301–322. doi:10.1007/s10162-016-0605-5

Boulet, J., White, M., Bruce, I.C., 2016. Temporal Considerations for Stimulating Spiral Ganglion Neurons with Cochlear Implants. J. Assoc. Res. Otolaryngol. 17, 1–17. doi:10.1007/s10162-015-0545-5

Brant, J.A., Eliades, S.J., Kaufman, H., Chen, J., Ruckenstein, M.J., 2018. AzBio Speech Understanding Performance in Quiet and Noise in High Performing Cochlear Implant Users. Otol. Neurotol. 39, 571–575. doi:10.1097/MAO.0000000000001765

Briaire, J.J., Frijns, J.H.M., 2006. The consequences of neural degeneration regarding optimal cochlear implant position in scala tympani: A model approach. Hear. Res. 214, 17–27. doi:10.1016/j.heares.2006.01.015

Briaire, J.J., Frijns, J.H.M., 2005. Unraveling the electrically evoked compound action potential. Hear. Res. 205, 143–156. doi:10.1016/j.heares.2005.03.020

Briaire, J.J., Frijns, J.H.M., 2000a. 3D mesh generation to solve the electrical volume conduction problem in the implanted inner ear. Simul. Pract. Theory 8, 57–73. doi:10.1016/S0928-4869(00)00007-0

Briaire, J.J., Frijns, J.H.M., 2000b. Field patterns in a 3D tapered spiral model of the electrically stimulated cochlea. Hear. Res. 148, 18–30. doi:10.1016/S0378-5955(00)00104-0

Brismar, T., 1981. Electrical properties of isolated demyelinated rat nerve fibres. Acta Physiol. Scand. 113, 151–166. doi:10.1111/j.1748-1716.1981.tb06877.x

Brown, A.D., Stecker, G.C., 2010. Temporal weighting of interaural time and level differences in high-rate click trains. J. Acoust. Soc. Am. 128, 332–341. doi:10.1121/1.3436540

Budenz, C.L., Cosetti, M.K., Coelho, D.H., Birenbaum, B., Babb, J., Waltzman, S.B., Roehm, P.C.,

2011. The effects of cochlear implantation on speech perception in older adults. J. Am. Geriatr. Soc. 59, 446–453. doi:10.1111/j.1532-5415.2010.03310.x

Chow, C.C., White, J. a, 1996. Spontaneous action potentials due to channel fluctuations. Biophys. J. 71, 3013–3021. doi:10.1016/S0006-3495(96)79494-8

Chung, Y., Hancock, K.E., Delgutte, B., 2016. Neural Coding of Interaural Time Differences with Bilateral Cochlear Implants in Unanesthetized Rabbits. J. Neurosci. 36, 5520–5531. doi:10.1523/JNEUROSCI.3795-15.2016

Cianfrone, G., Turchetta, R., Mazzei, F., Bartolo, M., Parisi, L., 2006. Temperature-Dependent Auditory Neuropathy: Is it an Acoustic Uhthoff-like Phenomenon?; A Case Report. Ann. Otol. Rhinol. Laryngol. 115, 518–527. doi:10.1177/000348940611500706

Craner, M.J., Lo, A.C., Black, J.A., Waxman, S.G., 2003. Abnormal sodium channel distribution in optic nerve axons in a model of inflammatory demyelination. Brain 126, 1552–1561. doi:10.1093/brain/awg153

Crowson, M.G., Semenov, Y.R., Tucci, D.L., Niparko, J.K., 2018. Quality of Life and Cost-Effectiveness of Cochlear Implants: A Narrative Review. Audiol. Neurotol. doi:10.1159/000481767

Dai, H., Micheyl, C., 2011. Psychometric functions for pure-tone frequency discrimination. J. Acoust. Soc. Am. 130, 263–272. doi:10.1121/1.3598448

de Vos, J.J., Biesheuvel, J.D., Briaire, J.J., Boot, P.S., van Gendt, M.J., Dekkers, O.M., Fiocco, M., Frijns, J.H.M., 2018. Use of Electrically Evoked Compound Action Potentials for Cochlear Implant Fitting. Ear Hear. 39, 401–411. doi:10.1097/AUD.0000000000000495

DeVries, L., Scheperle, R., Bierer, J.A., 2016. Assessing the Electrode-Neuron Interface with the Electrically Evoked Compound Action Potential, Electrode Position, and Behavioral

Thresholds. J. Assoc. Res. Otolaryngol. 17, 237–252. doi:10.1007/s10162-016-0557-9

DiNino, M., Arenberg, J.G., 2018. Age-Related Performance on Vowel Identification and the Spectral-temporally Modulated Ripple Test in Children With Normal Hearing and With Cochlear Implants. Trends Hear. 22, 233121651877095. doi:10.1177/2331216518770959

Dorman, M.F., Loiselle, L.H., Cook, S.J., Yost, W.A., Gifford, R.H., 2017. Sound source localization by normal hearing listeners, hearing-impaired listeners and cochlear implant listeners. Audiol. Neurotol. 21, 127–131. doi:10.1159/000444740.Sound

Drennan, W.R., Oleson, J.J., Gfeller, K., Crosson, J., Driscoll, V.D., Won, J.H., Anderson, E.S., Rubinstein, J.T., 2015. Clinical evaluation of music perception, appraisal and experience in cochlear implant users. Int. J. Audiol. 54, 114–123. doi:10.3109/14992027.2014.948219

Drennan, W.R., Won, J.H., Nie, K., Jameyson, E., Rubinstein, J.T., 2010. Sensitivity of psychophysical measures to signal processor modifications in cochlear implant users. Hear. Res. 262, 1–8. doi:10.1016/j.heares.2010.02.003

Eijl, R.H.M. Van, Buitenhuis, P.J., Stegeman, I., Klis, S.F.L., 2017. Systematic Review of Compound Action Potentials as Predictors for Cochlear Implant Performance. Laryngoscope 127, 476–487. doi:10.1002/lary.26154

El-Badry, M.M., Ding, D.L., McFadden, S.L., Eddins, A.C., 2007. Physiological effects of auditory nerve myelinopathy in chinchillas. Eur. J. Neurosci. 25, 1437–1446. doi:10.1111/j.1460-9568.2007.05401.x

Eppsteiner, R.W., Shearer, A.E., Hildebrand, M.S., DeLuca, A.P., Ji, H., Dunn, C.C., Black-Ziegelbein, E.A., Casavant, T.L., Braun, T.A., Scheetz, T.E., Scherer, S.E., Hansen, M.R., Gantz, B.J., Smith, R.J.H., 2012. Prediction of cochlear implant performance by genetic mutation: The spiral ganglion hypothesis. Hear. Res. 292, 51–58.

doi:10.1016/j.heares.2012.08.007

Finley, C.C., Wilson, B.S., White, M.W., 1990. Models of Neural Responsiveness to Electrical Stimulation, in: Cochlear Implants. Springer New York, New York, NY, pp. 55–96. doi:10.1007/978-1-4612-3256-8_5

Francart, T., Lenssen, A., Buechner, A., Lenarz, T., Wouters, J., 2014. Effect of channel synchrony on interaural time difference perception with bilateral cochlear implants. Ear Hear. submitted, 199–206. doi:10.1097/AUD.0000000000000152

Freyman, R.L., 1997. Onset dominance in lateralization. J. Acoust. Soc. Am. 101, 1649. doi:10.1121/1.418149

Freyman, R.L., Helfer, K.S., McCall, D.D., Clifton, R.K., 1999. The role of perceived spatial separation in the unmasking of speech. J. Acoust. Soc. Am. 106, 3578–88.

Frijns, J.H.M., Briaire, J.J., Grote, J.J., 2001. The importance of human cochlear anatomy for the results of modiolus-hugging multichannel cochlear implants. Otol. Neurotol. 22, 340–349. doi:10.1097/00129492-200105000-00012

Frijns, J.H.M., Briaire, J.J., Schoonhoven, R., 2000. Integrated use of volume conduction and neural models to simulate the response to cochlear implants. Simul. Pract. Theory 8, 75–97. doi:10.1016/S0928-4869(00)00008-2

Frijns, J.H.M., Mooij, J., ten Kate, J.H., 1994. A Quantitative Approach to Modeling Mammalian Myelinated Nerve Fibers for Electrical Prosthesis Design. IEEE Trans. Biomed. Eng. 41, 556–566. doi:10.1109/10.293243

Furman, A.C., Kujawa, S.G., Liberman, M.C., 2013. Noise-induced cochlear neuropathy is selective for fibers with low spontaneous rates. J. Neurophysiol. 110, 577–86. doi:10.1152/jn.00164.2013

Galvin, J.J., Fu, Q.J., 2009. Influence of stimulation rate and loudness growth on modulation detection and intensity discrimination in cochlear implant users. Hear. Res. 250, 46–54. doi:10.1016/j.heares.2009.01.009

Geers, A.E., Strube, M.J., Tobey, E.A., Pisoni, D.B., Moog, J.S., 2011. Epilogue: Factors Contributing to Long-Term Outcomes of Cochlear Implantation in Early Childhood. Ear Hear. 32, 84S-92S. doi:10.1097/AUD.0b013e3181ffd5b5

Gillespie, D.T., 1977. Exact Stochastic Simulation of Coupled Chemical Reactions. J. Phys. Chem. 81, 2340–2361.

Goldwyn, Joshua H, Bierer, S.M., Bierer, J.A., 2010. Modeling the electrode-neuron interface of cochlear implants: Effects of neural survival, electrode placement, and the partial tripolar configuration. Hear. Res. 268, 93–104. doi:10.1016/j.heares.2010.05.005

Goldwyn, J.H., Rubinstein, J.T., Shea-Brown, E., 2012. A point process framework for modeling electrical stimulation of the auditory nerve. J. Neurophysiol. 108, 1430–1452. doi:10.1152/jn.00095.2012

Goldwyn, Joshua H., Shea-Brown, E., Rubinstein, J.T., 2010. Encoding and decoding amplitude-modulated cochlear implant stimuli-a point process analysis. J. Comput. Neurosci. 28, 405–424. doi:10.1007/s10827-010-0224-9

Guérit, F., Marozeau, J., Deeks, J.M., Epp, B., Carlyon, R.P., 2018. Effects of the relative timing of opposite-polarity pulses on loudness for cochlear implant listeners. J. Acoust. Soc. Am. 144, 2751–2763. doi:10.1121/1.5070150

Hanekom, T., Hanekom, J., 2016. Three-dimensional models of cochlear implants: A review of their development and how they could support management and maintenance of cochlear implant performance. Netw. Comput. Neural Syst. doi:10.3109/0954898X.2016.1171411

Hardie, N. a, Shepherd, R.K., 1999. Sensorineural hearing loss during development: morphological and physiological response of the cochlea and auditory brainstem. Hear. Res. 128, 147–165. doi:10.1016/s0378-5955(98)00209-3

Hawley, M.L., Litovsky, R.Y., Culling, J.F., 2004. The benefit of binaural hearing in a cocktail party: effect of location and type of interferer. J. Acoust. Soc. Am. 115, 833–43.

Holden, L.K., Firszt, J.B., Reeder, R.M., Uchanski, R.M., Dwyer, N.Y., Holden, T.A., 2016. Factors Affecting Outcomes in Cochlear Implant Recipients Implanted With a Perimodiolar Electrode Array Located in Scala Tympani. Otol. Neurotol. 37, 1662–1668. doi:10.1097/MAO.0000000000001241

Horn, D.L., Won, J.H., Rubinstein, J.T., Werner, L.A., 2017. Spectral Ripple Discrimination in Normal-Hearing Infants. Ear Hear. 38, 212–222. doi:10.1097/AUD.0000000000000373

Hossain, W.A., Antic, S.D., Yang, Y., Rasband, M.N., Morest, D.K., 2005. Where Is the Spike Generator of the Cochlear Nerve? Voltage-Gated Sodium Channels in the Mouse Cochlea. J. Neurosci. 25, 6857–6868. doi:10.1523/JNEUROSCI.0123-05.2005

Hughes, M.L., Laurello, S.A., 2017. Effect of stimulus level on the temporal response properties of the auditory nerve in cochlear implants. Hear. Res. 1–14. doi:10.1016/j.heares.2017.06.004

Imennov, N.S., Rubinstein, J.T., 2009. Stochastic population model for electrical stimulation of the auditory nerve. IEEE Trans. Biomed. Eng. 56, 2493–2501. doi:10.1109/TBME.2009.2016667

Imennov, N.S., Won, J.H., Drennan, W.R., Jameyson, E., Rubinstein, J.T., 2013. Detection of acoustic temporal fine structure by cochlear implant listeners: Behavioral results and computational modeling. Hear. Res. 298, 60–72. doi:10.1016/j.heares.2013.01.004

Incesulu, A., Nadol, J.B., 1998. Correlation of acoustic threshold measures and spiral ganglion cell survival in severe to profound sensorineural hearing loss: Implications for cochlear implantation. Ann. Otol. Rhinol. Laryngol. 107, 906–911. doi:10.1177/000348949810701102

Javel, E., Shepherd, R.K., 2000. Electrical stimulation of the auditory nerve. III. Response initiation sites and temporal fine structure. Hear. Res. 140, 45–76. doi:10.1016/S0378-5955(99)00186-0

Jia, N., Kong, B., Liu, Q., Diao, X., Xia, X., 2012. Antioxidant activity of black currant (Ribes nigrum L.) extract and its inhibitory effect on lipid and protein oxidation of pork patties during chilled storage. Meat Sci. 91, 533–539. doi:10.1016/j.meatsci.2012.03.010

Jones, G.L., Won, J.H., Drennan, W.R., Rubinstein, J.T., 2013. Relationship between channel interaction and spectral-ripple discrimination in cochlear implant users. J. Acoust. Soc. Am. 133, 425–33. doi:10.1121/1.4768881

Joshi, S.N., Dau, T., Epp, B., 2017. A Model of Electrically Stimulated Auditory Nerve Fiber Responses with Peripheral and Central Sites of Spike Generation. J. Assoc. Res. Otolaryngol. doi:10.1007/s10162-016-0608-2

Kalkman, R.K., Briaire, J.J., Frijns, J.H.M., Kalkman, R.K., Briaire, J.J., Stimulation, J.H.M.F., 2016. Stimulation strategies and electrode design in computational models of the electrically stimulated cochlea: An overview of existing literature. Netw. Comput. Neural Syst. 6536, 0–28. doi:10.3109/0954898X.2016.1171412

Kan, A., Litovsky, R.Y., 2014. Binaural hearing with electrical stimulation. Hear. Res. 322, 127–137. doi:10.1016/j.heares.2014.08.005

Kan, A., Litovsky, R.Y., Goupell, M.J., 2015. Effects of interaural pitch matching and auditory image centering on binaural sensitivity in cochlear implant users. Ear Hear. 36, e62--8. doi:10.1097/AUD.0000000000000135

Kim, J.-R., Abbas, P.J., Brown, C.J., Etler, C.P., O'Brien, S., Kim, L., 2010. The Relationship Between Electrically Evoked Compound Action Potential and Speech Perception. Otol. Neurotol. 31, 1041–1048. doi:10.1097/MAO.0b013e3181ec1d92

Kirby, B., Brown, C., Abbas, P., Etler, C., Brien, S.O., 2012. Relationships Between Electrically Evoked Potentials and Loudness Growth in Bilateral Cochlear Implant Users 389–398.

Klein-Hennig, M., Dietz, M., Hohmann, V., Ewert, S.D., 2011. The influence of different segments of the ongoing envelope on sensitivity to interaural time delays. J. Acoust. Soc. Am. 129, 3856–3872. doi:10.1121/1.3585847

Kolaric, K. V, Thomson, G., Edgar, J.M., Brown, A.M., 2013. Focal axonal swellings and associated ultrastructural changes attenuate conduction velocity in central nervous system axons: a computer modeling study. Physiol. Rep. 1, e00059. doi:10.1002/phy2.59

Koles, Z.J., Rasminsky, M., 1972. A computer simulation of conduction in demyelinated nerve fibres. J. Physiol. 227, 351–64. doi:10.1113/jphysiol.1972.sp010036

Kroon, S., Ramekers, D., Smeets, E.M., Hendriksen, F.G.J., Klis, S.F.L., Versnel, H., 2017. Degeneration of auditory nerve fibers in guinea pigs with severe sensorineural hearing loss. Hear. Res. 345, 79–87. doi:10.1016/j.heares.2017.01.005

Kujawa, S.G., Liberman, M.C., 2009. Adding insult to injury: cochlear nerve degeneration after “temporary” noise-induced hearing loss. J. Neurosci. 29, 14077–85. doi:10.1523/JNEUROSCI.2845-09.2009

Landry, T.G., Wise, A.K., Fallon, J.B., Shepherd, R.K., 2011. Spiral ganglion neuron survival and function in the deafened cochlea following chronic neurotrophic treatment. Hear. Res. 282, 303–13. doi:10.1016/j.heares.2011.06.007

Lawler, M., Yu, J., Aronoff, J.M., 2017. Comparison of the Spectral-Temporally Modulated Ripple Test With the Arizona Biomedical Institute Sentence Test in Cochlear Implant Users. Ear Hear. 1. doi:10.1097/AUD.0000000000000496

Lazard, D.S., Vincent, C., Venail, F., van de Heyning, P., Truy, E., Sterkers, O., Skarzynski, P.H., Skarzynski, H., Schauwers, K., O'Leary, S., Mawman, D., Maat, B., Kleine-Punte, A., Huber, A.M., Green, K., Govaerts, P.J., Fraysse, B., Dowell, R., Dillier, N., Burke, E., Beynon, A., Bergeron, F., Başkent, D., Artières, F., Blamey, P.J., 2012. Pre-, Per- and Postoperative Factors Affecting Performance of Postlinguistically Deaf Adults Using Cochlear Implants: A New Conceptual Model over Time. PLoS One 7, 1–11. doi:10.1371/journal.pone.0048739

Leake, P.A., Hradek, G.T., 1988. Cochlear pathology of long term neomycin induced deafness in cats. Hear. Res. 33, 11–33. doi:10.1016/0378-5955(88)90018-4

Leake, P.A., Hradek, G.T., Rebscher, S.J., Snyder, R.L., 1991. Chronic intracochlear electrical stimulation induces selective survival of spiral ganglion neurons in neonatally deafened cats. Hear. Res. 54, 251–271. doi:10.1016/0378-5955(91)90120-X

Liberman, M. Charles, Oliver, M.E., 1984. Morphometry of intracellularly labeled neurons of the auditory nerve: correlations with functional properties. J. Comp. Neurol. 223, 163–176. doi:10.1002/cne.902230203

Liberman, M C, Oliver, M.E., 1984. Morphometry of intracellularly labeled neurons of the auditory nerve: correlations with functional properties. J. Comp. Neurol. 223, 163–176. doi:10.1002/cne.902230203

Litovsky, R.Y., Goupell, M.J., Godar, S., Grieco-Calub, T., Jones, G.L., Garadat, S.N., Agrawal, S., Kan, A., Todd, A., Hess, C., Misurelli, S., 2012. Studies on Bilateral Cochlear Implants at the University of Wisconsin Binaural Hearing and Speech Lab. J. Am. Acad. Audiol. 494, 476–494. doi:10.3766/jaaa.23.6.9

Litovsky, R.Y., Jones, G.L., Agrawal, S., van Hoesel, R., 2010. Effect of age at onset of deafness on binaural sensitivity in electric hearing in humans. J. Acoust. Soc. Am. 127, 400–414. doi:10.1121/1.3257546

Macherey, O., Carlyon, R.P., Chatron, J., Roman, S., 2017. Effect of Pulse Polarity on Thresholds and on Non-monotonic Loudness Growth in Cochlear Implant Users. J. Assoc. Res. Otolaryngol. 527, 513–527. doi:10.1007/s10162-016-0614-4

Macherey, O., Van Wieringen, A., Carlyon, R.P., Deeks, J.M., Wouters, J., 2006. Asymmetric pulses in cochlear implants: Effects of pulse shape, polarity, and rate. JARO - J. Assoc. Res. Otolaryngol. 7, 253–266. doi:10.1007/s10162-006-0040-0

Makary, C.A., Shin, J., Kujawa, S.G., Liberman, M.C., Merchant, S.N., 2011. Age-related primary cochlear neuronal degeneration in human temporal bones. JARO - J. Assoc. Res. Otolaryngol. 12, 711–717. doi:10.1007/s10162-011-0283-2

Malherbe, T.K., Hanekom, T., Hanekom, J.J., 2015. The effect of the resistive properties of bone on neural excitation and electric fields in cochlear implant models. Hear. Res. 327, 126–135. doi:10.1016/j.heares.2015.06.003

McIntyre, C.C., Richardson, A.G., Grill, W.M., 2002. Modeling the Excitability of Mammalian Nerve Fibers: Influence of Afterpotentials on the Recovery Cycle. J. Neurophysiol. 87, 995–1006. doi:10.1152/jn.00353.2001

Medina, M.D.M., Polo, R., Gutierrez, A., Muriel, A., Vaca, M., Perez, C., Cordero, A., Cobeta, I., 2017. Cochlear Implantation in Postlingual Adult Patients with Long-Term Auditory Deprivation. Otol. Neurotol. 38, e248–e252. doi:10.1097/MAO.0000000000001257

Miller, C.A., Abbas, P.J., Nourski, K. V., Hu, N., Robinson, B.K., 2003. Electrode configuration influences action potential initiation site and ensemble stochastic response properties. Hear. Res. 175, 200–214. doi:10.1016/S0378-5955(02)00739-6

Miller, C.A., Abbas, P.J., Robinson, B.K., Nourski, K. V., Zhang, F., Jeng, F.C., 2006. Electrical excitation of the acoustically sensitive auditory nerve: Single-fiber responses to electric pulse trains. JARO - J. Assoc. Res. Otolaryngol. 7, 195–210. doi:10.1007/s10162-006-0036-9

Miller, C.A., Abbas, P.J., Robinson, B.K., Rubinstein, J.T., Matsuoka, A.J., 1999. Electrically evoked single-fiber action potentials from cat: Responses to monopolar, monophasic stimulation. Hear. Res. 130, 197–218. doi:10.1016/S0378-5955(99)00012-X

Miller, C.A., Brown, C.J., Abbas, P.J., Chi, S., 2008. The clinical application of potentials evoked from the peripheral auditory system. Hear. Res. 242, 184–197. doi:10.1016/j.heares.2008.04.005

Miller, C.A., Robinson, B.K., Rubinstein, J.T., Abbas, P.J., Runge-Samuelson, C.L., 2001. Auditory nerve responses to monophasic and biphasic electric stimuli. Hear. Res. 151, 79–94. doi:10.1016/S0300-2977(00)00082-6

Mino, H., Grill, W.M., 2002. Effects of stochastic sodium channels on extracellular excitation of myelinated nerve fibers. IEEE Trans. Biomed. Eng. 49, 527–532. doi:10.1109/TBME.2002.1001966

Mino, H., Rubinstein, J.T., Miller, C.A., Abbas, P.J., 2004. Effects of Electrode-to-Fiber Distance on Temporal Neural Response with Electrical Stimulation. IEEE Trans. Biomed. Eng. 51, 13–20. doi:10.1109/TBME.2003.820383

Montal, M., Mueller, P., 1972. Formation of bimolecular membranes from lipid monolayers and a study of their electrical properties. Proc. Natl. Acad. Sci. U. S. A. 69, 3561–3566. doi:10.1073/pnas.69.12.3561

Nadol, J.B., 1988. Quantification of human spiral ganglion cells by serial section reconstruction and segmental density estimates. Am. J. Otolaryngol. 9, 47–51. doi:10.1016/S0196-0709(88)80007-3

Negm, M.H., Bruce, I.C., 2014. The Effects of HCN and KLT Ion Channels on Adaptation and Refractoriness in a Stochastic Auditory Nerve Model. IEEE Trans. Biomed. Eng. 61, 2749–

2759. doi:10.1109/TBME.2014.2327055

Niparko, J.K., Kirk, K.I., Robbins, A.M.C., Mellon, N.K., Tucci, D.L., Wilson, B.S., 2009. Cochlear Implants: Principles & Practices. Wolters Kluwer Health/Lippincott Williams & Wilkins.

Nordlund, B., 1962. Physical Factors in Angular Localization. Acta Otolaryngol. 54, 75–93. doi:10.3109/00016486209126924

O'Brien, G.E., Imennov, N.S., Rubinstein, J.T., 2016. Simulating electrical modulation detection thresholds using a biophysical model of the auditory nerve; J. Acoust. Soc. Am. 139, 2448–2462. doi:10.1121/1.4947430

O'Brien, G.E., Rubinstein, J.T., 2016. The development of biophysical models of the electrically stimulated auditory nerve: Single-node and cable models. Netw. Comput. Neural Syst. doi:10.3109/0954898X.2016.1162338

Orabi, A., Mawman, D., Al-Zoubi, F., Saeed, S.R., Ramsden, R., 2006. Cochlear implant outcomes and quality of life in the elderly: Manchester experience over 13 years1. Clin. Otolaryngol. 31, 116–122. doi:10.1111/j.1749-4486.2006.01156.x

Pfingst, B.E., Hughes, A.P., Colesa, D.J., Watts, M.M., Strahl, S.B., Raphael, Y., 2015. Insertion trauma and recovery of function after cochlear implantation: Evidence from objective functional measures. Hear. Res. 330, 98–105. doi:10.1016/j.heares.2015.07.010

Poissant, S.F., Bero, E.M., Busekroos, L., Shao, W., 2014. Determining cochlear implant users' true noise tolerance: use of speech reception threshold in noise testing. Otol. Neurotol. 35, 414–20. doi:10.1097/MAO.0000000000000246

Prado-Guitierrez, P., Fewster, L.M., Heasman, J.M., McKay, C.M., Shepherd, R.K., 2006. Effect of interphase gap and pulse duration on electrically evoked potentials is correlated with auditory nerve survival. Hear. Res. 215, 47–55. doi:10.1016/j.heares.2006.03.006

Ramekers, D., Versnel, H., Strahl, S.B., Smeets, E.M., Klis, S.F.L., Grolman, W., 2014. Auditory-Nerve Responses to Varied Inter-Phase Gap and Phase Duration of the Electric Pulse Stimulus as Predictors for Neuronal Degeneration. J. Assoc. Res. Otolaryngol. 15, 187–202. doi:10.1007/s10162-013-0440-x

Rattay, F., Leao, R.N., Felix, H., 2001a. A model of the electrically excited human cochlear neuron. II. Influence of the three-dimensional cochlear structure on neural excitability. Hear. Res. doi:10.1016/S0378-5955(00)00257-4

Rattay, F., Lutter, P., Felix, H., 2001b. A model of the electrically excited human cochlear neuron I. Contribution of neural substructures to the generation and propagation of spikes. Hear. Res. 153, 43–63. doi:10.1016/S0378-5955(00)00256-2

Resnick, J.M., O'Brien, G., Rubinstein, J.T., 2018. Simulated auditory nerve axon demyelination alters sensitivity and response timing to extracellular stimulation. Hear. Res. 361, 121–137. doi:10.1016/j.heares.2018.01.014

Robertson, D., 1983. Functional significance of dendritic swelling after loud sounds in the guinea pig cochlea. Hear. Res. 9, 263–278. doi:10.1016/0378-5955(83)90031-X

Rosen, S., 1992. Temporal Information in Speech: Acoustic, Auditory and Linguistic Aspects. Philos. Trans. R. Soc. B Biol. Sci. doi:10.1098/rstb.1992.0070

Rubinstein, J.T., 2004. An introduction to the biophysics of the electrically evoked compound action potential. Int. J. Audiol. 43 Suppl 1, S3-9.

Rubinstein, J.T., 1993. Axon Termination Conditions for Electrical Stimulation. IEEE Trans. Biomed. Eng. 40, 654–663. doi:10.1109/10.237695

Rubinstein, J.T., 1988. Quasi – Static Analytical Models for Electrical Stimulation of the Auditory Nervous System. University of Washington.

Rubinstein, J.T., Miller, C.A., Mino, H., Abbas, P.J., 2001. Analysis of monophasic and biphasic electrical stimulation of nerve. IEEE Trans. Biomed. Eng. 48, 1065–1070. doi:10.1109/10.951508

Rubinstein, J.T., Parkinson, W.S., Tyler, R.S., Gantz, B.J., 1999. Residual speech recognition and cochlear implant performance: effects of implantation criteria. Am. J. Otol. 20, 445–52.

Rushton, W.A.H., 1951. A theory of the effects of fibre size in medullated nerve. J. Physiol. 115, 101–122. doi:10.1113/jphysiol.1951.sp004655

Saberi, K., Perrott, D.R., 1999. Cognitive restoration of reversed speech. Nature 398, 760. doi:10.1038/19652

Schvartz-Leyzac, K.C., Pfingst, B.E., 2017. Assessing the Relationship Between the Electrically Evoked Compound Action Potential and Speech Recognition Abilities in Bilateral Cochlear Implant Recipients. Ear Hear. 1–15. doi:10.1097/AUD.0000000000000490

Schwarz, J.R., Reid, G., Bostock, H., 1995. Action potentials and membrane currents in the human node of Ranvier. Pflugers Arch. Eur. J. Physiol. 430, 283–292. doi:10.1007/BF00374660

Seyyedi, M., Viana, L.M., Nadol, J.B., 2014. Within-subject comparison of word recognition and spiral ganglion cell count in bilateral cochlear implant recipients. Otol. Neurotol. 35, 1446–1450. doi:10.1097/MAO.0000000000000445

Shannon, R. V., 1992. Temporal modulation transfer functions in patients with cochlear implants. J. Acoust. Soc. Am. 91, 2156–2164. doi:10.1121/1.403807

Shearer, A.E., Eppsteiner, R.W., Frees, K., Tejani, V., Sloan-Heggen, C.M., Brown, C., Abbas, P., Dunn, C., Hansen, M.R., Gantz, B.J., Smith, R.J.H., 2017. Genetic variants in the peripheral auditory system significantly affect adult cochlear implant performance. Hear. Res. 348, 138–142. doi:10.1016/j.heares.2017.02.008

Shepherd, R.K., Hardie, N.A., 2001. Deafness-induced changes in the auditory pathway: Implications for cochlear implants. Audiol. Neuro-Otology 6, 305–318. doi:10.1159/000046843

Shepherd, R.K., Javel, E., 1999. Electrical stimulation of the auditory nerve: II. Effect of stimulus waveshape on single fibre response properties. Hear. Res. 130, 171–188. doi:Doi 10.1016/S0378-5955(99)00011-8

Shepherd, R.K., Javel, E., 1997. Electrical stimulation of the auditory nerve. I. Correlation of physiological responses with cochlear status. Hear. Res. 108, 112–144. doi:10.1016/S0378-5955(97)00046-4

Shepherd, R.K., Roberts, L.A., Paolini, A.G., 2004. Long-term sensorineural hearing loss induces functional changes in the rat auditory nerve. Eur. J. Neurosci. 20, 3131–3140. doi:10.1111/j.1460-9568.2004.03809.x

Sly, D.J., Heffer, L.F., White, M.W., Shepherd, R.K., Birch, M.G.J., Minter, R.L., Nelson, N.E., Wise, A.K., O'Leary, S.J., 2007. Deafness alters auditory nerve fibre responses to cochlear implant stimulation. Eur. J. Neurosci. 26, 510–522. doi:10.1111/j.1460-9568.2007.05678.x

Tagoe, T., Barker, M., Jones, A., Allcock, N., Hamann, M., 2014. Auditory Nerve Perinodal Dysmyelination in Noise-Induced Hearing Loss. J. Neurosci. 34, 2684–2688. doi:10.1523/JNEUROSCI.3977-13.2014

Tasaki, I., 1955. New measurements of the capacity and the resistance of the myelin sheath and the nodal membrane of the isolated frog nerve fiber. Am. J. Physiol. 181, 639–50.

van Gendt, M.J., Briaire, J.J., Kalkman, R.K., Frijns, J.H.M., 2016. A fast, stochastic, and adaptive model of auditory nerve responses to cochlear implant stimulation. Hear. Res. 341, 130–143. doi:10.1016/j.heares.2016.08.011

Vollmer, M., Leake, P.A., Beitel, R.E., Rebscher, S.J., Snyder, R.L., 2005. Degradation of Temporal

Resolution in the Auditory Midbrain After Prolonged Deafness Is Reversed by Electrical Stimulation of the Cochlea. J. Neurophysiol. 93, 3339–3355. doi:10.1152/jn.00900.2004

Wan, G., Corfas, G., 2017. Transient auditory nerve demyelination as a new mechanism for hidden hearing loss. Nat. Commun. 8, 1–13. doi:10.1038/ncomms14487

White, J.A., Rubinstein, J.T., Kay, A.R., 2000. Channel noise in neurons. Trends Neurosci. 23, 131–137. doi:10.1016/S0166-2236(99)01521-0

Wightman, F.L., Kistler, D.J., 1992. The dominant role of low-frequency interaural time differences in sound localization. J Acoust Soc Am 91, 1648–1661. doi:10.1121/1.402445

Wilk, M., Hessler, R., Mugridge, K., Jolly, C., Fehr, M., Lenarz, T., Scheper, V., 2016. Impedance Changes and Fibrous Tissue Growth after Cochlear Implantation Are Correlated and Can Be Reduced Using a Dexamethasone Eluting Electrode. PLoS One 11, 1–19. doi:10.1371/journal.pone.0147552

Wilson, B.S., Dorman, M.F., 2008. Cochlear implants: A remarkable past and a brilliant future. Hear. Res. 242, 3–21. doi:10.1016/j.heares.2008.06.005

Wise, A.K., Pujol, R., Landry, T.G., Fallon, J.B., Shepherd, R.K., 2017. Structural and Ultrastructural Changes to Type I Spiral Ganglion Neurons and Schwann Cells in the Deafened Guinea Pig Cochlea. JARO - J. Assoc. Res. Otolaryngol. 769, 1–19. doi:10.1007/s10162-017-0631-y

Yamazaki, H., Easwar, V., Papsin, B., Gordon, K., Deighton, M., 2017. Simultaneous bilateral cochlear implants: Developmental advances do not yet achieve normal cortical processing. Brain Behav. 7, e00638. doi:10.1002/brb3.638

Zhou, N., 2017. Deactivating stimulation sites based on low-rate thresholds improves spectral ripple and speech reception thresholds in cochlear implant users. J. Acoust. Soc. Am. 141, EL243–EL248. doi:10.1121/1.4977235

Zilany, M.S.A., Bruce, I.C., Carney, L.H., 2014. Updated parameters and expanded simulation options for a model of the auditory periphery. J. Acoust. Soc. Am. 135, 283–286. doi:10.1121/1.4837815

Zimmermann, C.E., Burgess, B.J., Nadol, J.B., 1995. Patterns of degeneration in the human cochlear nerve. Hear. Res. 90, 192–201. doi:10.1016/0378-5955(95)00165-1

Zwislocki, J., Feldman, R.S., 1956. Just Noticeable Differences in Dichotic Phase. J. Acoust. Soc. Am. 28, 860–864. doi:10.1002/9780470479216.corpsy0481